Textures and fabrics in the GRIP ice core, in relation to climate history and ice deformation

Thorsteinn Thorsteinsson

Ber. Polarforsch. 205 (1996)
ISSN 0176 - 5027

Thorsteinn Thorsteinsson

Alfred Wegener Institut für Polar- und Meeresforschung
Sektion Geophysik
Postfach 12 01 61
D-27515 Bremerhaven

Die vorliegende Arbeit ist die inhaltlich unveränderte Fassung einer Dissertation, die 1996 dem Fachbereich Geowissenschaften der Universität Bremen vorgelegt wurde.

CONTENTS

	Page
Acknowledgments	3
Abstract	5
Zusammenfassung	7
1. INTRODUCTION	9
Ice core studies	9
The GRIP core	13
This work	15
2. BACKGROUND	17
2.1 Ice crystals	17
The structure of ice crystals	17
Defects in the crystal lattice	19
2.2 Deformation of ice	24
Stress and strain	24
Deformation of single ice crystals	28
Deformation of polycrystalline ice	30
The flow law for ice	31
2.3 Recrystallization processes in polar ice	33
Normal grain growth	34
Polygonization	37
Migration recrystallization	38
Impurity effects	40
2.4 Fabric development in ice	41
Formation of preferred fabrics	41
Rotation of c-axes	43
2.5 The ice sheet at Summit	47
Surface and bedrock topography	47
Ice flow regime and temperature	48
Timescale	50
3. MEASUREMENTS	52
3.1 Sample preparation	52
Sampling from the GRIP core	52
Thin section preparation	53
3.2 Crystal size measurements	54
3.3 C-axis measurements	57
Optical properties of ice	57

The Universal Stage 57
C-axis measurements 61
Fabric diagrams 64
Fabric statistics 66

4. RESULTS 69
4.1 The crystal size profile 69
4.2 Crystal orientation fabrics 71

5. DISCUSSION 80
5.1 Crystal size variations 80
The normal grain growth regime 80
The polygonization regime 82
The Wisconsin ice: Impurity effects 85
The Eemian ice: Crystal size as a climatic parameter 89
The lowest 160 m: Migration recrystallization? 97
The silty ice 99
5.2 Crystal fabric development 101
Overview 101
Formation of the single maximum 103
Fabrics in coarse grained ice 105
Simulation of the GRIP fabrics 106
5.3 Flow properties of Summit ice 108
The "soft" ice age ice problem 108
The Holocene-Wisconsin transition in the GRIP core 109
Rheological contrasts in the lowest 250 m 111
Variation in geometric softness 113
Deformation tests on GRIP core samples 114

6. STRATIGRAPHIC STUDIES 120
Visual stratigraphy 120
Origin of the disturbances 125
Effects on fabrics 128

7. SUMMARY AND OUTLOOK 134
Conclusions 134
Recommendations 135

8. REFERENCES 137

ACKNOWLEDGMENTS

This thesis results from work carried out at the Alfred Wegener Institute between September 1992 and February 1996. I am deeply grateful to Prof. Heinz Miller for giving me the opportunity to carry out this PhD work within the framework of the GRIP project, and for providing excellent guidance and support. I would also like to express my warmest thanks to Sepp Kipfstuhl, with whom I have collaborated closely throughout this period. Without his engagement at Summit, his great effort in collecting and preparing samples and his continuing and unselfish support of all kinds, this work would never have been carried out. I further thank Prof. U. Bleil for serving as co-referee.

I have enjoyed the excellent facilities of the Alfred Wegener Institute while working on this project. The atmosphere in the geophysics/glaciology group has been very friendly and stimulating and I would like to thank all those who have given me new insights and ideas, provided technical and computing assistance, helped me on administrative issues and provided good comradeship at AWI, in the field and during travel. In particular I would like to thank Hajo Eicken, Andreas Frenzel, Christel Hoffmann, Brunhilde Kunsch, László Oskó, Frank Pauer, Fernando Valero-Delgado and Frank Wilhelms, but many more could be mentioned. All participants in the North Greenland Traverse are thanked for excellent cooperation.

The GRIP project can be said to have been fathered by Willi Dansgaard, who developed the first plans for a deep drilling in Central Greenland almost 30 years ago. The great success of this cooperative effort is due to the hard work of many people who have participated at all levels. Since I removed the first blocks of snow from the spot selected for the deep hole, I have had the opportunity to take part in every aspect of this cooperation: General camp work at Summit, core drilling, core processing, administrative work, scientific analysis and conference presentation. It has been a great experience and I thank all the individuals I have worked with in one way or another on the ice sheet and at various research institutes.

Special thanks are due to colleagues at the Geophysical Institute at the University of Copenhagen, where I was originally brought into the field of ice core studies. In particular, I would like to thank Prof. Sigfus J. Johnsen, who aroused my interest in ice core work while he was my teacher at the University of Iceland. He has been my unofficial mentor ever since and I can never thank him fully for all the insights he has offered me during many, extended discussions. Personal friendship and support during the years from him and his wife, Pálína Kristinsdóttir, is very much appreciated. I would also like to thank Dorthe Dahl-Jensen for very stimulating cooperation on deformation tests during this period, from which I have benefitted greatly. I further offer my thanks to Jørgen P. Steffensen, Niels Gundestrup, Claus Hammer and Henrik Clausen for giving me access to unpublished data, and for various other support over the years.

Excellent relations with the ice core group at the University of Bern have resulted in fruitful cooperation. In particular, I would like to thank Katrin Fuhrer for providing the calcium data, which have been crucial for my work, and Bernhard Stauffer, chairman of the GRIP Steering Committee, for encouraging and supporting me and other young scientists in the GRIP community in various ways.

I thank Olivier Castelnau and Paul Duval at the Laboratoire de Glaciologie in Grenoble for stimulating cooperation on a joint fabric–simulation project. Their expertise provided me with many new insights. I would also like to thank Michel Legrand for supplying unpublished chemistry data.

I am very grateful to Prof. Roland Souchez at the Université Libre de Bruxelles for inviting me to visit his laboratory and join his group in a study of textures and fabrics in the basal ice from the GRIP core. I extend my warmest thanks to Jean-Louis Tison and Reginald Lorrain for excellent cooperation during this project.

I thank colleagues at the British Antarctic Survey in Cambridge, Eric Wolff, David Peel and John Moore (now at the Arctic Centre in Rovaniemi) for very friendly exchange of data, ideas and information, as well as Valter Maggi at the University of Milano for sending me information on his particle studies.

The simultaneous drilling of two deep ice cores in the Summit area – the European GRIP core and the American GISP2 core – has naturally led to some important links across the Atlantic. Stimulating contact and cooperation with various researchers in the US, including Chris Shuman, Ed Waddington, Pierre Biscaye, Tony Gow and Deb Meese is acknowledged. I would also like to offer my sincere thanks to Richard Alley at Penn State University for inviting me for a short visit to his laboratory and for providing me with various kinds of information and support while I have been working on this thesis.

For preparing me to enter the field of science I thank former teachers at the University of Iceland. I also thank C.C. Langway and H. Shoji, formerly at the State University of New York at Buffalo, and David Fisher, formerly at the University of Copenhagen for introducing me to the study of ice textures and fabrics while I was a student at the University of Copenhagen.

I am grateful to John Firestone for reading much of my manuscript and significantly improving my English.

Last but not least I would like to thank my parents, Thorsteinn Gudjónsson and Steingerdur Thorsteinsdóttir, and other relatives for continuing support over the years, which has been of vital importance.

I dedicate this thesis to the memory of my brother, Eiríkur H. Thorsteinsson.

ABSTRACT

Within the framework of the joint European Greenland Icecore Project (GRIP) a 3029 m long ice core was drilled in Central Greenland in the years 1989–1992. Studies of isotopes and various atmospheric constituents in the core have revealed a detailed record of climatic variations reaching more than 100 000 years back in time. The results indicate that Holocene climate has been remarkably stable and have confirmed the occurrence of rapid climatic variation during the last ice age (the Wisconsin). Climatic instability observed in the core part believed to date from the Eemian interglacial has not been confirmed by other climate records.

The GRIP core offers a unique possibility to study the growth, rotation and recrystallization of polar ice at an ideal location, covering a time span of more than 100.000 years. This information is obtained by a comprehensive thin section study of crystal sizes and c-axis orientations along its entire length. The results confirm earlier, basic observations on deep ice cores and have led to new insights. A significant variation of crystal size with climatic parameters is shown to persist to a great depth in the core; the development of a strong crystalline anisotropy in the ice sheet is also demonstrated. Considerable insight is obtained into the rheological properties of the ice sheet from these studies.

In the upper 700 m of the core, the average area of ice crystals is found to increase linearly with time, in accordance with a well known grain-growth law. This is the regime of normal grain growth. Below 700 m, grain size does not increase any further and keeps a nearly constant average diameter of 4 mm. The stop in grain growth is probably due to the fragmentation of crystals under increasing strain (polygonization). The polygonization regime covers the lower part of the Holocene and the entire Wisconsin ice (1625-2790 m), with smaller crystals in the latter (typically 2-3 mm). The difference is probably due to a heightened impurity content in the ice age ice. The impurities tend to segregate to grain boundaries and slow their migration, and thereby the grain-growth rate.

In the Eemian ice (2790-2865 m), a continuous record of crystal size has revealed a surprisingly strong correlation of this parameter with various climatic parameters measured on the core, such as isotopes, impurity content and electric conductivity. Large crystals (1-2 cm) are found in ice from warm periods, small crystals (3-4 mm) in ice from cold stages. Although several studies have now suggested that the Eemian sequence might not be in stratigraphic order, it is likely that the result described here will prove to be a valid one: that outlines of past climatic variation can be inferred from a study of crystal size changes.

Closer to the bottom, the growth of very large crystals is observed. This is likely due to extensive recrystallization at relatively high temperatures near the bottom (-10 °C), combined with the effects of great age. The crystal size-isotope-impurity covariation disappears in the lowest 100 m of the core.

The results from the crystal fabric measurements are compatible with the ice flow regime expected at Summit, which is positioned at the top of a dome on the Central Greenland ice divide. The c-axis orientation gradually and progressively changes from a random pattern near the surface to a strong vertical single maximum fabric at 2200 m depth. A rapid strengthening of the fabric is not observed at the Holocene-Wisconsin transition. Enhanced flow of Wisconsin ice is thus not expected at Summit. The formation mechanism of the preferred fabric is believed to be through c-axis rotation by intracrystalline dislocation glide, under the influence of vertical compressive stress. In the coarse grained ice within and below the Eemian, the fabric weakens, due to either recrystallization mechanisms or different stress conditions in the lowest part of the ice sheet or both.

There are clear indications that the vertical single maximum fabric hardens the ice against vertical compression. This hardening is evident in deformation tests carried out on samples from the core. Softening of the ice against horizontal shear is also expected, especially in fine-grained layers. The c-axis measurements reveal fabric contrasts between fine-grained and coarse-grained layers, which are likely to result in rheological differences.

The climatic interpretations from the core assume that the layer sequence in the core is continuous and undisturbed by irregular flow patterns. Studies of the visual stratigraphy in the ice core have revealed that significant flow distortion has occurred between 2850 m and 2950 m depth, an interval which includes the lowest 1/4 of the Eemian sequence. Distortions have not been found in the upper 3/4 of the Eemian ice. Highly inclined layering occurs in a 1 m increment 30 m above the Eemian, indicating that the timescale below 2750 m depth, beyond 100 kyr, cannot be considered certain. Thin section study of the inclined layering and of other flow distortions reveals that these features exert a marked influence on the ice fabric, by rotating c-axes out of the vertical position. The presence of overturned folds below 2850 m depth suggests that simple shear is, or has recently been active in the lowest part of the ice sheet.

ZUSAMMENFASSUNG

Im Rahmen des Greenland Ice Core Projects (GRIP) wurde zwischen 1989 und 1992 ein 3028 m langer Eiskern durch den grönländischen Eisschild gebohrt. Isotopen- und Spurenstoffanalysen ergeben ein detailliertes Bild der Klimaänderungen über den Verlauf der letzten 100 000 Jahre: Das Klima im Holozän zeigt sich stabil. Im Gegensatz dazu ist das Klima der letzten Eiszeit (Wisconsin) und des letzten Interglazials (Eem) durch schnelle Schwankungen und Instabilitäten gekennzeichnet. Die Klimainstabilitäten im Eem-Interglazial sind jedoch durch andere Untersuchungen bislang nicht eindeutig belegt.

Die besondere Lage des Bohrpunktes auf einem Eisdom bietet die einzigartige Möglichkeit, Wachstum, Rotation und Rekristallisation von polarem Eis über einen Zeitraum von mehr als 100000 Jahren bei vorwiegend vertikaler Bewegung zu untersuchen. Der Schwerpunkt der vorliegenden Arbeit liegt in der Analyse des Kornwachstums und der beobachteten c-Achsenverteilung. Analysen mehrerer Hundert Dünnschnitte bestätigen frühere Beobachtungen und führen zu neuen Erkenntnissen. Die Korngröße variiert mit den Klimaparametern bis in große Tiefen. Die bevorzugt vertikal orientierten c-Achsen führen zu einer ausgeprägten Anisotropie im Eisschild. Hieraus lassen sich Rückschlüsse auf das Fließregime ableiten.

In den obersten 700 m des Kernes nimmt die mittlere Korngröße in Übereinstimmung mit dem bekannten Gesetz über das Kornwachstum linear mit dem Alter zu. Unterhalb von 700 m Tiefe stoppt das Kornwachstum. Der mittlere Korndurchmesser bleibt mit 4 mm nahezu konstant. Ursache dafür dürfte Subkornbildung (Polygonization) infolge zunehmender Deformation sein. Polygonization bestimmt bzw. verhindert im unteren Teil des Holozäns sowie im gesamten Wisconsin (1625-2790 m) das Kornwachstum. Die Ursache dafür, daß die Kristalle im Wisconsin-Eis kleiner (2-3 mm) sind, dürfte in den stark erhöhten Spurenstoffkonzentrationen liegen. Die Spurenstoffe sammeln sich bevorzugt an den Korngrenzflächen. Sie behindern das Wandern der Korngrenzen und damit das Kornwachstum.

Über den Bereich des Eems (2790-2865 m Tiefe) wurde eine kontinuierliche Dünnschnittsequenz erstellt. Die Kristallgröße ist sehr gut korreliert mit Klimaparametern wie den stabilen Isotopen, der Spurenstoffkonzentration und der elektrischen Leitfähigkeit. Große Kristalle (10-20 mm) sind charakteristisch für warme Perioden, kleine Kristalle (3-4 mm) für kalte Perioden. Obwohl Ergebnissen anderer Untersuchungen zufolge die Eem-Sequenz möglicherweise als gestört angesehen werden muß, bleiben wahrscheinlich die hier vorgestellten Ergebnisse gültig, wonach sich aus Änderungen der Kristallgröße Klimaschwankungen ableiten lassen.

Nahe dem Felsuntergrund werden sehr große Kristalle beobachtet. Dafür dürften als Folge der relativ hohen Temperatur (-10°C) Rekristallisation und das hohe Alter verantwortlich sein. Die Abhängigkeit zwischen Kristallgröße und den Konzentrationen an stabilen Isotopen und Spurenstoffen ist in den untersten 100 m des Kerns nicht mehr vorhanden.

Die c-Achsenverteilung deutet, wie von der Position des Bohrpunktes auf einem Eisdom aus erwartet, ein bemerkenswert stabiles Fließregime an. Die c-Achsen regeln sich mit zunehmender Tiefe auf ein einzelnes Maximum mit vertikaler Orientierung ein. Die Einregelung verläuft stetig, auch am Übergang zur letzten Eiszeit. Eine verstärkte Zunahme des Einregelungsgrades wird dort nicht beobachtet. Deshalb ist bevorzugtes Fließen von Wisconsin-Eis am Summit nicht zu erwarten. Für die Ausrichtung der c-Achsen dürfte die Rotation der Kristalle infolge intrakristallinen Versetzungsgleitens unter dem Einfluß vertikaler Kompression verantwortlich sein. Im grobkörnigem Eis in und unterhalb des Eems nimmt infolge von Rekristallisationsprozessen und/oder unterschiedlicher Deformationsbedingungen der Grad der Einregelung wieder ab.

Aufgrund der vertikal ausgerichteten c-Achsen ist das Eis hart gegenüber vertikaler Kompression. Dieses Verhalten wird durch Deformationstests bestätigt. Umgekehrt kann man erwarten, daß sich Lagen mit kleinen Korngrößen relativ weich gegenüber horizontaler Scherung verhalten. Die c-Achsenverteilungen zeigen Kontraste zwischen klein- und grobkörnigen Schichten, die sehr wahrscheinlich auch für die Unterschiede in den rheologischen Eigenschaften verantwortlich sind.

Die Rekonstruktion des Klimas aus Eiskernanalysen beruht auf der Annahme, daß die Schichtenabfolge kontinuierlich und nicht durch die Bewegung des Eises gestört ist. Untersuchungen der visuellen Stratigraphie ergeben Hinweise auf Störungen zwischen 2850 und 2950 m Tiefe. Dieses Intervall schließt nur das untere Viertel der Eem-Sequenz mit ein, dennoch sollte der gesamte Eem-Klimarekord mit großer Vorsicht interpretiert werden. In Dünnschnittanalysen sind diese gestörten Bereiche durch ihre von der Vertikalen deutlich abweichende c-Achsenorientierung zu erkennen. Überkippte Falten unterhalb von 2850 m Tiefe deuten an, daß dort "simple shear" aktiv ist oder in der jüngsten Vergangenheit aktiv war.

1. INTRODUCTION

This thesis presents the results of a comprehensive study of variations in textures (crystal sizes and shapes) and fabrics (crystal orientations) in the GRIP deep ice core, drilled in Central Greenland in the years 1989–1992. The results are interpreted within the framework of current knowledge of recrystallization processes in polar ice, the rheological properties of the ice are evaluated, and stratigraphic disturbances in the lowest part of the ice sheet and their relevance for the climatic record are discussed. This chapter briefly outlines ice core drilling and research, describes some major results from the GRIP core and finally outlines the contents of the thesis.

Ice core studies

Ice core drilling on the Greenland Ice Sheet was initiated in 1956–7 with the retrieval of a 400 m long ice core from Site 2, NW-Greenland (Langway, 1967). In the years 1963–1966 the first deep drilling to bedrock was undertaken at Camp Century (Ueda & Garfield, 1968) and a core was retrieved with ice dating back to at least 100.000 years BP, according to isotopic analysis (Johnsen et al., 1972). Various studies were undertaken between 1971 and 1981 within the framework of the American–Danish–Swiss Greenland Ice Sheet Program (GISP), culminating in a deep drilling at the Dye 3 station in South Greenland (Langway et al., 1985). Measurements on this core allowed continuous annual-layer dating of the ice from the entire Holocene period (Hammer et al., 1986) and further indicated that rapid climatic variation had occurred during the last ice age, the Wisconsin period (Dansgaard et al., 1982).

From a scientific viewpoint, the Central Greenland region has long been assumed to be more suitable for the retrieval of ice core records than other parts of the Greenland ice sheet. Here, two deep drilling projects were initiated in 1989: The European Greenland Ice Core Project (GRIP), which cored at the Summit of the ice sheet (72° 34.5´ N, 37° 38.5´ W; 3230 m.a.s.l.), and the American Greenland Ice Sheet Project Two (GISP2), which operated 27 km west of the GRIP site. Both drillings successfully reached bedrock below 3 km depth. Analysis of the ice cores has provided new impetus to the study of palaeoclimates and atmospheric processes and brought important new insights into the stratigraphy, rheology and crystal structure of polar ice sheets.

In Antarctica, deep ice cores have been drilled at Byrd Station and at Vostok. Coring to intermediate depths has been performed at Dome C and near Mizuho station. Currently, the Vostok borehole is being extended to near bedrock, and a deep drilling has been initiated at Dome F. Within the framework of the European Project for Ice Coring in Antarctica (EPICA), two deep ice cores will be drilled to bedrock within the next decade, at Dome C and in Dronning Maud Land.

Drilling sites where ice cores have been taken from depths greater than 500 m are listed in Table 1.1; their locations are shown in Fig. 1.1.

Polar ice cores have been shown to be very rich sources of information on past environmental conditions. Each year, a layer of snow falls on the surface of the ice sheet, becomes buried by subsequent snowfalls and then compacted into ice within a depth of less than 100 meters. Various atmospheric constituents are preserved in the snow and the ice; seasonal variations in several of them allow the counting of annual layers in the entire Holocene ice and in parts of the Wisconsin ice. Vertical compression of the ice leads to thinning of the annual layers with depth; models of this process are used to date the ice beyond the level where annual layer counting is no longer feasible. The most important studies carried out on ice cores are briefly outlined below.

Isotope studies. The oxygen isotope ratio $^{18}O/^{16}O$ in falling snow depends on the temperature in the precipitating cloud (Dansgaard et al., 1973). Isotope measurements thus reveal summer-winter variations in temperature which under favourable conditions can be used for annual layer counting (Hammer et al., 1978). Short- and long-term climatic variations are also clearly detected as shifts in the isotopic profiles. Oxygen-isotope data from Greenland ice cores have provided the most detailed information available on climatic variation in the Northern Hemisphere during the last 100.000 years (e.g. Johnsen et al., 1992; Dansgaard et al., 1993).

Electric conductivity studies. The past concentration of various acids in the atmosphere, most importantly H_2SO_4, HCl and HF, is reflected by the electric conductivity measured on the ice cores (Hammer, 1980). Greatly elevated acidity following violent volcanic eruptions is clearly detected in the cores; the identification of historically recorded eruptions is important for dating purposes (Hammer et al., 1980). In addition, electrical measurements can be used to estimate the concentrations of sea-salts and other atmospherically derived impurities in the ice (Wolff et al., 1995).

Chemistry studies. Much more detailed information on the content of soluble chemical impurities is obtained by direct ion chromatography measurements (de Angelis et al., 1995) or by the use of continuous flow analysis systems (Fuhrer et al., 1993). Variation in the concentrations of major ions reflect

TABLE 1.1 DEEP DRILLING SITES

Site	Region	Core length (m)	Completed
Camp Century	NW. Greenland	1390 m	1966
Dye 3	S. Greenland	2037 m	1981
GRIP	Central Greenland	3029 m	1992
GISP2	Central Greenland	3053 m	1993
Byrd Station	W. Antarctica	2164 m	1968
Dome C	E. Antarctica	905 m	1978
Mizuho Station	E. Antarctica	700 m	1984
Law Dome	E. Antarctica	1203 m	1993
Vostok	E. Antarctica	>3000 m	1995

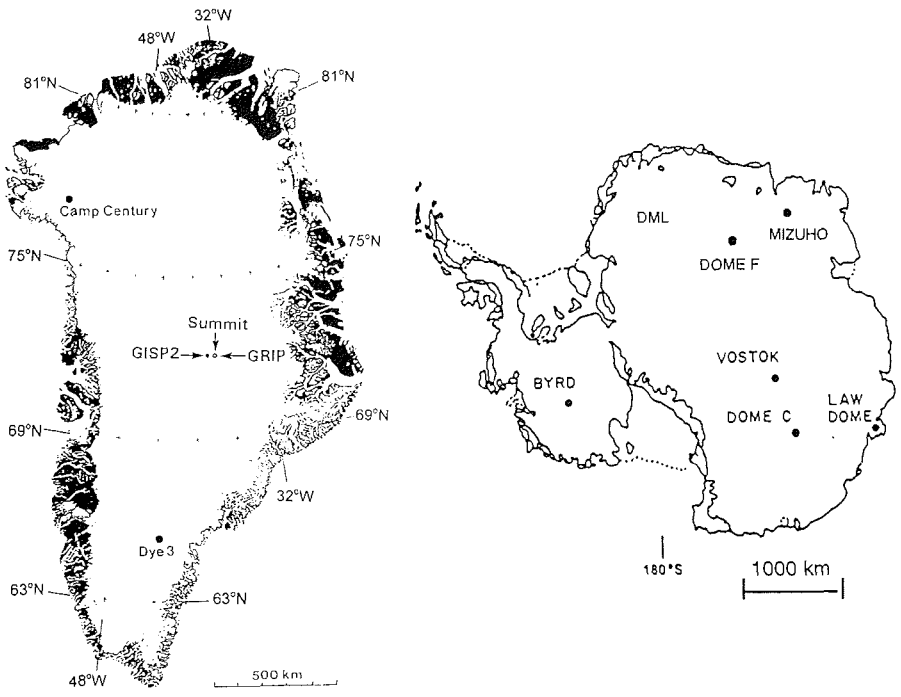

Fig. 1.1 - Deep drilling sites in Greenland and Antarctica.

changes in the productivity of their marine and terrestrial sources. For example, suddenly elevated concentrations of ammonium (NH_4^+) in the Holocene ice are believed to result from extensive forest fires (biomass burning), mainly on the North American continent. Another example is the increased concentration of calcium (Ca^{++}) during the ice age, which probably reflects the exposure of great continental shelf areas to the atmosphere, when sea level was much lower than today.

Gas analyses. Reconstruction of past atmospheric concentrations of greenhouse gases, like carbon dioxide (CO_2) and methane (CH_4), has been one of the main goals of ice core studies (Oeschger et al., 1982; Raynaud et al., 1993). Clear evidence has been obtained showing that the level of CO_2 in the atmosphere has increased by 30% since the start of the industrial revolution, and that CO_2 levels were considerably lower during the ice age than during the Holocene. It has also been found that the atmospheric methane concentration varied in parallel with temperature variations inferred for the last glacial period (Chappellaz et al., 1993).

Stratigraphy. Summer-winter variations in snow structure and impurity content allow the identification of visible strata in the ice cores (Alley et al., in press). These can be used for annual layer counting back to ≈ 50.000 years BP. In addition, the study of visible cloudy bands in the GRIP and GISP2 ice cores has yielded important information on the occurrence of disturbed layering in the lowest part of the ice sheet (Kipfstuhl & Thorsteinsson, 1993; Alley et al., 1995).

Textures and fabrics. The study of variations in crystal sizes and c-axis orientations reveals important information on recrystallization processes in polar ice. The first major study of variations in textures and fabrics within a large polar ice sheet was carried out on the Byrd ice core from West Antarctica (Gow & Williamson, 1976). Similar work has been performed on the Greenland cores from Camp Century and Dye 3 (Herron & Langway, 1982; Herron et al., 1985), on the Vostok core from East Antarctica (Lipenkov et al., 1989), on shallow cores from the Barnes ice cap in the Canadian Arctic (Hooke & Hudleston, 1980) and on cores drilled on the Law Dome ice cap, Antarctica (e.g. Russell-Head & Budd, 1979; Li Jun, 1995). The studies have shown that crystal size variation in the different deep cores follows a common pattern and that strong anisotropies develop within the ice sheets. In addition, fabric contrasts and grain-size differences across climatic transitions are believed to cause important variations in the rheological properties of the ice at certain drill sites (Paterson, 1991), and thus provide an interesting comparison with deformation rates observed in the drill-holes after ice core recovery (Dahl-Jensen and Gundestrup, 1987). It is also likely that models of the flow and evolution of polar ice sheets can benefit from incorporation of the anisotropy demonstrated by the fabric measurements.

The GRIP core

The GRIP project was carried out as a joint European effort involving 8 nations, partly organized by the European Science Foundation (ESF). The main laboratories and their research fields are listed in Table 1.2. Activities at Summit were initiated in 1989, but drilling was carried out in the summers of 1990-92. Drilling was succesfully terminated on July 12 1992 at a depth of 3028.65 m, when the drill had penetrated through 6 meters of debris laden bottom ice.

Drilling was carried out with the ISTUK deep drill, developed mainly at the University of Copenhagen (Johnsen et al., 1994). Sample cutting and various scientific analyses were performed on the cores at the drill site, in a trench dug into the snow surface (Gundestrup et al., 1994). Up to 50 people were present at a time in the GRIP camp, occupied with drilling, core processing and general camp work.

The results from the core concerning palaeoclimatic variations, reported by Johnsen et al. (1992), Dansgaard et al. (1993) and GRIP Members (1993), have received considerable attention. A $\delta^{18}O$ profile spanning the entire core is displayed in Fig. 1.2. The major features are as follows:

1. The warm Holocene period (0-11.5 kyr BP; 0-1625 m) is characterized by very stable climate, in contrast to the instability of the preceding 100-200 kyr.
2. Several interstadial periods (numbered 1-24) of relatively mild climate conditions have occurred during the Wisconsin glacial period (11.5-110 kyr BP; 1625-2790 m).
3. Climatic instability is also observed in the part of the core identified as the Eemian interglacial (110-135 kyr, 2790-2865 m), in contrast to previous records, which indicate an unbroken warm period.

The American GISP2 core reached bedrock in July 1993 and intercomparison of the isotopic and electric conductivity records from the two cores soon revealed an excellent match back to ≈100 kyr BP (Grootes et al., 1993; Taylor et al., 1993). The unstable Eemian climate was, however, not confirmed by the GISP2 record, and it became apparent that the original stratigraphy had been disturbed in the lowest parts of both cores. To which extent the disturbances have affected the GRIP Eemian has not been fully resolved, but several sources of evidence indicate that this part of the core might not be in stratigraphic order (e.g. Fuchs & Leuenberger, in press) - although definite conclusions have not been reached.

TABLE 1.2 - GRIP CORE STUDIES

COUNTRY	INSTITUTE	MAIN FIELDS OF STUDY
BELGIUM	Université Libre de Bruxelles	Bottom silty ice - formation and flow properties
DENMARK	University of Copenhagen	Climate history, past volcanism, ice flow modelling, borehole logging, rheology of ice.
FRANCE	Laboratoire de Glaciologie, Grenoble Laboratoire de Modelisation du Climat, Paris	Greenhouse gases, ionic chemistry, rheology of ice Isotope studies, climate modelling
GERMANY	Alfred Wegener Institute Bremerhaven	Physical properties: Density, conductivity, textures and fabrics visual stratigraphy
GREAT BRITAIN	British Antarctic Survey Cambridge	Dielectric properties of ice, SEM studies on particles
ICELAND	University of Iceland, Nordic Volcanologic Institute, Reykjavík	Isotope studies Volcanic ash layers
ITALY	University of Milano	Volcanic and other airborne particles
SWITZERLAND	University of Bern	Greenhouse gases, continuous chemistry, total gas content

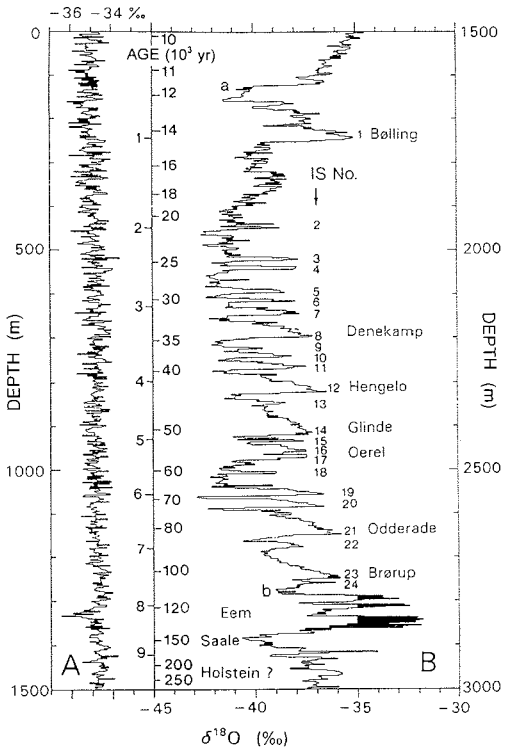

Fig. 1.2 - The GRIP $\delta^{18}O$ profile, plotted on a linear depth scale. A) 0 - 1500 m, B) 1500 - 3000 m. The timescales for the two sections are shown in between them. - From Dansgaard et al. (1993).

This work

The study of textures and fabrics has been one of the main contributions of the Alfred Wegener Institute to the GRIP project. These parameters are mainly influenced by changing temperatures, stresses and strains within the ice sheet. The GRIP core offers a unique possibility to study the growth, rotation and recrystallization of polar ice at an ideal location, covering a time span of more than 100.000 years.

Terminology. Following normal practice in ice core analysis (Gow & Williamson, 1976), the term texture will refer to the sizes and shapes of the ice crystals, and fabrics to the c-axis orientation distributions of the crystals. The words crystal and grain will be used synonymously. In natural ice, single crystals are assembled into a mass of polycrystalline ice, and each crystal is separated from its nearest neighbours by grain boundaries. Crystal size

changes take place by grain boundary migration, which leads to grain growth if the average grain size in a sample is increasing.
Regarding different periods covered by the timescale, the North American term Wisconsin* will be used for the last ice age, since this is common practice in ice core studies. Corresponding European terms are Weichsel and Würm. On the other hand, the European terms Eem and Saale are used for the last interglacial and for the penultimate glacial periods, respectively. These terms will be used for the core intervals in which the periods were originally identified (Dansgaard et al., 1993; GRIP Members, 1993), but this should not be taken as an assumption that the climatic records from these periods are undisturbed.

In Chapter 2, background information on the structure and deformation of ice is given, along with an overview of recrystallization processes and fabric development in polar ice. The general condition of the ice sheet at Summit is also outlined.
Chapter 3 gives an overview of the methods used to measure crystal sizes and c-axis orientations, along with a discussion of sources of error. Furthermore, statistical parameters used to evaluate fabric strength are derived and discussed.
In Chapter 4, the main results from measurements of crystal sizes and fabrics on the whole GRIP core are presented and described. From this chapter, the reader gets the necessary overview over the evolution of those parameters in the ice sheet, prior to a discussion of the results in subsequent chapters. More detailed results also are presented in chapters 5 and 6.
Chapter 5 starts with a discussion of two major recrystallization processes observed in the Holocene ice: normal grain growth and polygonization. Crystal size variations in the Wisconsin ice are then presented and interpreted as resulting from a probable influence of impurities on grain boundary migration. Detailed data from the Eemian ice, showing that crystal size in this sequence varies closely in parallel with climatic parameters, are presented and thoroughly discussed, as is the growth of very large crystals in the lowest 250 m of the ice sheet. Following this, the fabric evolution in the core and the mechanisms causing it are discussed further. The results are then used to draw conclusions regarding the flow properties of the ice sheet at Summit. In addition, results of crystal size and orientation measurements on GRIP core samples, which have been used in deformation tests carried out at the University of Copenhagen, are presented and discussed.
Chapter 6 contains a description of main results from studies of stratigraphic disturbances in the lowest part of the core. The implications of these observations for the climatic record in the core, especially for the Eemian sequence, are discussed. Special attention is given to the effects of the flow disturbances on ice fabrics.
Finally, Chapter 7 concludes the thesis with a summary and outlook.

* Wisconsinan is more correct, but will not be used here.

2. BACKGROUND

2.1 ICE CRYSTALS

The structure of ice crystals

In natural ice (ice Ih), water molecules (H_2O) are joined together by a hydrogen bond; that is, by electrostatic attractions between the oxygen and hydrogen atoms. From results of x-ray diffraction experiments, Bragg (1922) concluded that each oxygen atom in the ice crystal lattice is surrounded by four neighbouring oxygen atoms in a tetrahedral arrangement. This leads to a hexagonal crystal structure, where the oxygen atoms are arranged in layers separated by a distance of 0.276 nm, as indicated in Fig. 2.1. These layers, the so-called basal planes of the crystals, are actually made up of two planes 0.0923 nm apart. The normal to the basal planes is called the c-axis of the

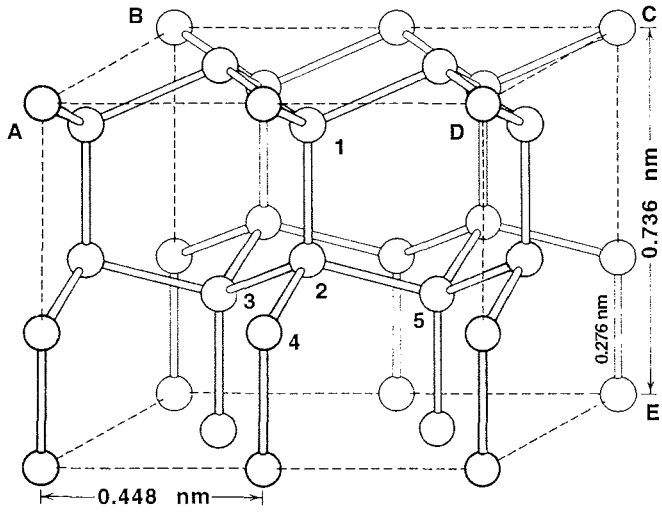

Fig. 2.1 - The crystal structure of ice Ih. The white spheres denote the oxygen atoms. The atoms labeled 1,2,3,4,5 indicate the typical tetrahedral arrangement. Three basal planes are shown (ABCD being the uppermost), the shortest distance between which is 0.276 nm. Each basal plane consists of two layers separated by a distance of 0.0923 nm. Thus the distance between atoms C and E is 0.276+0.0923+0.276+0.0923 ≈ 0.736 nm. This distance is the cell parameter c, the minimum vertical separation in which the pattern repeats exactly.

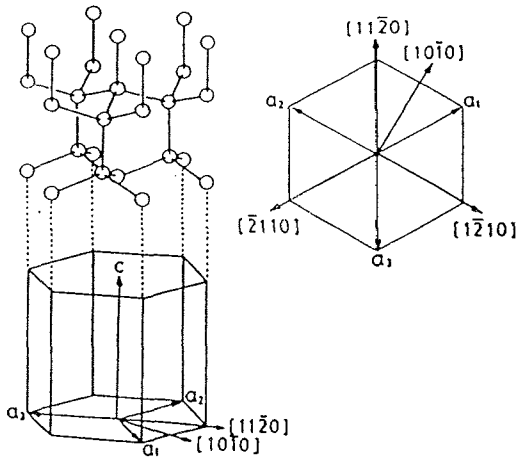

Fig. 2.2 - Left: A part of the ice crystal lattice and below it the corresponding hexagonal cell, showing the directions of the c-axis and the three a-axes.

Right: The cell viewed from above, along the c-axis, showing the three a-axes in the basal plane. Crystallographic direction indices (Miller-Bravais indices) in the negative direction of each a-axis, are indicated. The four indices denote, for translation in a particular direction, the components of this translation along each of the four crystallographic axes [a_1,a_2,a_3,c], respectively. The indices are always expressed in the smallest integers possible. For example, the [11$\bar{2}$0] direction simultaneously translates 1 unit length along the a_1 and a_2 axes, 2 unit lengths along the negative a_3 axis (hence the bar above 2) and 0 units along the caxis.

Miller-Bravais indices are also assigned to the crystallographic planes. The basal plane is denoted (0001), since the unit normal vector to this plane translates a unit distance in the direction of the c-axis and zero distance along each of the a-axes. The six vertical planes of the hexagonal cell are examples of prismatic planes, denoted (1$\bar{1}$00), ($\bar{1}$100), etc. Pyramidal planes in the crystal structure make an angle with the c-axis; examples of these are (10$\bar{1}$1), ($\bar{1}$011), etc.

For a more detailed description of the crystallographic indices see f.ex. Cox et al. (1974) and for the special case of ice see Hobbs (1974), p. 725.

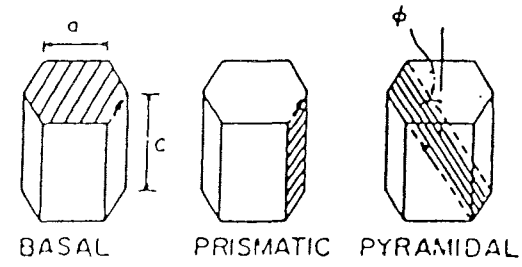

Fig. 2.3 - Crystallographic planes (shaded) in the ice lattice.

crystal. The c-axis is one of four crystallographic axes of the hexagonal crystal system, the other three (a_1, a_2 and a_3) are set mutually at 120° in the basal plane, as shown in Fig. 2.2. The basal plane is the plane of the closest packing in the structure of ice Ih. Other closely packed planes in the crystal structure are prismatic planes, which lie parallel to the c-axis. Planes that form an angle with the c-axis are called pyramidal planes (Fig. 2.3).
The fact that ice has a lower density (0.92 g/cm^3) than liquid water is generally believed to be due to the relatively "open" structure of the ice lattice, with considerable empty space between the molecules.

The infrared spectra of natural ice are similar to those of liquid water and water vapour, suggesting that the water molecule is preserved as a structural unit in the ice lattice. This lead Bernal and Fowler (1933) to suggest the following two principles for the positions of the hydrogen atoms (more accurately: for their protons):

1. Each oxygen atom in the lattice has two protons in its close vicinity, forming a H_2O molecule.
2. One proton is situated on each line joining a pair of oxygen atoms.

Fig. 2.4.a shows the structure of ice according to those rules.

Bernal and Fowler (1933) showed that the protons could assume six different configurations on the four O-O lines linking each oxygen atom to its nearest neighbours. Building on their work, Pauling (1935) proposed a statistical model for the structure of ice Ih, the essentials of which have been confirmed by later experimental work. According to this model, each proton can assume one of two positions on a O-O line, each position being located 0.095 nm from one of the oxygen atoms. Pauling showed that this leads to a total number of approximately $(3/2)^n$ possible proton configurations for a crystal lattice with n molecules.

Other forms of ice, with a crystalline structure different than ice Ih, have been produced in the laboratory. High pressures and varying temperatures are required to form these ices. At present, 12 crystallographic forms of ice are known (Ih, Ic (cubic), II, III, ..., XI) and two amorphous (non-crystalline) forms (Petrenko, 1993). Since pressures in excess of 2 kbar are required for most of these ices to form (compare with 0.3 kbar at the bottom of the Central Greenland ice sheet), they do not occur in natural form on Earth and thus are not of concern in this work.

Defects in the crystal lattice

The foregoing description referred to the properties of perfect crystals of ice. In real ice crystals, however, many imperfections occur, the most important of

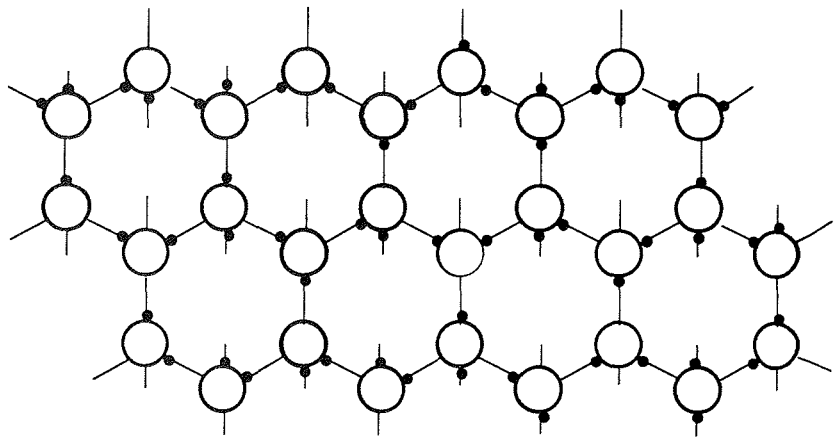

Fig. 2.4.a - Ideal structure of the ice crystal lattice, viewed along the c-axis. Large, open spheres denote oxygen atoms, small filled spheres hydrogen atoms. Since the angle between each two O-O lines in the tetrahedral structure is about 109° and the H-O-H angle in a free water molecule is about 105°, the molecules in the ice lattice deviate only slightly from the shape of water molecules in the vapour phase.

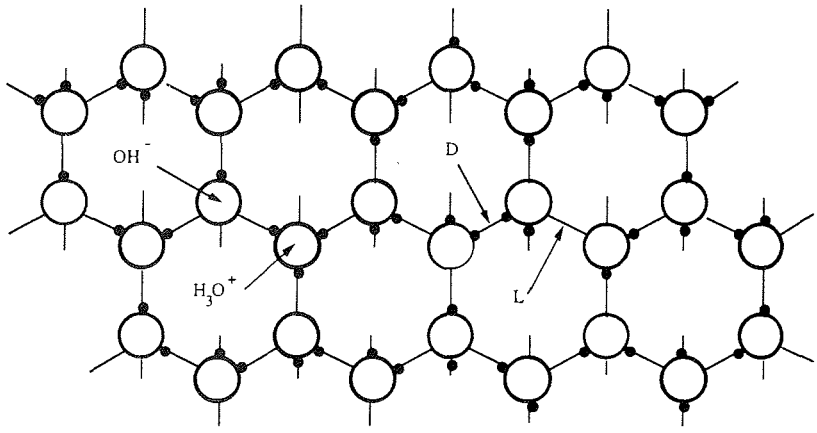

Fig. 2.4.b - The lattice in Fig. 2.4.a after the formation of: i) a pair of ionic defects (H_3O^+ and OH^-) by proton jump along a O-O line, and ii) a pair of Bjerrum defects by a proton jump from one O-O line to another. These are called D-defects and L-defects (D=doppelt (double); L=leer (empty)).

which will now be described briefly. A distinction is made between two types: point defects and linear defects:

1. Point defects. Deviations from the Bernal-Fowler rules can lead to the formation of the ionic and protonic point defects depicted in Fig. 2.4.b. A pair of H_3O^+ and OH^- ions can form by a proton jump along a O-O line, and the so-called Bjerrum defects (D- and L-defects) are produced when protons jump from one O-O line to another. Results of theoretical and experimental studies (e.g. Bjerrum, 1951; Jaccard, 1964) indicate that electric conduction in ice can be explained by the migration of these defects within the crystal lattice.

Other point defects in ice include the so-called molecular defects: vacancies and interstitials. A vacancy is a site within the lattice from which a water molecule is missing; an interstitial is an extra molecule situated in a space between the normal molecules of the structure. These defects are responsible for the self-diffusion of H_2O molecules in the lattice; a process which plays an important role during grain growth in polycrystalline ice. Recent experimental work suggests that self-diffusion can mainly be ascribed to the migration of interstitials (Hondoh et al.,1987; Petrenko, 1994).

Impurity molecules can also constitute point defects in the ice lattice. Examples are molecules of the HF and HCl acids, which are incorporated in such a way that the F and Cl atoms replace oxygen atoms in the lattice. In the case of KOH molecules, on the other hand, the K atom occupies an interstitial position, surrounded by oxygen atoms. The presence of these impurity molecules introduces ionic and protonic defects into the crystal structure and thus influences the electrical properties significantly.

2. Linear defects. Two types of the so-called dislocations constitute the most important linear defects in ice crystals:

1. Edge dislocations - which are additional planes of atoms inserted into a part of the regular crystal lattice.
2. Screw dislocations - which are offsets in the crystal structure, whereby a part of the crystal is translated one interatomic distance relative to another part.

Both types are illustrated in Fig. 2.5. For each dislocation the so-called Burgers vector, **b**, can be defined as giving the displacement of the lattice parts affected by the dislocation.

All natural crystals contain dislocations, but their concentration is highly dependent upon factors like strain, temperature and the presence of point defects. The dislocation density - ρ, is defined as the total length of dislocation line per unit volume of crystal and expressed in units of m^{-2}. For ice crystals grown under low-stress conditions, typical values of ρ are of the order of

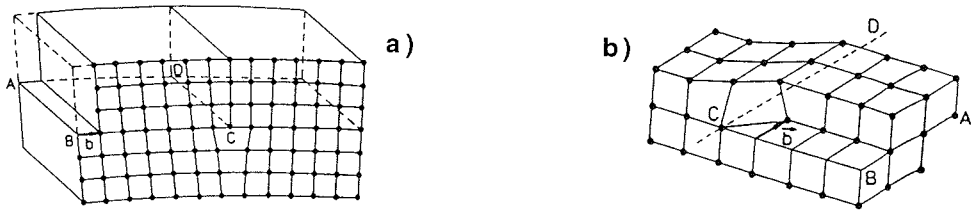

Fig. 2.5 - a) Edge dislocation, formed by the insertion of the extra atomic plane above the dislocation line CD. The Burgers vector, **b**, is perpendicular to this line.
b) Screw dislocation, formed when a part of a crystal lattice is translated one interatomic distance over another part. In this case the Burgers vector is parallel to the dislocation line (CD). For clarity, dislocations in simple cubic crystal structures are depicted.

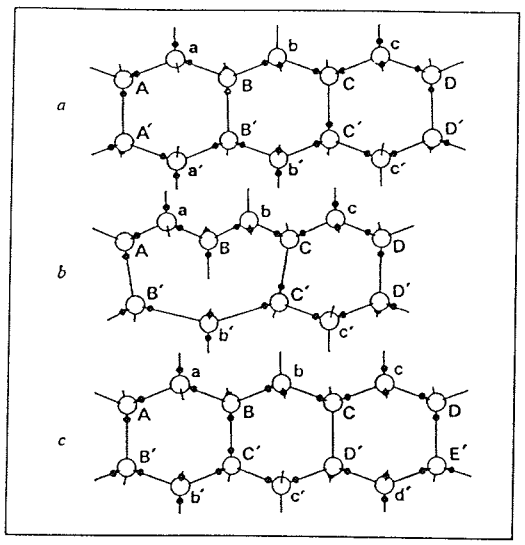

Fig. 2.6 - One example of dislocation glide in the basal plane of ice.
a) Undisturbed crystal lattice (with protons arranged according to the Bernal-Fowler rules), viewed along a direction perpendicular to the c-axis. **b)** The dislocation at an intermediate position between a) and c), having moved atom A to join B′. **c)** The top part in a) has sheared to the right relative to the bottom part by the passage of the dislocation. Note that a pair of Bjerrum defects has formed during this process.

10^8 m^{-2}, but deformation leads to an increase in dislocation density by several orders of magnitude.
Dislocations can originate at various sources, the most important being the boundaries between grains, where local stress concentrations can arise. After being emitted from a grain boundary into the lattice, a dislocation can multiply during grain deformation, resulting in an increase in dislocation density.
Dislocations move through a crystal lattice by two basic types of movement; glide and climb. Glide can be envisaged as sliding or successive displacement of one plane of atoms over another on so-called slip-planes, giving rise to plastic deformation of the crystal. The slip planes are normally the planes with the highest density of atoms, which in ice crystals are the basal planes. Dislocation glide on the basal plane of ice is illustrated in Fig. 2.6.
During climb, a dislocation moves out of its slip plane and continues in an adjacent plane. This process is also believed to play a role in the deformation of polycrystalline ice.

The direction of slip is the direction in the slip plane in which the atoms are most closely spaced. In ice these are the crystallographic directions $[11\bar{2}0]$, $[\bar{2}110]$ and $[1\bar{2}10]$, parallel to the three a-axes (see Fig. 2.2). Experiments have, however, shown that no preferred glide direction exists in the basal plane and thus an ice crystal will deform in the direction of the shear stress applied to it, irrespective of the orientation of the a-axes. According to Kamb (1961), this behaviour is due to simultaneous glide in the three directions indicated above, during non-linear response of the crystal to the applied shear stress.
Geometrically, dislocations can also glide on the prismatic and pyramidal planes in ice crystals, but experiments have shown that much greater stress is required for deformation to occur along these planes than on the basal plane.
The velocity of dislocations depends on the applied shear stress, the temperature, the presence of defects and the type of dislocation.
The distortion of a crystal lattice caused by a dislocation produces stress fields in its vicinity. For example, the edge dislocation depicted in Fig. 2.5 will exert a compressive stress above the slip plane, and the region immediately below it will be in tension. From knowledge of the elastic stress field, the energy of a dislocation can be found according to

$$E = K b^2 \ln (R/r_o) \qquad (2.1)$$

where

K = factor which is dependent upon the elastic constants and on the orientation of the dislocation.
b = length of the Burgers vector, **b**.
R = the average distance between dislocations.
r_o = dislocation core radius, which in most cases lies in the range b to 4b, giving $r_o \leq 1$ nm.

2.2 DEFORMATION OF ICE

Stress and strain

When a force δF is applied to a body, stress is defined as the ratio of the force to the area δA on which the force is applied, according to

$$\sigma = \frac{\delta F}{\delta A} \qquad (2.2)$$

Stress has units of N/m^2 in the SI system, and this unit is also termed Pascal (1 Pa = 1 N/m^2). In glaciology, it is still common to express stresses in bars; 1 bar = 10^5 Pascal.

The stress at any point within a body is found by taking the limit of the quantity above as δA tends to zero, according to

$$\sigma = \lim_{\delta A \to 0} \frac{\delta F}{\delta A} = \frac{dF}{dA} \qquad (2.3)$$

If a force is perpendicular to the area it acts on, the stress is said to be a normal stress; if it acts tangentially to an element of area the stress is a shear stress. A force which is applied neither parallel nor perpendicular to an element of area can be resolved into normal and shear stress components.

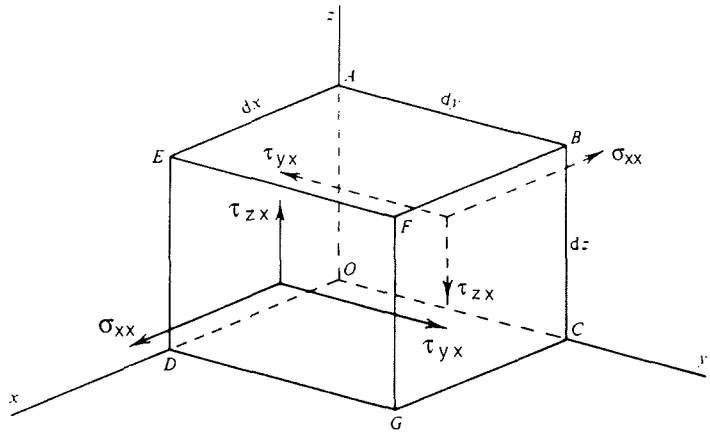

Fig. 2.7 - Stress components acting on a cubic volume element inside a body.
All stresses acting on each of the six sides of the element can be resolved into components parallel to the coordinate axes, as shown for the two sides perpendicular to the x-axis. σ_{xx} denotes a stress parallel to the x-axis, τ_{yx} a stress parallel to the y-axis acting upon a surface perpendicular to the x-axis, and similar for τ_{zx} (σ is normally used to denote normal stresses, and τ shear stresses).
In the limit, as the stresses acting at a single point are considered, the number of stresses reduces to the six independent entries of the stress tensor.

A total of nine stress components (3 normal and 6 shear components) are required to completely determine the state of stress at a given point. The notations of those components are explained in Fig. 2.7 and they are said to define the stress tensor at the point:

$$\begin{bmatrix} \sigma_{xx} & \tau_{xy} & \tau_{xz} \\ \tau_{yx} & \sigma_{yy} & \tau_{yz} \\ \tau_{zx} & \tau_{zy} & \sigma_{zz} \end{bmatrix} \qquad (2.4)$$

Of the 9 components of the stress tensor, only 6 are completely independent, since it can be shown that $\tau_{xy} = \tau_{yx}$, $\tau_{xz} = \tau_{zx}$ and $\tau_{yz} = \tau_{zy}$. By an appropriate change of coordinates a given stress tensor can always be expressed in diagonal form, where the only non-zero terms are the diagonal ones, σ_{xx}, σ_{yy} and σ_{zz}. These are called the principal stresses (Jaeger, 1962).

Fig. 2.8 illustrates the most important stress systems encountered in different parts of ice sheets and glaciers. Uniaxial compression or pure shear normally dominates in the upper parts of large ice sheets, but at least one example is known of tension dominating (Vostok, Antarctica - see Lipenkov et al., 1989). Simple shear usually dominates in the lowermost 10-15% of the ice thickness.

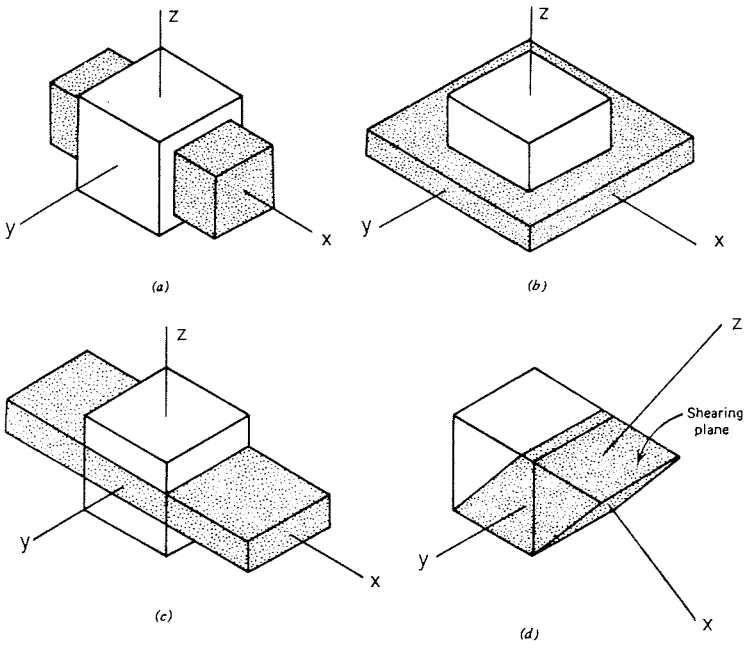

Fig. 2.8 - Major stress systems. In each case the cube represents the undeformed state and the stippled figure represents the deformed state. The x, y and z axes represent the principal stress directions. **a)** Uniaxial extension (for which the strains are $\varepsilon_y = \varepsilon_z = -\varepsilon_x/2$). **b)** Uniaxial compression ($\varepsilon_x = \varepsilon_y = -\varepsilon_z/2$). **c)** Pure shear ($\varepsilon_x = -\varepsilon_z$; $\varepsilon_y = 0$). **d)** Simple shear.

Strain is the change in shape and dimensions of a body which results from a stress (or stresses) acting on it. Fig. 2.9 shows a solid being subjected to compressive stress. The (compressive) normal strain experienced by the solid in the z-direction is

$$\varepsilon_z = \frac{l - l_o}{l_o} \qquad (2.5)$$

and the (tensional) normal strain in the x-direction is defined in a similar way. Normally, extension is taken as positive and compression as negative strain, but this convention is usually not strictly followed. It is also common to express strain in %; 20 % compressive strain then meaning that a sample has been compressed to 80% of its original thickness.

Shear strain is measured as the change in angle between two lines in a material, which originally were perpendicular. Fig. 2.10 illustrates a solid being deformed in simple shear. The shear strain is defined as

$$\varepsilon = \frac{d}{l} = \tan\beta \qquad (2.6)$$

and is thus seen to be < 1 for $\beta < 45°$ and > 1 for $\beta > 45°$.

Strain rate is the rate of deformation, expressed as strain/unit time and denoted $\dot{\varepsilon}$. Strain is dimensionsless, strain rate has dimensions $(\text{time})^{-1}$.

Fig. 2.11 shows the schematic flow pattern in an ice sheet and the major modes of deformation operating. Pure shear dominates at an ice divide, simple shear near the bottom. Irregular bedrock topography can cause large variations in the stresses near the bottom. The hydrostatic pressure (stress) at any depth in the ice sheet is given by

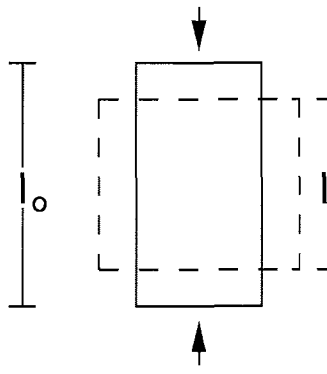

Fig. 2.9- Shapes of a solid before (stippled) and after (full) compression.

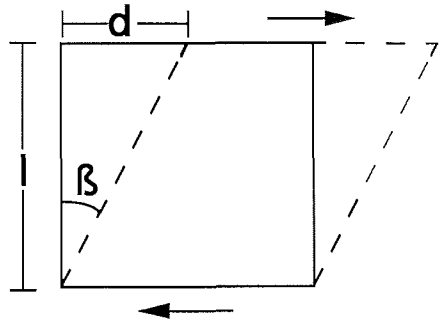

Fig. 2.10 - Before (left) and after (right) simple shear deformation of a solid.

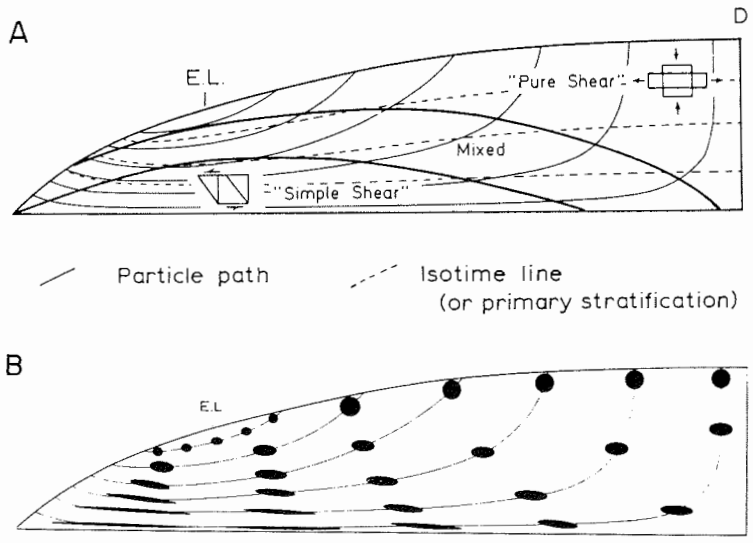

Fig. 2.11 - **a)** Schematic flow patterns in an ice sheet. D = ice divide, E.L. = equilibrium line. Pure shear deformation dominates at the ice divide, simple shear near the bottom. **b)** Illustrating the total strain at selected points along particle paths shown in a). Initial circles become deformed into ellipses during flow. - From Hooke & Hudleston (1978).

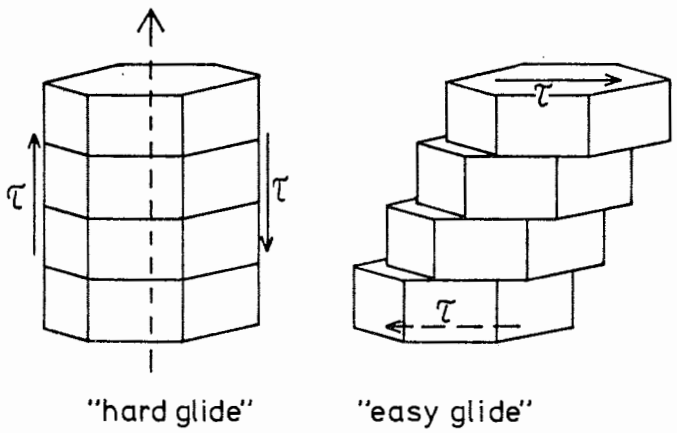

Fig. 2.12 - Illustrating how the deformation of a single crystal is dependent on the direction of the applied stress.

$$\sigma = \rho g h \qquad (2.7)$$

where ρ is the density of ice (920 kg/m^3 below the firn-ice transition), g is the acceleration due to gravity (9.8 m/s^2) and h is the depth below the surface. This pressure thus is about $9*10^6$ Pa = 90 bar at 1 km depth in ice and 270 bar at the bottom of the Central Greenland ice sheet, at 3 km depth.
The flow law of ice (the relation between applied stress and the resulting rate of deformation) is, however, generally assumed to be unaffected by hydrostatic pressure (Paterson, 1994) and it is thus normal practice to work with stress deviators, rather than stresses. The stress deviators are obtained by subtracting the amplitude of the hydrostatic pressure from each normal-stress component (Jaeger, 1962).

Deformation of single ice crystals

When stress is applied to a single crystal, the resulting deformation is highly dependent on the direction of the stress relative to the direction of the c-axis. A stress applied parallel to the basal planes causes easy glide of the planes over each other, whereas the crystal is hard against a stress applied parallel to the c-axis (Fig. 2.12). The rapid basal glide, which is the main deformation mechanism in ice, is due to the relatively easy movement of dislocations on the basal plane. Non-basal glide can occur by dislocation movement on the prismatic and pyramidal planes, but at least 60 times higher stress is required for such deformation to occur at the same strain rate (Duval et al., 1983).

A creep curve shows the change in strain with time in a sample being deformed by constant stress. Fig. 2.13 shows a typical creep curve for a single crystal of ice. The strain rate increases in the beginning, but reaches a steady value after ≈20% deformation. The initial increase is believed to be due to dislocation multiplication, but once the dislocation density has reached a value which is in balance with the applied stress, a stationary strain rate is established.

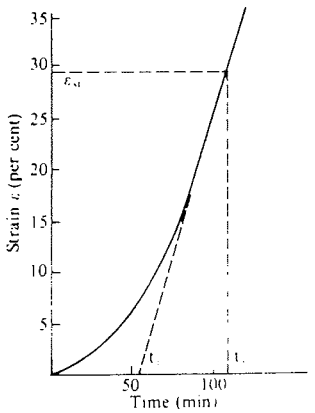

Fig. 2.13 - A typical creep curve for a single crystal of ice, deforming by basal glide. From Higashi et al. (1965).

A simple relationship between strain rate and dislocation density will now be derived, following the approach of Hull & Bacon (1984 - p. 68-69):

Fig. 2.14 shows a crystal of volume hld being deformed by shear stress, acting on the slip plane parallel to the Burgers vector **b**. The dislocations glide on the slip planes and the top surface is displaced relative to the bottom surface. A dislocation which moves completely across the slip plane through the distance d, contributes to the total displacement D by the amount b; the length of the Burgers vector. Since b is small in comparison to d and h, the contribution made by a dislocation which moves a distance x_i may be taken as the fraction x_i/d of b. Thus, if the number of dislocations which move is N, the total displacement is

$$D = \frac{b}{d} \sum_{i=1}^{N} x_i \qquad (2.8)$$

and the shear strain ε experienced by the crystal is given by

$$\varepsilon = \frac{D}{h} = \frac{b}{hd} \sum_{i=1}^{N} x_i. \qquad (2.9)$$

This can be simplified by noting that the average distance a dislocation moves is

$$\bar{x} = \frac{1}{N} \sum_{i=1}^{N} x_i \qquad (2.10)$$

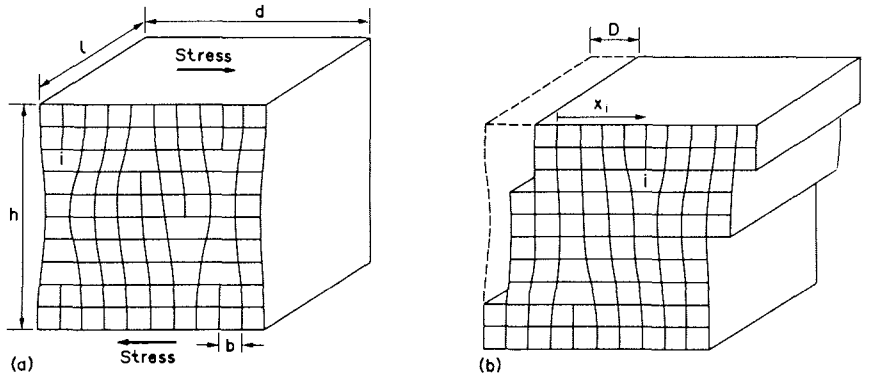

Fig. 2.14 - a) Edge dislocations in a crystal subjected to an external shear stress resolved for slip. **b)** Plastic displacement D produced by glide of the dislocations. Dislocation i has moved a distance x_i, as shown.

and that the density of mobile dislocations ρ_m is (Nl/hld) - the total length of dislocation line per unit volume. Hence

$$\varepsilon = b\rho_m\bar{x} \tag{2.11}$$

and the strain rate is therefore

$$\dot{\varepsilon} = \frac{d\varepsilon}{dt} = b\rho_m\bar{v}, \tag{2.12}$$

where $\bar{v}$ is the average dislocation velocity. These relations can also be shown to apply for a crystal which is deformed in tension by dislocation climb.

Deformation of polycrystalline ice

A sample of polycrystalline ice with randomly oriented c-axes deforms much slower than a single crystal under the same stress, since most of the crystals will not be favourably oriented for basal glide. The strain rate of a polycrystal during secondary creep is 2-3 orders of magnitude lower than for a single crystal having the most favourable orientation for shear (Lliboutry & Duval, 1985). Each crystal in a polycrystalline aggregate will be confined by its neighbours and thus other mechanisms, in addition to dislocation glide, contribute to the deformation. Among these are grain growth, grain boundary migration, grain boundary sliding, diffusion, distortion of the lattice and recrystallization (Hobbs, 1974; Alley, 1992; Paterson, 1994).

Extensive deformation tests have been carried out on artificial and natural ice samples in the last decades (e.g. Glen, 1955; Steinemann, 1958; Kamb, 1972; Duval, 1981; Jacka & Maccagnan, 1984; Dahl-Jensen et al., 1996). Fig. 2.15 shows a typical creep curve for polycrystalline ice deformed at constant stress. Four stages of deformation are observed:

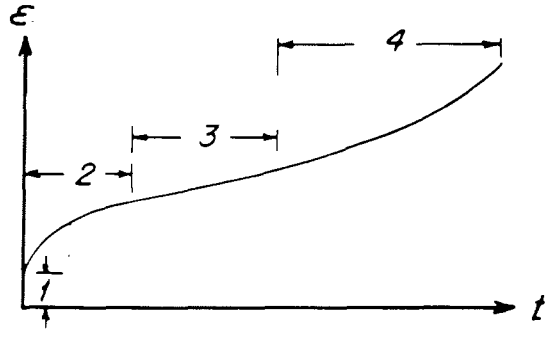

Fig. 2.15 - a) A typical strain-time curve for polycrystalline ice deformed under constant stress. See text for explanations.

1. An initial elastic deformation.

2. A stage of decelerating creep, termed transient or primary creep. The hardening in this stage is ascribed to interference between grains with different orientations. Initially, those grains which are oriented for basal glide deform, and load is gradually transferred to the "hard" grains, whereby the strain rate decreases.

3. A stage in which the creep rate reaches a minimum and becomes constant for a time. This steady secondary creep probably results from a temporary balance between hardening in parts of the sample and softening elsewhere, by recrystallization at grain boundaries and/or dislocation climb.

4. A stage of accelerating creep, referred to as tertiary creep. The increased creep rate in this stage is usually attributed to recrystallization, producing grains which are more favourably oriented for basal glide. Formation of microcracks and dislocation multiplication may also play a role. A steady strain rate is usually reached in tertiary creep, if the test is carried out long enough.

The strain rate in each test is, of course, strongly dependent on the magnitude of the applied stress and on the temperature. The minimum (secondary) creep rate, however, always appears to be reached when the total strain reaches about 1%, irrespective of the stress and temperature (Jacka, 1984b). Laboratory tests are typically carried out to 10-20% strains, but much higher strains can be attained in natural ice masses.

The flow law for ice

Deformation of a material can be described by the so-called constitutive relation, a formula which relates the applied stress to the resulting strain rate. For an elastic material, strain is proportional to stress (Hooke's law) and the relation is thus $\varepsilon = k\sigma$. For a Newtonian viscous material, strain rate is proportional to stress and hence $\dot{\varepsilon} = k\sigma$. In a perfectly plastic material, no deformation occurs until a critical yield stress is reached; then rapid deformation begins.

The deformation of ice during flow of natural ice masses can be described as intermediate between Newtonian viscous and perfectly plastic behaviour. Laboratory creep tests have established that the constitutive relation, normally referred to as the flow law (or Glen's law), can be expressed as

$$\dot{\varepsilon} = A\sigma^n \qquad (2.13)$$

where $\dot{\varepsilon}$ is the strain rate, σ the stress deviator, n is the power law constant and A is a factor which depends on temperature according to the Arrhenius relation: $A = A_0 \exp(-Q/RT)$. Here Q is the activation energy for creep, R is the universal gas constant and T is the temperature. The value of A_0 depends on ice fabric, grain size and impurity content, along with other factors.

Results from field and laboratory studies indicate that $n \approx 3$ and this is the value usually adopted in modelling studies. The exponent 3 can be derived from dislocation theory: The dislocation density ρ is proportional to σ^2 and the dislocation velocity $v \sim \sigma\exp(-Q/RT)$; insertion in (2.12) thus yields $\dot{\varepsilon} \sim \exp(-Q/RT)\sigma^3$ (Weertman, 1983).

The flow law with n = 3, however, cannot be considered to apply at all locations in glaciers and ice sheets, since it depends on widely varying deformation mechanisms and stress systems. For example, an exponent of n = 1 (i.e. Newtonian viscosity) could be more appropriate under low-stress conditions in the upper parts of polar ice sheets (Lliboutry & Duval, 1985; Alley, 1992). Suggested processes leading to ice flow with n = 1 include diffusional creep, superplasticity and dislocation creep with a constant dislocation density (Weertman, 1983; Lliboutry & Duval, 1983).

It is clear from the Arrhenius term that ice deforms slower at lower temperatures. Assuming Q = 60 kJ/mol (Paterson, 1994), the strain rate produced by a given stress at -10 °C is about 5 times that at -25 °C.

The factors which contribute to the value of A_0 have not been quantified, but important insights have been gained. Some soluble impurities, like HF and HCl are known to increase the creep rate of single crystals by factor 10, at concentrations of few parts per million. Whether solid inclusions like sand or silt also soften the ice is not clear (Paterson, 1994).

Laboratory tests have shown that the minimum (secondary) creep rate is independent of crystal size and also that the tertiary creep rate is independent of the initial crystal size (Jacka, 1984a). An equilibrium crystal size has been shown to develop in tertiary creep, resulting from a balance between crystal growth and deformation effects tending to reduce crystal size (Jacka & Li Jun, 1995).

The effect of c-axis fabrics on flow rates has recently been discussed in the literature (Dahl-Jensen & Gundestrup, 1987; Paterson 1991). Results of some deformation tests indicate that the flow of anisotropic ice (with a preferred fabric) is strongly enhanced as compared to isotropic ice with a random fabric (Pimienta et al., 1988; Shoji & Langway, 1988). The difference in flow rates is usually expressed by the use of an enhancement factor; the ratio of the flow rates of anisotropic and isotropic ice. The effect of fabrics and crystal sizes on flow properties will be discussed further in a later section.

2.3 RECRYSTALLIZATION PROCESSES IN POLAR ICE

Ice in polar ice sheets is continually recrystallizing to accommodate changes in temperature and stress-strain conditions. This involves changes in size, shape and orientation of existing crystals, bending and fragmentation of crystals under stress and the nucleation and growth of entirely new crystals. The recrystallization and deformation processes in ice show many similarities to those observed in metals, ceramics and rocks, and consequently theories developed for metallurgical systems and geological materials have been applied to polar ice.

A few words on (the sometimes confusing) terminology are needed before proceeding further. In metallurgy, distinction is made between primary, secondary and tertiary recrystallization (Gottstein & Mecking, 1985). The first process is the crystallization of a strongly deformed structure, whereas the other two terms refer to the growth of a few grains to large sizes while others do not grow at all. Secondary recrystallization is sometimes termed abnormal grain growth, in contrast to normal grain growth, which refers to a homogeneous increase in grain size (see below). In addition, distinction is made between static recrystallization, which occurs during heat treatment (annealing) in the absence of external stresses, and dynamic recrystallization, which occurs during active deformation. Most of the above terms have been used in the geological literature (e.g. Urai et al.,1985; Guillopé & Poirier 1979; Poirier, 1985; Gottstein & Mecking, 1985).

In polar ice sheets, three major recrystallization regimes have been identified (Alley, 1992; Duval & Castelnau, 1995). The terminologies used by these authors are shown in Table 2.1. Below, Alley's terms for the two upper regimes will be used, and Duval & Castelnau's term for the lowest regime; migration recrystallization. Paterson (1994) uses the term dynamic recrystallization for this regime.

RECRYSTALLIZATION REGIMES — **TABLE 2.1**

Alley, 1992	Duval & Castelnau, 1995	DESCRIPTION	OCCURRENCE
Normal grain growth	Grain growth	Steady increase in average grain size	Upper few hundred meters of polar ice sheets
Polygonization	Rotation recrystallization	Bending and fragmentation of existing grains	Dominates between other two regimes
Recrystallization	Migration recrystallization	Nucleation and rapid growth of new grains	Lowest few hundred meters (if T high enough)

Table 2.1 - Alternative descriptions of the main recrystallization regimes in polar ice sheets.

1. Normal grain growth

Normal grain growth is the approximately linear increase in average grain area with time observed in the upper 400-700 m of polar ice sheets (both in firn and ice). Two main aspects of this process are:

1. The range of grain sizes and shapes is relatively narrow.
2. The grain-size distribution, normalized by the mean grain size, does not vary significantly with age.

Theories of normal grain growth have been developed in metallurgy over the past 50 years (Atkinson, 1988). The basic underlying assumption is that grain boundaries migrate by atom transport due to surface curvature, the driving force of this process being the decrease in free energy which accompanies reduction in total grain boundary area. The so-called mean field theories, developed by Feltham (1957), Hillert (1965) and Louat (1974), deal with the change in size of an isolated grain embedded in an environment which represents the average effect of the whole array of grains. The grain-growth law which results from these theories is of the form

$$D^n = k\,t \tag{2.14}$$

where D is the average grain diameter, k is a constant, t is time and n=2. This law is supported by observations, which show that grain diameter grows as the square root of t, or somewhat slower (i.e. $2 \leq n \leq 3$ in most cases).
Below, a simplified derivation of the parabolic growth law will be given, following mainly approaches given by Kingery et al. (1976) and Gottstein & Mecking (1985).

As an analogy to a single grain embedded in the averaged environment of other grains, consider a spherical bubble blown from a capillary as illustrated in Fig. 2.16. A negligible density difference between the bubble material and the surrounding medium is assumed and thus the only resistance to the expansion of the bubble is the increased surface area being formed and an associated increase in surface energy. Thus, at equilibrium, the work of expansion $W = \Delta P\,dV$ equals the increased surface energy $\gamma\,dA$, giving

$$\Delta P\,dV = \gamma\,dA \tag{2.15}$$

$$\Rightarrow \qquad \Delta P\,(4\pi r^2\,dr) = \gamma\,(8\pi r\,dr)$$

$$\Rightarrow \qquad \Delta P = \gamma \frac{dA}{dV} = \gamma \frac{8\pi r dr}{4\pi r^2 dr}$$

$$\Rightarrow \qquad \Delta P = \frac{2\gamma}{r} \tag{2.16}$$

where ΔP is the pressure, dV is a volume element, r is the radius of the bubble and γ is the surface energy [J/m^2].

In case of a non-spherical shape of the surface, similar reasoning leads to the result

$$\Delta P = \gamma\left(\frac{1}{r_1} + \frac{1}{r_2}\right) \qquad (2.17)$$

where r_1 and r_2 are the principal radii of curvature.

A pressure difference ΔP thus arises across the surface and causes the liquid in the bubble to rise in the capillary. Similarly, a pressure difference exists across the curved boundaries separating a grain in ice from the grains surrounding it (Fig. 2.17). Since a boundary between two grains will usually bow into the larger grain, the pressure will be directed towards it, causing molecules to jump from the smaller grain across the boundary. The boundary will thus move towards the center of the smaller grain, which eventually is consumed by the larger grains surrounding it.

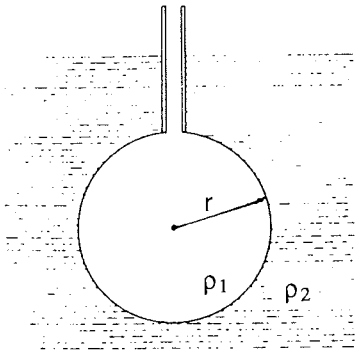

Fig. 2.16 - A bubble of material 1 is blown into a medium of material 2; with $\rho_1 \approx \rho_2$. A pressure difference across the curved boundary is required to maintain a spherical surface of radius r.

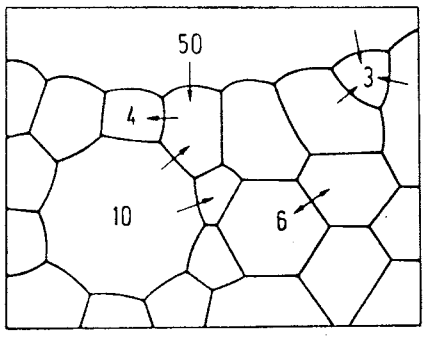

Fig 2.17 - Illustrating grain growth in a polycrystalline material. The figures indicate the number of edges of each grain. Pressure will normally be directed from the smaller grain to the larger (from the concave side of a boundary), causing atoms to jump across the boundary to the larger grain. The boundary therefore moves into the smaller grain, as indicated by the arrows. Ideally, grains with fewer than 6 edges will shrink, those with more than 6 edges will grow. Grains with 6 edges and straight boundaries will be in equilibrium. - Note that only grains with < 6 edges and concave boundaries are analogous to the bubble in Fig. 2.17.

The velocity of a moving boundary is proportional to the pressure difference according to

$$v = M \cdot \Delta P \qquad (2.18)$$

where M, the mobility of grain boundaries, depends on temperature according to the Arrhenius relation

$$M = M_o \exp(-Q/RT) \qquad (2.19)$$

where M_o is a constant, Q is an activation energy (J/mol), R is the gas constant (8.314 J/K mol) and T is the absolute temperature.

Assuming that the radius of curvature of a grain is proportional to the average grain diameter ($r = \alpha D$) and that the grain diameter (D) varies proportionally to the average velocity ($v = \beta\, dD/dt$), equations (2.16) and (2.18) combine to

$$v = M \cdot \Delta P$$

$$\Rightarrow \qquad \beta \frac{dD}{dt} = M \frac{2\gamma}{r} = M \frac{2\gamma}{\alpha D}$$

$$\Rightarrow \qquad D\, dD = \frac{2M\gamma}{\alpha\beta}\, dt$$

which integrates to

$$\boxed{D^2 = D_o^2 + k \cdot t} \qquad (2.20)$$

where D is the average diameter at time t, D_o is the average diameter at time t = 0, and $k = k_o \exp(-Q/RT)$ is the growth rate, which normally is expressed in mm^2/yr.

The parabolic growth relation (2.20) thus predicts the average area of grains increases linearly with time. Several studies have shown that this relation can be applied to grain growth in polar firn (e.g. Gow, 1969; Stephenson, 1967; see also Paterson, 1994). Gow & Williamson (1976) showed that it also applies to normal grain growth in the top 4-500 m of ice in the Byrd deep ice core.

Paterson (1994) has compiled data on grain growth for different temperatures at various polar sites. These data are depicted in Fig. 2.18, where lnk has been plotted against the reciprocal of T. The slope of the regression line through the data points yields the activation energy for grain growth, which according to these data is Q = 42.5 kJ/mol. This compares well with the experimentally determined activation energy of 40.6 kJ/mol for grain boundary

self-diffusion in ice (Paterson, 1994), which is the appropriate activation energy here since diffusion of molecules is the process by which grain boundaries migrate.

2. Polygonization

In most deep ice cores, the increase in grain size by grain growth has been observed to cease below a depth of 400-700 m. This has been suggested to result from a process called polygonization, i.e. bending and eventually subdivision of individual crystals under increasing strain in the ice (Alley, 1992; Alley et al., 1995). Polygonization, which also has been termed rotation recrystallization (Poirier, 1985; Duval & Castelnau, 1995), has been observed to occur frequently in various naturally and experimentally deformed minerals (e.g. Guillope & Poirier, 1979; Urai et al., 1986). In ice sheets, the tendency of grain size to increase by surface-energy driven grain growth is still present in this regime, but is counteracted by the subdivision process so that the grain size stays nearly constant.

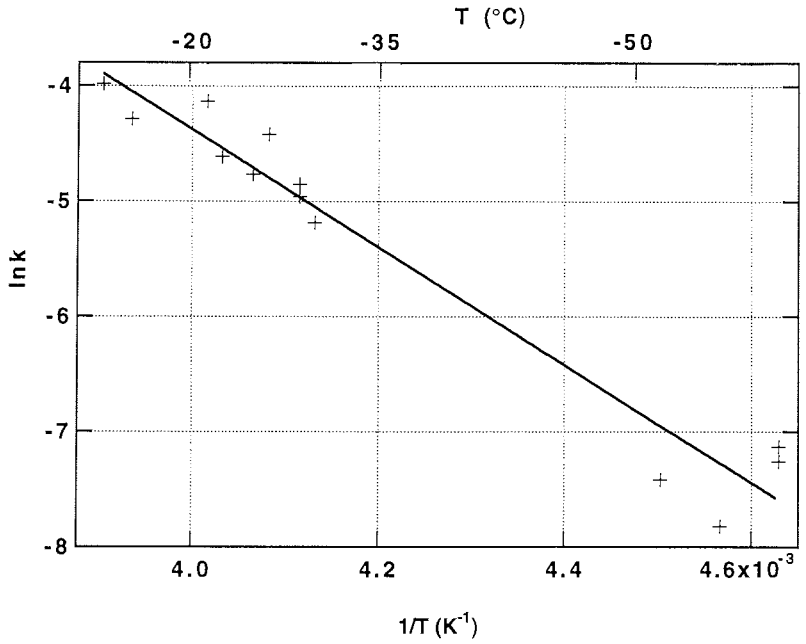

Fig. 2.18 - Crystal growth data from various polar sites. The natural logarithm of the growth rate k (mm^2/yr) is plotted versus the reciprocal of the absolute temperature (K). The growth rate follows the Arrhenius relation $k = k_0 \exp(-Q/RT)$, giving $\ln k = \ln k_0 - Q/RT$. Regression analysis of the data yields a value of 16.06 for the intercept ($\ln k_0$) and -5109.9 for the slope (-Q/R). Thus $k_0 = 9.5*10^6$ mm^2/yr and the activation energy is Q = 5109.9 K * 8.314 J/K mol = 42.5 kJ/mol.
The data compiled by Paterson (1994, p. 24) have been used in this graph. Duval (1985) obtained an activation energy of 52 kJ/mol from a different data set.

The mechanism of polygonization is illustrated in Fig. 2.19. The lattice of a deforming crystal rotates and acquires a curvature, leading to an increase in the dislocation density, and thus in the elastic strain energy. The dislocations will tend to rearrange themselves into configurations of lower energy, resulting in the formation of sub-grain boundaries (or low-angle grain boundaries). They separate regions of a crystal which differ in lattice (and c-axis) orientation by a few degrees. The sub-grain boundaries gradually develop into full grain boundaries and when the misorientation angle has reached ≈15°, it is appropriate to speak of separate grains rather than sub-grains (Poirier, 1985).
Since strain increases downward in ice sheets, polygonization always operates below ≈ 400 m depth and acts to reduce average grain size. Its effects can be overridden, however, if grain growth is rapid enough.

3. Migration recrystallization

In short, this process can be defined as the nucleation and growth of entirely new grains by rapid migration of grain boundaries. In polar ice sheets, this type of recrystallization only occurs above a critical temperature close to -10 °C (Duval & Castelnau, 1995). Generally, the recrystallization nuclei have a different orientation than the surrounding grains; i.e. are separated from them by high-angle grain boundaries (Alley, 1992). Large, interlocking grains in the bottom 350 m of the Byrd ice core are believed to have been formed by this process (Gow & Williamson, 1976; Duval & Castelnau, 1995).

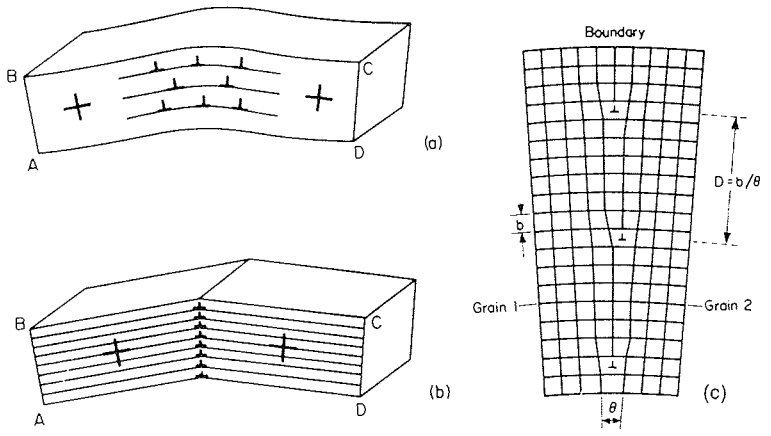

Fig. 2.19 - Formation of a sub-grain boundary. **a)** Bent crystal with edge dislocations in random positions. Each inverted T denotes one extra plane of atoms in the lattice, moving on a glide plane. **b)** The dislocations have rearranged to form a sub-grain (or low-angle) grain boundary. **c)** A closeup view of the low-angle boundary. The extra planes of atoms, positioned above each other, cause misorientation of the lattice and eventually breakup of the grain into two separate grains (for $\theta > 15°$).

In this case, grain boundary migration is not driven by the pressure difference induced by the curvature of grain boundaries. The newly nucleated grains will have very small initial sizes (< 1mm) and thus the process requires these small grains to grow into larger ones (whereas during normal grain growth smaller grains are consumed). The driving force of this recrystallization process is the difference in stored strain energy between old grains, which have a high dislocation content, and new, dislocation-free grains (Fig. 2.20). For recrystallization to occur, this driving force must exceed the curvature-induced stress $2\gamma_{GB}/r$ (eq. 2.16), which causes boundaries to move towards their center of curvature. Here $\gamma_{GB} = 0.065$ J/m^3 is the grain boundary energy (Hobbs, 1974) and r is the radius of curvature. Duval et al. (1983) took r = 0.1 mm and obtained a necessary stored strain energy for recrystallization of $\approx$1000 J/m^3.

If stress is applied to an ice sample, internal stress of an equal magnitude arises from the elastic fields of dislocations produced by the deformation. The stored strain energy associated with the dislocations has been shown to be much lower than that required to initiate recrystallization, by 1-2 orders of magnitude. However, strain energy of sufficient magnitude can be reached in crystals which are unfavourably oriented for basal glide (Duval et al., 1983), and Alley (1992) pointed out other mechanisms which might explain the above mentioned contradiction.

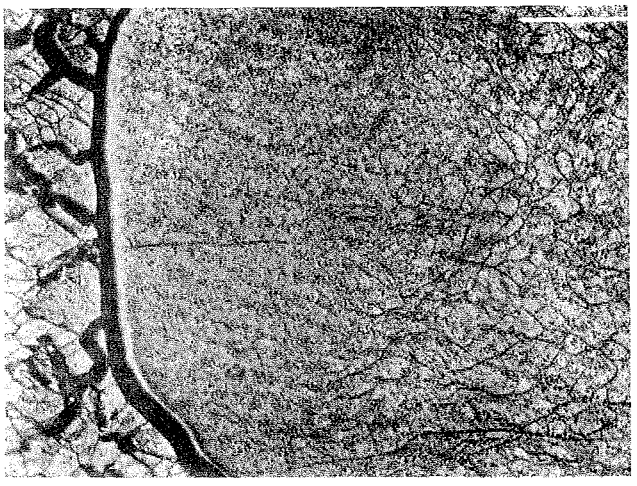

Fig. 2.20 - Migration recrystallization on a small scale in NaCl. The large grain boundary is moving to the left and a heavily strained (polygonized) grain structure is being consumed by a new, strain-free grain. This grain, in turn, is becoming polygonized to the right. Scale bar = 0.1 mm. (From Guillopé & Poirier, 1979.)

Impurity effects

In all three recrystallization regimes outlined above, grain boundary migration occurs, under differing conditions and driving forces. Studies in metallurgy and on geological materials have shown that second-phase particles or chemical impurities, which are present at the grain boundaries, can significantly slow their migration and even completely stop it (Hillert, 1965; Lücke & Stüve, 1971). Poirier & Guillopé (1979) have considered two possible modes of grain boundary migration when impurities are present:

1. Slow migration of the boundary when it is unable to break away from the impurities and must drag them along with it as it migrates.
2. Fast migration of the boundary, when the driving force for migration is sufficient to overcome impurity drag, and the boundary can break away from the pinning effect of the impurities.

The two cases are illustrated in Fig. 2.21. According to P. Duval (personal communication), the recrystallization processes observed in ice are readily interpreted in terms of this model of grain boundary migration rate, as indicated on the figure.
Factors which can initiate the sudden jump to fast migration include higher temperature and higher misorientation across a boundary, both of which increase the grain boundary mobility. In addition, increased deviatoric stress will increase the dislocation density and thus cause a greater driving force (Urai et al., 1986).

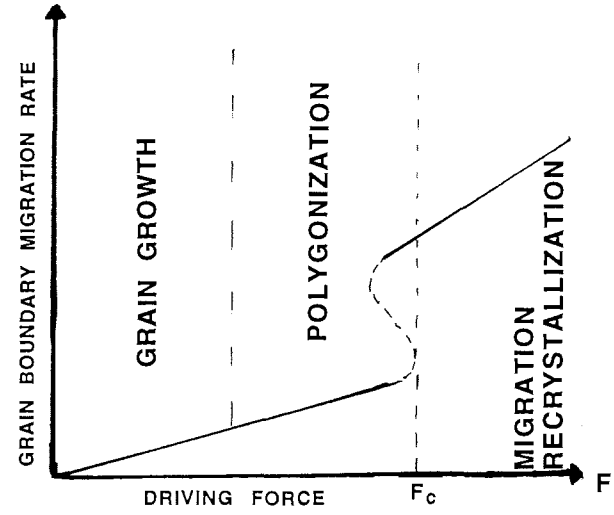

Fig. 2.21 - Schematic drawing illustrating the transition from "slow", impurity- controlled to "fast", impurity-free grain boundary migration, when a critical driving force F_c has been reached. The domains of the different recrystallization regimes in ice are indicated, as outlined by P. Duval (personal communication).

2.4 FABRIC DEVELOPMENT IN ICE

Formation of preferred fabrics

The fabric of an ice sample is the distribution of the c-axis orientations of its crystals (see Section 3.3). Straining of ice with initially random c-axis orientations normally results in changes of the fabric, the shape of the resulting fabric depending on the dominating stress system. Thus fabrics provide information on the deformational history of a sample and on its rheological properties. Quantitative relationships have been established between the magnitude of strain and fabric evolution (e.g. Azuma & Higashi, 1985; Alley, 1988; Castelnau et al., 1995).

Changes in fabric patterns are mainly due to the two following processes:

1. Rotation of c-axes due to the applied stress.
2. Recrystallization - i.e. the formation of new grains assuming special orientations.

Alley (1992; see also Paterson, 1994) has reviewed the processes of fabric formation and presented an overview of fabric development in ice sheets, shown in Fig. 2.22. The main features are:

When rotation alone is occurring, vertical compression transforms the initially random fabric to a strong single maximum, by rotation of the c-axes towards the axis of compression. Simple shear also produces a single maximum. This type of fabric development has been observed in the Byrd (Gow & Williamson, 1976), Camp Century (Herron & Langway, 1982), Dye 3 (Herron et al., 1985) and Law Dome (Li Jun, 1995) deep ice cores. In longitudinal extension, the c-axes rotate away from the axis of tension to form a vertical girdle fabric, with the girdle in a plane perpendicular to the axis of tension. This development is observed in the Vostok ice core (Lipenkov et al., 1989). - The process of grain rotation under applied stress will be described in further detail below.

When recrystallization occurs, the new crystals tend to form in positions favourable for basal glide; that is, with c-axes in intermediate positions between compressional and tensional axes so that the resolved shear stress on the basal planes reaches a maximum value. In compression and tension, this should result in the formation of the girdle fabrics shown to the right in Fig. 2.22, with the axes forming cones of half-angle $\approx 45°$, centered on the axis of compression/extension. In simple shear, a second maximum is expected to form near the shear plane. - Rotation of course continues to occur and modifies these fabrics.
Recrystallization fabrics have been produced in laboratory tests (see Budd & Jacka, 1989), normally at temperatures above -10 °C. In natural ice masses,

girdles centered on the axis of compression have been observed at shallow depths in the Ross Ice Shelf (Gow & Williamson, 1976) and at Law Dome (Budd & Jacka, 1989), and also in the deepest 100 m of the Byrd core (Gow & Williamson, 1976). The second maximum in simple shear has hitherto not been detected with certainty in deep ice cores.

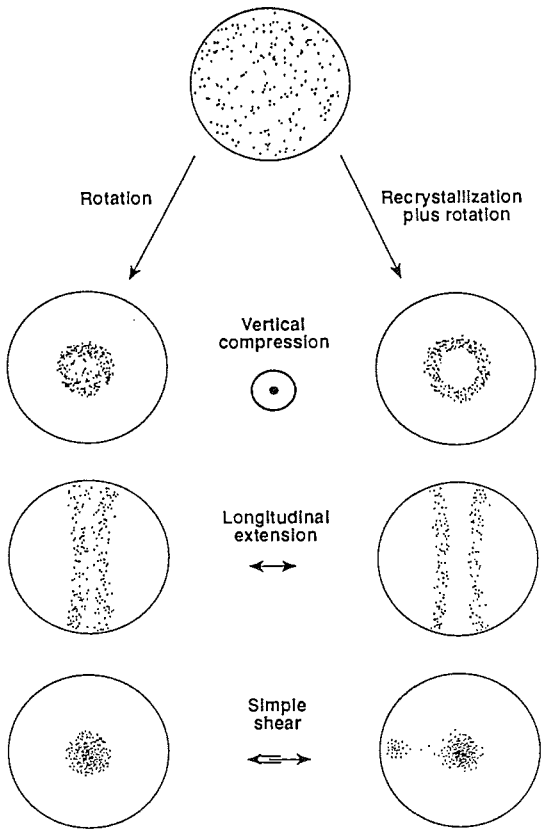

Fig. 2.22 - Fabric evolution under different stress systems in polar ice sheets. The c-axis orientations are projected into the horizontal plane, which is viewed from above. An initially random fabric transforms into different types of distributions, depending on the stress conditions. Rotation of c-axes can occur alone, or along with recrystallization. See text for further explanations. - From Alley (1992).

Rotation of c-axes

The rotation of c-axes to form a preferred orientation results from plastic deformation by slip on the basal plane, which can be directly related to the mechanics of dislocation glide (Section 2.2). Consider a crystal being deformed in vertical compression, as depicted in Fig. 2.23, with the basal planes initially in the most favourable position for slip. The basal planes would glide over each other without any change in orientation if the crystal were not constrained, resulting in rigid body rotation along with the compression. In polycrystalline ice each crystal is constrained by its neighbours, but compression will in this case be able to occur if the lattice planes themselves take up the rotation (Hobbs et al., 1976; Stander & Michel, 1989). The c-axis thus rotates towards the axis of compression. This rotation has been directly observed to take place in vertical compression tests, by placing the ice sample between crossed polarizers during the tests (Azuma & Higashi, 1985).

During deformation, no overlaps or gaps can form between grains. The individual grains must therefore adjust to the shapes of their neighbours by the migration and/or sliding of grain boundaries, along with other processes (Alley, 1992). Furthermore, the general strain of a grain by intracrystalline slip must obey the so-called von Mises condition; which dictates that at least five independent slip systems operate within the grain (von Mises, 1928; Taylor, 1938)* .The basal plane has only two independent slip systems and thus slip on the other crystallographic planes is likely to operate during deformation of polycrystalline ice, along with the grain boundary processes (Alley, 1992; Castelnau et al., 1995).

In recent years, several authors have developed models of the grain-rotation process. Azuma & Higashi (1985) modelled the evolution of fabrics in uniaxial compression, assuming that 1) The strain in each grain is proportional to the resolved shear stress in its basal plane, and 2) The bulk strain is equal to the

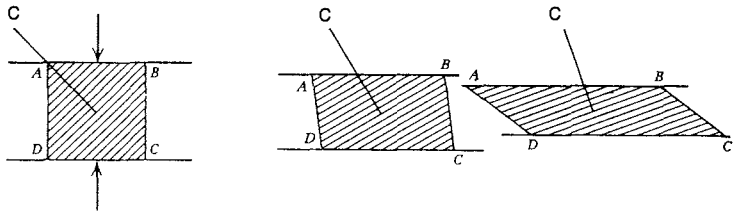

Fig. 2.23 - Rotation of the c-axis of a crystal during deformation by basal slip.

* A slip system is the combination of a specific crystallographic plane with a crystallographic direction in that plane. For example, **a** (0001) denotes the family of three slip systems on the basal plane and in the direction of one or more of the a-axes in an ice crystal. Two slip systems are said to be independent, if a shape change produced by shear on one system cannot be produced by shear on the other system (Hobbs et al., p. 77 and 125).

average strain of the individual grains in the sample. - The basic principles of this model will now be described briefly:

Consider a crystal being deformed in uniaxial compression, as shown in Fig. 2.24. The compressive stress parallel to F is $\sigma = F/A$. The force has a component $F\cos\lambda$ in the slip direction, where λ is the angle between F and the slip direction. This force acts over the slip surface which has an area $A/\cos\phi$, where ϕ is the angle between F and the normal to the slip plane (the c-axis). Thus the shear stress τ, resolved on the slip plane in the slip direction, is

$$\tau = \frac{F\cos\lambda}{A/\cos\phi} = \frac{F}{A}\cos\phi\cos\lambda \qquad (2.21)$$

In ice, the slip surface is the basal plane, and since there is no preferred glide direction on the basal plane (Kamb, 1961), $\lambda = 90 - \phi$, and $\cos\phi\cos\lambda = \cos\phi\sin\phi$. This quantity is known as the Schmid factor. The shear stress on the basal plane will be proportional to this factor, and will be maximized for $\phi = 45°$, but zero for $\phi = 0°$ and $\phi = 90°$.

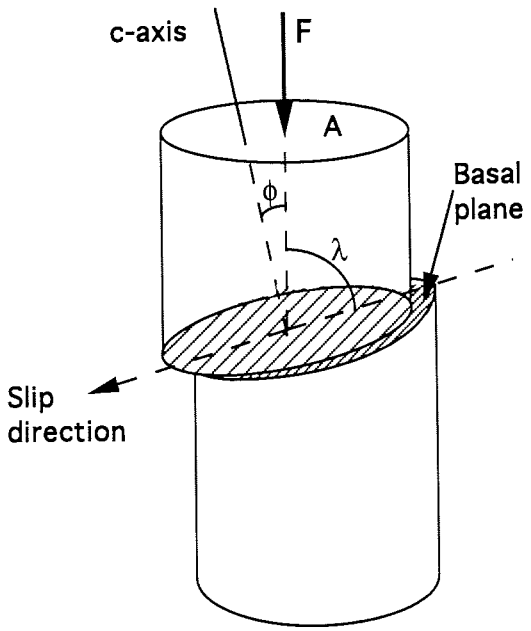

Fig. 2.24 - Geometry of slip in a single crystal under compression.

The geometrical basis of the Azuma & Higashi model (see Schmid & Boas, 1935), is shown in Fig. 2.25. The grain is compressed from thickness l_o to l, and thus experiences the strain

$$\varepsilon_g = \frac{l - l_o}{l_o} = \frac{AB\sin\phi}{AB\sin\phi_o} - 1 \qquad (2.22)$$

and thus a grain whose c-axis initially makes the angle ϕ_o with the axis of compression rotates to angle ϕ according to

$$\sin\phi = (1 + \varepsilon_g)\sin\phi_o \qquad (2.23)$$

Azuma & Higashi found experimentally that the strain ε_g of an individual grain is proportional to the resolved shear stress on the basal plane; i.e. proportional to the Schmid factor $S = \cos\phi_o \sin\phi_o$. They assumed the following relationship between ε_g and the average compressive strain ε of the whole sample:

$$\varepsilon_g = \varepsilon \frac{S}{\bar{S}} \qquad (2.24)$$

where $\bar{S} = \sum_{i=1}^{N} \cos\phi_{oi}\sin\phi_{oi}$ is the average Schmid factor for a sample of N grains

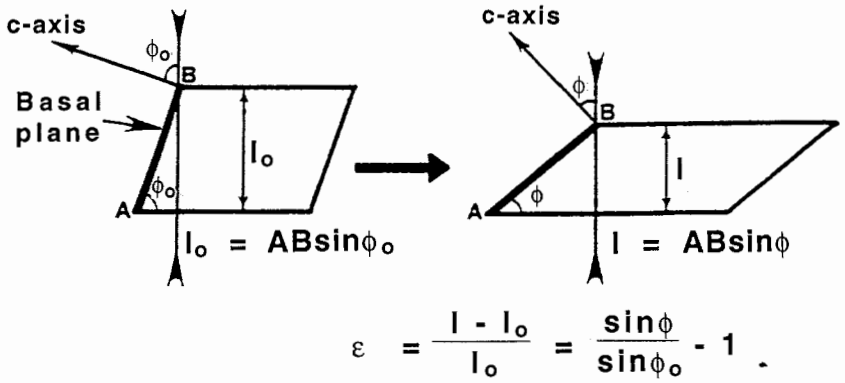

Fig. 2.25 - Geometry of c-axis rotation during compression of a crystal. - Modified after van der Veen & Whillans (1994).

at the start of the deformation. Equations (2.23) and (2.24) combine to yield

$$\sin\phi = (1 + \varepsilon\frac{S}{S})\sin\phi_o \qquad (2.25)$$

for rotation in uniaxial compression, and the corresponding equation

$$\cos\phi = (1 + \varepsilon\frac{S}{S})^{-1}\cos\phi_o \qquad (2.26)$$

applies to uniaxial tension.

The formation of the single maximum fabric in the Dye 3 core was successfully simulated with this model. The same kind of model was used to simulate fabric development in uniaxial tension in the Mizuho (Fujita et al. 1987) and Vostok ice cores (Lipenkov et al., 1989), and Alley (1988) used it for general modelling of fabric development under uniaxial and biaxial deformations.

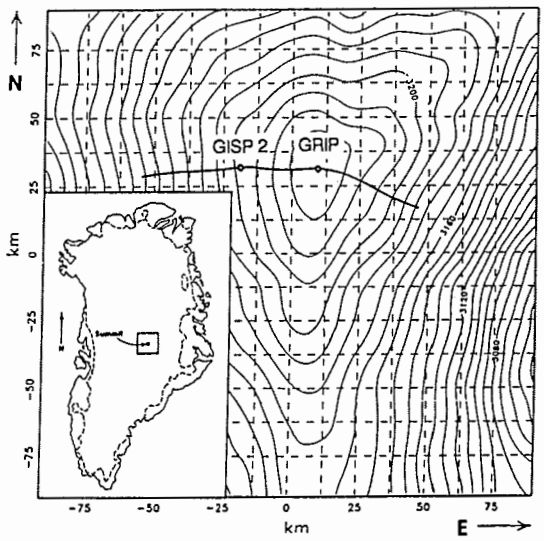

Fig. 2.26 - Surface elevation map of the Summit region, covering an area of 150x150 km. The contour interval is 8 m. - From Schøtt et al. (1992), with topographic information from Hodge et al. (1990).

2.5 THE ICE SHEET AT SUMMIT

Surface and bedrock topography

An airborne ice radar survey was carried out in the Summit area in 1987 (Hodge et al., 1990). Maps of the bedrock and surface topography covering an area of 180x180 km were produced in the study. The average thickness of the ice sheet in this region was found to be 2975 m, and the average bed altitude 180 m a.s.l. The surface map in Fig. 2.26 indicates a ridge (the ice divide) running north-south, and flanks towards the west south west, east south east and north. The GRIP drill site at the top of the dome was chosen on the basis of this map.

Hempel & Thyssen (1992) carried out surface based radio echo soundings in the Summit area, in connection with a major resurvey of the old EGIG-line across Central Greenland (Hempel, 1994). A profile of the bedrock between the GRIP and GISP2 drill sites is shown in Fig. 2.27. The GRIP borehole is

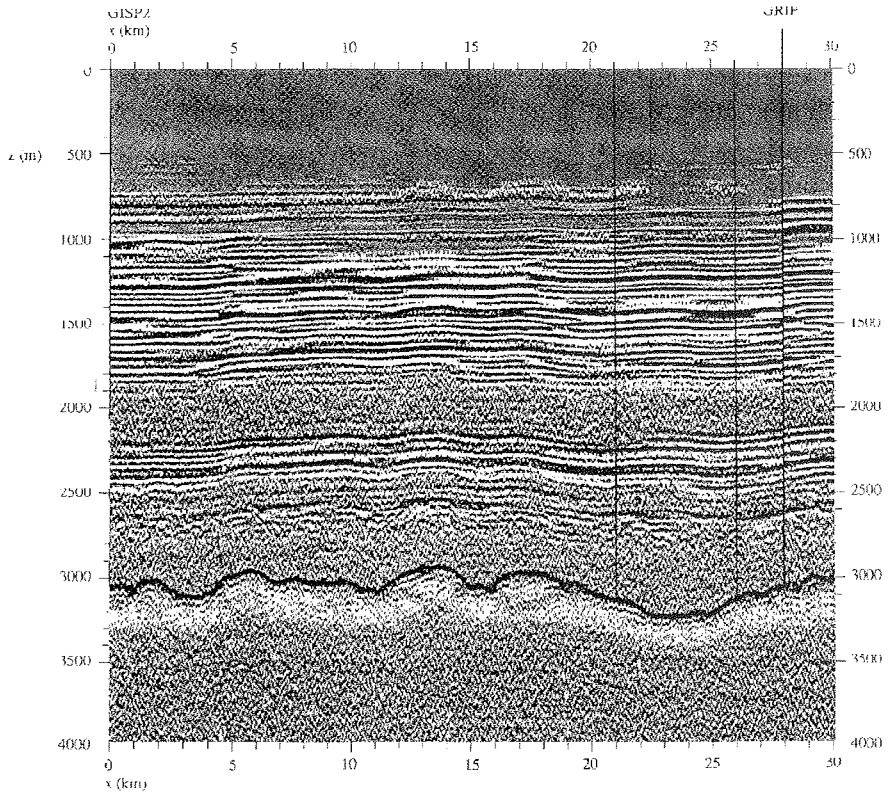

Fig. 2.27 - Radio echo sounding on a line between GRIP and GISP2. The thick, dark echo at z≈3000 m depth is the bedrock. - From Hempel & Thyssen (1992).

seen to reach the bottom on the eastern side of a 10 km wide valley, which runs north-south. The eastern side slopes gently into the valley, which is 200 m deep, but a flat bed was found within 2-300 m of the borehole (Hempel & Thyssen, 1992; Fig. 2). A north-south profile through the GRIP camp showed it to be directly above the top of a 7 km long, 150 m high hill, which runs parallel to the valley. - A map of the bottom topography, showing the same main topographic features of the region in greater detail, was produced during an airborne radar survey of the Summit area in 1994 (L. Hempel & H. Miller, personal communication).

Internal layering is also observed in the echo soundings, believed to result from layers of volcanic acid in the ice (Hammer, 1980). As seen in Fig. 2.27, these internal echoes are prominent down to 1800 m depth and in the interval 2100-2600 m, but disappear in the lowest 400 m of the ice sheet.

Ice flow regime and temperature

At an ice divide, the dominant mode of deformation is believed to be pure shear; i.e. vertical compression combined with lateral extension (Paterson, 1994). The extension would be expected to be mainly in the east-west direction at an ice divide running north south, but since Summit is located at a dome, uniaxial compression might be a more likely deformation mechanism (Fig. 2.8).

GPS surveys of ice movement have been carried out in the Summit region along with the drilling projects. A strain net was established between GRIP and GISP2 by researchers from the Technische Hochschule Braunschweig, and surveys of movement in all directions from the Summit have been carried out by the University of Copenhagen and the Danish National Survey and Cadastre. Results to date indicate very low horizontal velocities at the GRIP site; 0.2 m/yr westwards and 0.1 m/yr northwards, and 1.4 m/yr westwards at GISP2 (Keller et al., 1995). Inclination surveys of the GRIP borehole since the end of drilling have failed to detect any horizontal movement (N. Gundestrup, personal communication).

The temperature profile measured in the borehole is shown in Fig. 2.28 (Johnsen et al., 1995). The temperature in the upper 1800 m does not deviate more than 0.5 °C from the present average surface temperature of -32 °C. Below 1800 m, the warming due to the geothermal heat flux causes a steady increase in temperature towards the bottom value of -9 °C. Johnsen et al. (1995) have modelled the temperature profile and used it to established conversion factors between past surface temperatures and $\delta^{18}O$ values measured in the ice core. Their results indicate that surface temperatures during the coldest part of the ice age (21.500 BP) were up to 25 °C colder than

Fig. 2.28 (below, left) - The temperature profile measured in the GRIP borehole. - From Johnsen et al. (1995).

Fig. 2.29 (right) - The age-depth profile in the GRIP core down to 2730 m depth and back to 100 000 years BP. - From data provided by S. J. Johnsen.

Fig. 2.30 (below, right) - Vertical strain in the GRIP core showing the ratio (in percent) of the present thickness of an annual layer to its original thickness at the surface. - After Dahl-Jensen et al. (1993), data provided by S.J. Johnsen.

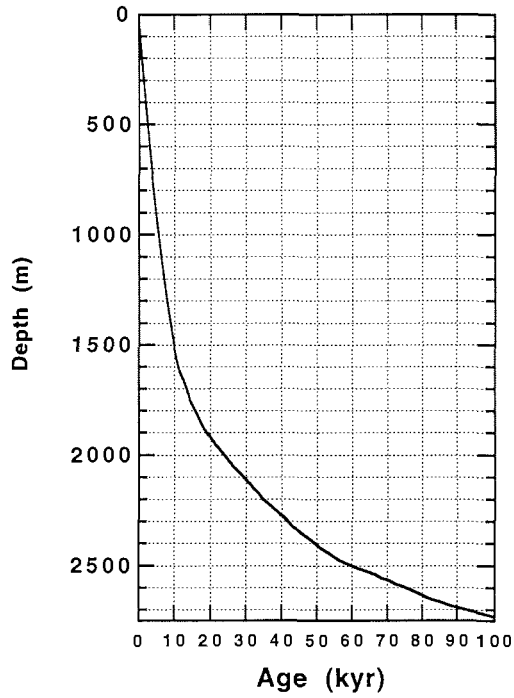

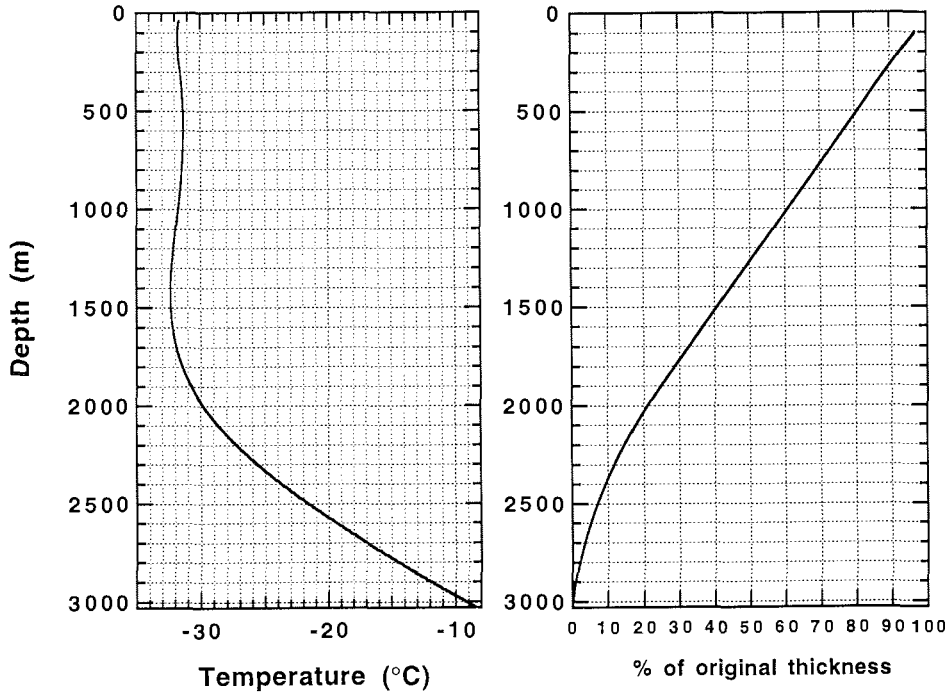

present day values. A similar result has been obtained by GISP2 researchers (Cuffey et al., 1995).

Timescale

The methods used for dating ice cores have been briefly described in Chapter 1. The GRIP timescale has been established by the combined use of stratigraphic layer counting and modelling of the process of layer thinning with depth (Dansgaard et al., 1993).

The simplest type of such a flow model is the so-called sandwich model (Nye, 1963 - see Paterson, 1994, p. 276), which assumes that each annual layer in the entire ice column thins at a constant vertical strain rate. In its simplest form, the model also assumes a constant accumulation rate (c) and a constant ice thickness. The vertical velocity w varies from -c at the surface to 0 at the bottom according to $w = -cz/H$, where z is the height above bedrock (z-axis upwards) and H is the ice thickness. The age t of ice at z is calculated from

$$t(z) = \int_H^z \frac{dz}{w} = -\frac{H}{c}\int_H^z \frac{dz}{z} = -\frac{H}{c}\ln\left(\frac{z}{H}\right) \qquad (2.27)$$

which gives reasonably accurate results in the upper half of the ice sheet, back to ≈10 kyr BP. The assumptions mentioned above are completely unrealistic for the deeper, older ice.

Dansgaard & Johnsen (1969) developed a more realistic model which assumes the vertical strain rate is constant down to a depth h above the bottom and then linearly decreases to zero approaching the bed. This leads to separate expressions for t(z) above and below z = h; the value of h can be determined by tuning the model to fit certain well dated reference horizons. To establish the GRIP timescale, Dansgaard et al. (1993a) used a modified Dansgaard-Johnsen model that introduces a soft sliding layer just above the bed, and assumes a variable accumulation rate (λ) determined from a relationship between measured $\delta^{18}O$ and λ values.

The age-depth profile determined by this model is shown in Fig. 2.29. The original timescale reaching back to 250 kyr BP has not been confirmed by results from the GISP2 core, and thus only the age-depth variation back to 100 kyr BP is shown.
Dahl-Jensen et al. (1993) have also used this flow model to determine the total thinning the annual layers in the GRIP core have experienced since they were deposited at the surface. The results, which indicate vertical strain vs. depth in the ice sheet, are shown in Fig. 2.30.

Numerical models of the ice flow and timescales at an ice divide have also been developed (Raymond, 1983; Dahl-Jensen, 1989; Schøtt et al., 1992). According to these models, the temperature, velocity and stress distributions in the ice are different at the ice divide than at a distance of a few ice depths away from it. The absence of horizontal shearing leads to a special variation of vertical strain rate with depth and an age-depth profile that differs in form from that on the flanks. Dahl-Jensen (1989) found that the isochrones would rise under the ice divide (in the lower part of the ice sheet) to form the so-called isochrone bump. The timescale would thus reach significantly further back in time in the narrow region of the divide, than a few ice thicknesses away. The bump would cause the annual layers to be inclined locally, reaching a maximum slope of 7° a few hundred meters above the bottom.
Hempel & Thyssen (1992) discussed an interesting feature in the internal radio echoes in Fig. 2.27. Bumps and lows in the bottom topography seem to be reflected quite closely in the shape of the echoes, with one exception: A bump is seen in the layering above the valley just west of the GRIP site. In addition, the top of the bump is seen to shift with decreasing depth towards the present ice divide position (Hempel & Thyssen, 1992; Fig. 3c). As mentioned by these authors, it is possible that this feature represents an isochrone bump, which, if true, would mean that the ice divide has been within 5 km of its present position for the last 75.000 years (at least).

However, the modelling results indicate that relatively minor shifts in the divide position could result in a complicated history of flow in the vertical direction, since the ice would alternately experience patterns of divide-flow and flank-flow (Raymond, 1983). Such a flow history would introduce uncertainties and even disturbances into an ice core record from the divide position.

3. MEASUREMENTS

3.1 SAMPLE PREPARATION

Sampling from the GRIP core

In the GRIP camp, the ice cores were stored in a snow cave at -25 °C after recovery, and then taken to a specially designed science trench for logging, sampling and measurements. Most of the samples for crystal studies were cut from the core in the trench. Temperatures in the science trench never exceeded -15 °C, which ensures that recrystallization should not have taken place and original textures and fabrics should be preserved in the samples (Gow, 1994). A bandsaw was used to cut 1 cm thick horizontal and vertical sections from the core (Fig. 3.1) and from these, thin sections were prepared using standard methods (Langway, 1958).

All sampling done in the field was carried out by Josef Kipfstuhl. This work was initiated during the 1990 field season and thus the firn part of the core (uppermost 90 m, drilled in 1989) is not covered in this study. Drilling reached a depth of 770 m in 1990 and thick sections were obtained at irregular intervals (10-115 m) during this season.

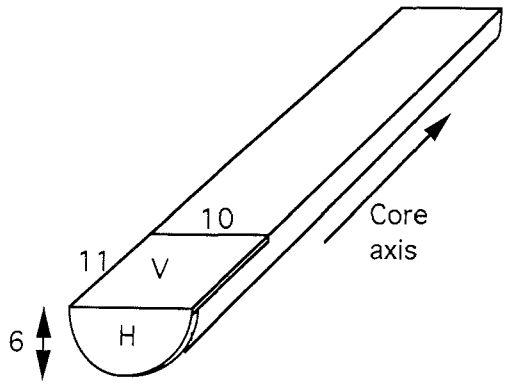

Fig. 3.1 - Thick section cutting from an ice core. The core is first cut with a bandsaw along the core axis, leaving a flat surface. The vertical thick section (V) cut parallel to this surface has dimensions 10x11 cm; the horizontal thick section 10x6 cm. - The upper part of the core, not shown here, is used for isotope, gases and chemistry measurements. The lower part is stored, and used for further sampling.

In 1991, drilling proceeded to a depth of 2320 m and samples were cut at 25-55 m intervals over most of the core length. The zone between 700 and 1300 m consisted of brittle ice* and the cores recovered, cracked into pieces due to internal stresses after being brought to the surface. Consequently, most samples from this interval were irregularly shaped, but this does not affect the measurements presented here in any way.
In 1992, drilling was terminated at 3028.65 m, having penetrated through 6 m of debris laden ice (silty ice) just above the bedrock. Thick sections were cut at 27.5 m intervals while the core was at Summit. Additional samples were taken from other depths of special interest after the core had been stored in Copenhagen.

Thin section preparation

The thin sections were prepared in the following way:

1. The thick section was placed on a 5 mm thick glass plate (size: 12x12 cm) and drops of water were put along its side, causing it to freeze onto the plate.
2. The plate was fixed on a microtome with the aid of vacuum plate attachment, connected to a vacuum pump. The microtome knife was then used to produce a smooth and plane parallel surface.
3. Another glass plate was frozen onto the smooth surface.
4. The section was then cut with a bandsaw, 1-2 mm from the smooth surface.
5. The thin section thus produced was reduced to 0.5 mm thickness with the microtome knife.

Occasionally the thin section would start cracking when it was being reduced in thickness. To prevent further damage, such thin sections were kept uncovered in the cold room, and allowed to sublimate down to the desired thickness. At -20 °C, sublimation normally reduced the thickness by 0.2-0.3 mm/day.

After preparation and measurement, the thin sections were stored in air tight plastic bags, kept at -20 °C in a closed drawer.

* The so-called brittle ice zone is the depth interval in an ice sheet in which the air bubbles disappear due to increasing overburden pressure. The air in the bubbles is transformed into clathrate hydrates, in which the atmospheric air molecules are trapped in the ice crystal lattice (Miller, 1969). For information on clathrate studies on GRIP samples see Pauer et al. (1995).

3.2 CRYSTAL SIZE MEASUREMENTS

When a thin section of ice is placed between crossed polarizers, individual crystals and crystal boundaries become clearly visible. This is due to differences in interference colours, which result from different c-axis orientations (Section 3.3). Crystal size measurements are normally made on photographs of the thin sections, but can also be conducted directly on the sections themselves. The latter option is preferable, since grain boundaries are occasionally invisible at certain polarization angles. When the thin section is placed on the measuring stage, the operator can still incline or turn the section to other angles and reveal the boundaries. This approach should increase the accuracy of the measurement and has been used throughout this work.

Crystal size (grain size) is expressed either as average area ($\bar{A}$) or average diameter ($\bar{d}$); different methods have been employed to obtain these values (e.g. Gow, 1969; Jacka, 1984a). Assuming a thin section of width L and area A (Fig. 3.2), the three most common approaches are as follows:

1. The number of grains M in the section is counted, yielding an average area per grain of A/M; the result can be converted into an average diameter, if desired. Circular cross sections of the grains are then normally assumed, and the average diameter found from $\bar{d} = \sqrt{4A/\pi M}$.

2. The number of grains N in a traverse of length L across the thin section is counted, yielding an average diameter L/N. This is referred to as the linear intercept method.

3. The maximum intercept length of each of N grains is measured, and the average value calculated.

Each of these methods has the drawback that a two-dimensional section can only give limited information about a three-dimensional grain structure. A thin section will usually not intersect each crystal at its maximum diameter (the "sectioning effect") and consequently the measured crystal sizes will be lower than the "true" values. Furthermore, the line along which the crystals are counted when the linear intercept method is employed will usually not cross the crystals at their maximum diameter seen in the thin section (Fig. 3.2). The underestimate can be partly overcome by multiplying the measured values by an appropriate correction factor. For example, a section cut through closely packed spherical grains of equal size will yield an average grain area which is 2/3 of the true maximum cross-sectional area (Alley, 1987). A correction factor of 3/2 must thus be applied to obtain the true area, and a factor of $(3/2)^{1/2} \approx 1.23$ to obtain the correct diameter. Gow (1969) suggested that measuring

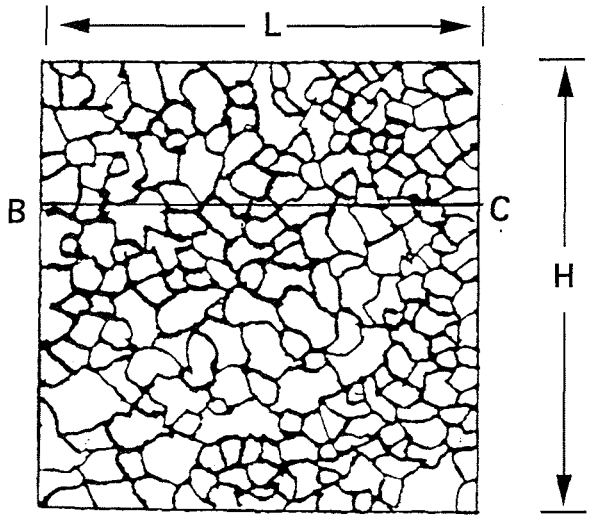

Fig. 3.2 - Schematic diagram of a thin section of dimensions LxH and area A = LH. Counting the total number of crystals M in the section yields the average area A/M. Counting N crystals along the transect BC yields the average grain size L/N.
Note that the transect does not cross each crystal at its greatest diameter seen in the section. Similarly, the thin section does not intersect each crystal at its maximum three-dimensional diameter.

TABLE 3.1 - CORRECTION FACTORS FOR LINEAR INTERCEPT MEASUREMENTS

Depth	221 m (V)	634 m (H)	1238 m (V)	2807 m (V)
d_H	2.6	4.2	4.0	
d_V	2.6		3.1	2.9
d_{Hmax}	3.0	4.9	4.4	
d_{Vmax}	3.0		3.2	3.2
Difference	15 %	17 %	10%(H)/ 3%(V)	10%

only the 50 largest crystals in each section would give a more realistic value than a measurement including all crystals. Jacka (1984a) presented data indicating that the three methods yielded crystal diameter values in the proportions 1.3 : 1.0 : 1.6. He multiplied by 1.75 the crystal sizes obtained by the linear intercept method, to obtain values closer to actual ones, but he did not explicitly state on which grounds this value was chosen. It appears to be common in the literature to present the measured, uncorrected linear intercept crystal sizes (e.g. Herron et al., 1985; Fisher & Koerner, 1986; Langway et al., 1988).

All crystal sizes presented in this work, except those from samples used for deformation tests (Chapter 6), are obtained with the linear intercept method. Measurements have predominantly been carried out on vertical thin sections, since these allow the determination of both horizontal and vertical grain diameters. Each value is typically an average of five traverses across the thin section. No correction factor is applied to the measured values, to facilitate intercomparison with other works, including articles published by this author (see Tison et al., 1994; Thorsteinsson et al., 1995; Thorsteinsson et al., 1996). Furthermore, grain shapes vary along the core, and the same correction factor cannot be assumed to apply at all depths. Information on the magnitude of the correction factor at different depths has, however, been obtained as follows.

On four thin sections, three vertical (V) and one horizontal (H), linear-intercept diameters were measured along transects to yield average horizontal ($\bar{d}_H$) and vertical ($\bar{d}_V$) diameters. Then, maximum horizontal and maximum vertical diameters of each grain crossed by these same transects were measured and the results averaged to yield $\bar{d}_{Hmax}$ and $\bar{d}_{Vmax}$. Some 200 crystals were measured in each case. The results are shown in Table 3.1. The counting along a transect underestimates the grain diameter observed in the thin section by 10-17% (except for the vertical diameters at 1238 m depth, where the difference is only 3% - probably due to the flattened shape of the grains by this depth). Assuming that the sectioning effect introduces an error of a similar magnitude, the correction factor can be estimated to be in the range $(1.1)^2$ to $(1.17)^2$, i.e. between 1.2 and 1.4. The factor of 1.23, used by Alley & Woods (in review), in their study of grain sizes in the GISP2 core, falls within this range.

It is worth noting that accurate determination of "true" crystal size is not of critical importance. What matters is the relative variation in crystal size between different recrystallization regimes, climatic periods and stress-strain conditions.

3.3 C-AXIS MEASUREMENTS

Optical properties of ice

In isotropic materials, such as gases, most fluids and amorphous solids like glass, the velocity of light is the same in all directions. Cubic crystals are optically isotropic, but crystals having other geometries, including ice Ih crystals, are optically anisotropic (Hobbs, 1974). Such materials exhibit a property called double refraction (or birefringence), meaning that a light ray entering a crystal is broken up into two waves, one ordinary (O) and one extraordinary (E), which travel through the crystal in slightly different directions (Fig. 3.3) at slightly different velocities. In addition, they are plane-polarized in mutually perpendicular planes: the electric vector of the ordinary wave vibrates perpendicular to the optic axis; the electric vector of the extraordinary wave vibrates in a plane defined by the propagation direction and the optic axis.

The refractive indices of the two waves are $n_O = c/v_O$ and $n_E = c/v_E$, where c is the velocity of light in air ($\approx$ c in vacuum), v_O is the velocity of the ordinary wave and v_E is the velocity of the extraordinary wave in a direction normal to the wave front when the wave is travelling perpendicular to the optic axis (Hobbs, 1974). Since $v_O > v_E$, ice is said to be optically positive. The quantity $n_E - n_O$, which equals 0.0014 for the sodium D-lines, is the birefringence.

Like other hexagonal crystals, ice crystals exhibit isotropic behaviour along their optic axis, which coincides with the c-axis. No extraordinary wave is produced as a polarized light ray is transmitted along this direction and it thus enters and leaves the crystal with its type and direction of polarization unchanged. As there is only a single optic axis, such crystals are called optically uniaxial (Ehlers, 1987).

The Universal Stage

The optical properties outlined above can be used to determine the c-axis (optic axis) orientation of ice crystals in a thin section. The Universal Stage (Rigsby Stage) (Fig. 3.4) is an instrument built for this purpose, originally introduced by Fedorow for use on a polarizing petrographic microscope, and later modified for ice fabric work (Rigsby, 1951). The thin section being studied is placed on the stage between crossed polarizers and can be rotated about horizontal and vertical axes.

The optical principles are explained in Fig. 3.5. Non-polarized white light enters the first polarizing plate, called the polarizer, and continues plane-

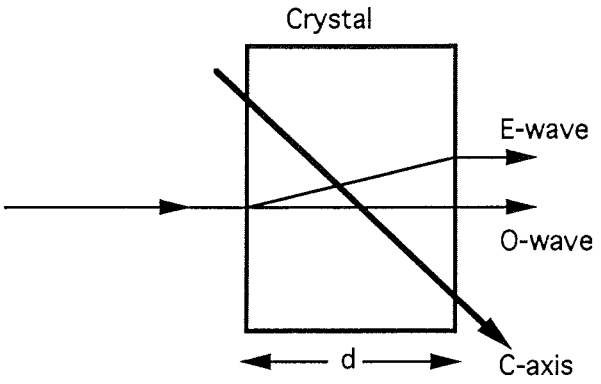

Fig. 3.3 - Linearly polarized light enters a crystal of thickness d and is split into an ordinary and extraordinary wave, which travel with different velocities through the crystal.

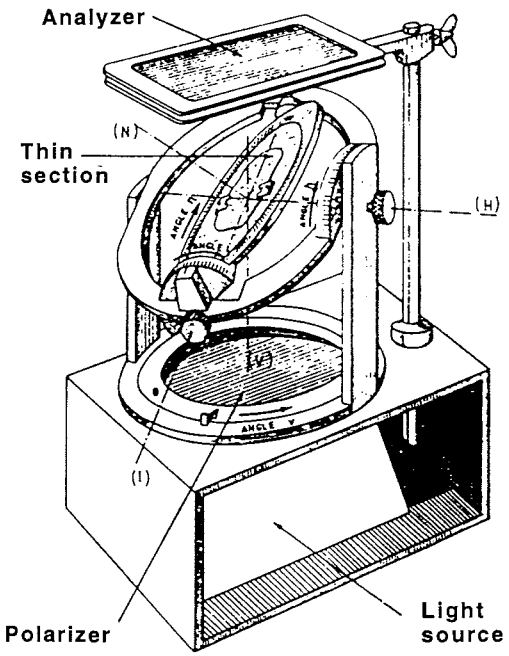

Fig. 3.4 - The Universal Stage. The thin section is placed on a glass plate between crossed polaroids. The light source is in the box. The thin section can be rotated about two horizontal axes (H and I) and about one axis which is perpendicular to the section (N). In addition, the whole stage can be rotated about the fixed vertical axis V.

polarized, with the electric vector constrained to vibrate in a single plane perpendicular to the direction of travel. Restricting the discussion to a single wavelength λ in the white light from the source, three different cases must now be considered.

1. The c-axis is perpendicular to the direction of light propagation, i.e. horizontal in the thin section (this is the case shown in Fig. 3.5 c-d). The polarized light splits into the O- and E-waves, vibrating at right angles and propagating at different velocities v_O and v_E, and thus with different wavelengths λ_O and λ_E. In a thin section of thickness d, there are d/λ_O wavelengths of the ordinary wave and d/λ_E wavelengths of the extraordinary wave. When they emerge from the crystal, both waves again acquire the original wavelength λ, but the O-wave is now

$$\frac{d}{\lambda_E} - \frac{d}{\lambda_O} = \frac{d}{\lambda}(n_E - n_O) \qquad (3.1)$$

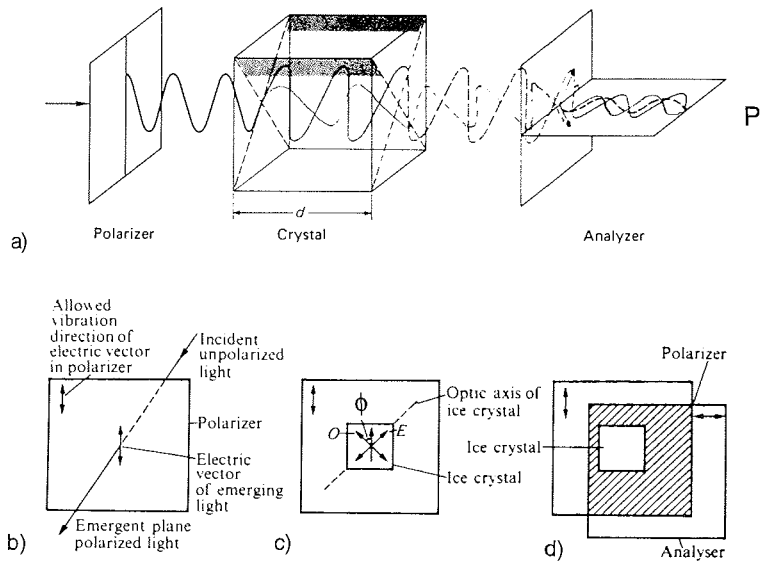

Fig. 3.5 - Optics of the Universal Stage. **a)** General overview: Plane-polarized light splits into O- and E-waves in the crystal, attains a path difference and is brought to interference after passing through the analyzer. The thickness of the crystal (d) is greatly exaggerated for clarity. In b) - d) the situation is viewed from the point P. **b)** Production of the plane-polarized light. **c)** The small rectangle is the crystal and its c-axis (optic axis) is perpendicular to the direction of the incoming light. The vibration directions of the O- and E-waves are shown. **d)** Between crossed polaroids, only the crystal will appear bright, since light emerging from it will have a horizontal component which will be transmitted through the analyser. However, the crystal will appear dark when it assumes special orientations (see text). - a) from Wenk (1985); b) - d) from Hobbs (1974).

wavelengths ahead of the E-wave. (Here, use has been made of the relation $n_E = c/v_E = \lambda/\lambda_E$, and similarly for n_O). The two waves attain a path difference defined as

$$\Delta = d(n_E - n_O) \qquad (3.2)$$

and a phase difference

$$\delta = \frac{2\pi d}{\lambda}(n_E - n_O) \qquad (3.3)$$

and travel towards the second polarizing plate, called the analyzer. The analyzer passes only those components of the waves that vibrate at right angles to the original polarized light. The amplitude of the component waves emerging from the analyzer (and thus the intensity of the light seen by the observer; i.e. the brightness of the crystal) is dependent upon the angle ϕ indicated in Fig. 3.5 c. When $\phi = 0°$, there is no E-wave (since the electric vector of the incoming ray has no horizontal component) and when $\phi = 90°$ there is no O-wave; in both cases the light will emerge from the crystal without a horizontal component and thus cannot pass through the analyzer. The crystal will therefore appear dark between the crossed polaroids. Clearly, this will also occur for $\phi = 180°$ and $\phi = 270°$ and every crystal in the thin section (except those with vertical c-axes) thus goes through four extinction positions as the section is rotated 360°. For $\phi = 45° + n\pi/2$; n=0,1,2,3, the crystal will exhibit maximum brightness and is said to be in diagonal position.

2. If the c-axis is not perpendicular to the light ray, the velocity of the extraordinary wave will depend on the angle between the c-axis and the direction of the ray. The description above still applies and the crystal will also appear dark at four extinction positions.

3. If the c-axis is parallel to the direction of light propagation, i.e. vertical in the thin section, there will be no extraordinary wave and the crystal will thus appear dark at all positions, when the thin section is rotated 360°.

In cases 1 and 2, the wave components which have passed through the analyzer interfere to produce an interference colour, which depends on the path difference Δ (Müller & Raith, 1987), i.e. the thickness of the crystal. For a particular wavelength λ, the two component waves emerging from the analyzer will cancel when the path difference equals a whole multiple of λ (meaning that they will be out of phase by $n2\pi$; n=1,2,3...). This wavelength will thus be subtracted from the original white light and the crystal will exhibit a colour which results from a combination of the remaining wavelengths.

For example, a thin section of thickness 0.4 mm will result in a path difference of $\Delta = (0.4*10^6 \text{ nm})*0.0014 = 560$ nm, which corresponds to the wavelength of green light. This wavelength will be eliminated in a crystal with a horizontal

c-axis, lying in the diagonal position, and the crystal will exhibit the complementary color of first order red. With increasing thin section thickness, a spectrum of interference colours is observed (typically red-violet-blue-green-yellow-orange, all first order), which then repeats itself to produce second and third order colours if the thickness is increased still further. Note, that tilting of the thin section also will change the path difference, and thus the colours.

C-axis measurements

The measurement of the c-axis orientation of a crystal consists in bringing the c-axis into extinction position, either vertical or horizontal, by turning the thin section about the axes of the Universal Stage. Detailed descriptions of the procedures are provided by Langway (1958) and by Eicken (1985). In brief, the procedure is as follows (Fig. 3.6).

1. The crystal is first rotated into extinction with its c-axis in a vertical plane, which is perpendicular to the vibration plane of the incoming polarized light (ϕ = 0° in Fig. 3.5.c). By rotating on both horizontal axes of the stage according to a certain procedure, the c-axis is brought into vertical position, in which it will remain dark when the whole stage is rotated. When the c-axis is brought to a vertical position, it is said to be in polar orientation. The angle the c-axis makes with the vertical before these manipulations is read from one of the graduated scales on the stage and the azimuth position is also noted.

2. If the c-axis is inclined more than 45° from the vertical, it must be laid down into horizontal position, called equatorial orientation, using a procedure different from that in 1.

The readings on the stage must be corrected for the refraction which occurs when the light passes from crystal to air (Fig. 3.7). The refraction index of ice is n = 1.31, found from Snell's law:

$$n = \frac{\sin\alpha}{\sin\beta} \qquad (3.4)$$

where α is the angle of incidence, and β is the angle of refraction. For example, an inclination of the stage to 68° (the measured value) is required to bring into extinction a c-axis which in reality is inclined 45° from the vertical.

Rigsby (1951) noticed that for a c-axis orientation of 45°, measurements of the crystal with both the polar and the equatorial method, corrected for refraction by Snell's law, would not yield the same result. A disagreement of about 10° was found, indicating that the correction applied to one or both of the measurements was too large. Kamb (1962) analysed the optics involved theoretically and found that the correction based on Snell's law was valid to a good approximation when the polar method was used, but failed when the

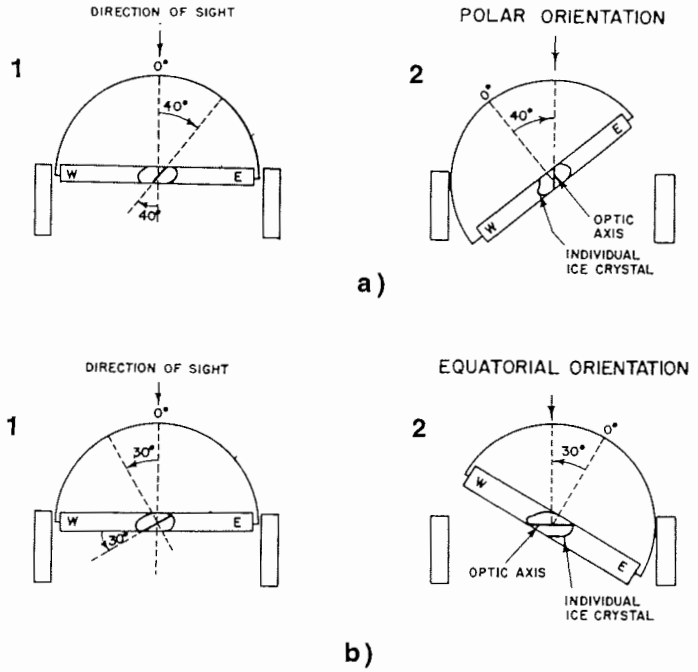

Fig. 3.6 - The inclination of a c-axis is determined by bringing it either to a vertical or to a horizontal position. **a)** A c-axis which is inclined 40° to the vertical when the stage is in horizontal position is brought into polar orientation by tilting the stage about one of the horizontal axes. **b)** A c-axis which is inclined 60° to the vertical (30° to the horizontal) is brought into equatorial position. - After Langway (1958), modified.

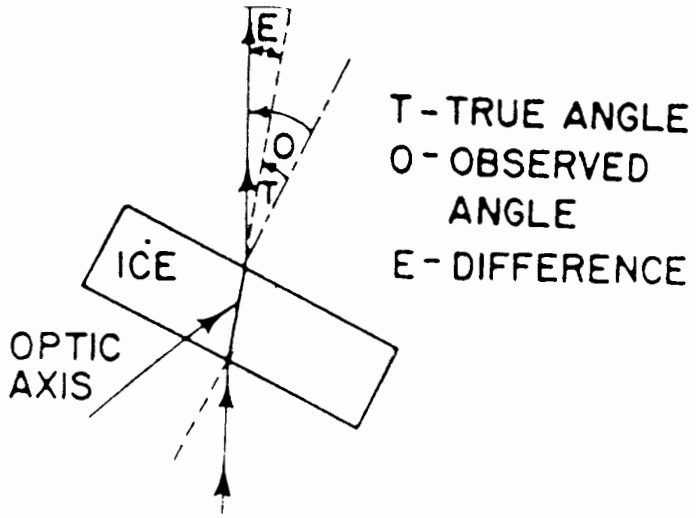

Fig. 3.7 - When the c-axis inclination is measured by bringing it to the vertical position, the observed angle is always greater than the true angle, due to refraction. From Langway (1958).

crystal was being laid down horizontally by use of the equatorial method. In the latter case, a simple linear formula was derived for correcting the inclination readings. Kamb (1962) thus recommended the following refraction corrections to obtain the true inclination i from the measured inclination i_m:

Polar method: $i = \sin^{-1}(\frac{1}{1.31} \sin i_m)$ (Snell's law) (3.4)

Equatorial method: $i = 1.04 i_m$ (3.5)

These standard corrections have been applied to the c-axis measurements presented in this work. Note that these formulas imply that the measured angle is always greater than the true angle in polar orientation (Fig. 3.7) but smaller than the true angle in equatorial orientation.

The Universal Stage used at the Alfred Wegener Institute has been fitted with two opto-electronic sensors for automatic recording of the azimuth and tilt angle (Lange, 1988). Gray-coded signals of the angles are produced and transmitted to an interface box by pushing buttons on a triggering device; one for equatorial and the other for polar positions of the c-axes. The interface converts the signals into ASCII data and transmits them via a RS 232 interface to a PC computer, which stores the data. This system considerably reduces the time needed for measurement of a thin section, since the operator does not have to read the azimuth and tilt angle values and write them down.

There are four main errors in measuring the c-axis orientations (see Langway, 1958).

First, the error involved in determining the exact extinction position can be estimated to be usually within 2°, but perhaps up to 5° at high angles.
Second, an error in the tilt angle determination is introduced if the operator does not keep his eye directly above the crystal being measured.
Third, an error can result in reading the azimuth and tilt angle from the graduated scales on the stage. This error is almost completely eliminated by the use of the semiautomatic stage described above. The resolution of the opto-electronic sensors is 1° and repeated measurements of a single crystal normally agree within 1-2°.
4. There can be mechanical error in the universal stage itself.

Langway (1958) concludes that the total error in each c-axis measurement should normally not exceed 5°. Since each fabric diagram is the sum of up to 200 measurements, a small error in the position of each axis is not critical for the statistical evaluation and final interpretation of the diagram.

The 200 crystals required to obtain a statistically reliable result should be as uniformly distributed over the whole area of the thin section as possible, to avoid any observer bias. This can be achieved by placing a centimeter grid on top of the thin section and measuring a fixed number of crystals within each quadrant. For example, if the total area of the thin section is 50 cm^2, four crystals are measured within each cm^2.

Fabric diagrams

If one visualizes a sphere centered on the crystal being measured, and a line through the c-axis, the line will intersect the sphere at two opposite points. The distribution of the measured points on the lower hemisphere, projected into a horizontal plane, is the fabric diagram for the sample. In ice fabric studies the Schmidt equal-area net is employed for plotting c-axis data. It is constructed with the Lambert-projection, in such a way that each element of unit area on the projected net corresponds to a unit area on the sphere.

Fig. 3.8 illustrates the projection. The point M on the hemisphere is represented by the point m in the projected horizontal plane such that Om = SM = r. Now we have

$$\sin\frac{\theta}{2} = \frac{r}{2R} \quad \Rightarrow \quad r = 2R\sin\frac{\theta}{2} \tag{3.6}$$

$$\Rightarrow \quad \frac{dr}{d\theta} = R\cos\frac{\theta}{2} \quad \Rightarrow \quad dr = R\cos\frac{\theta}{2}\,d\theta$$

and hence

$$rdr = 2R^2\sin\frac{\theta}{2}\cos\frac{\theta}{2}\,d\theta \quad \Rightarrow \quad rdr = R^2\sin\theta\,d\theta \tag{3.7}.$$

An element of area on the projected net is

$$dS = (rd\phi)dr = rdrd\phi \tag{3.8}$$

whereas an element of area on the sphere is

$$dS = R^2\sin\theta\,d\theta\,d\phi \tag{3.9}$$

and these two elements are equal according to (3.7).

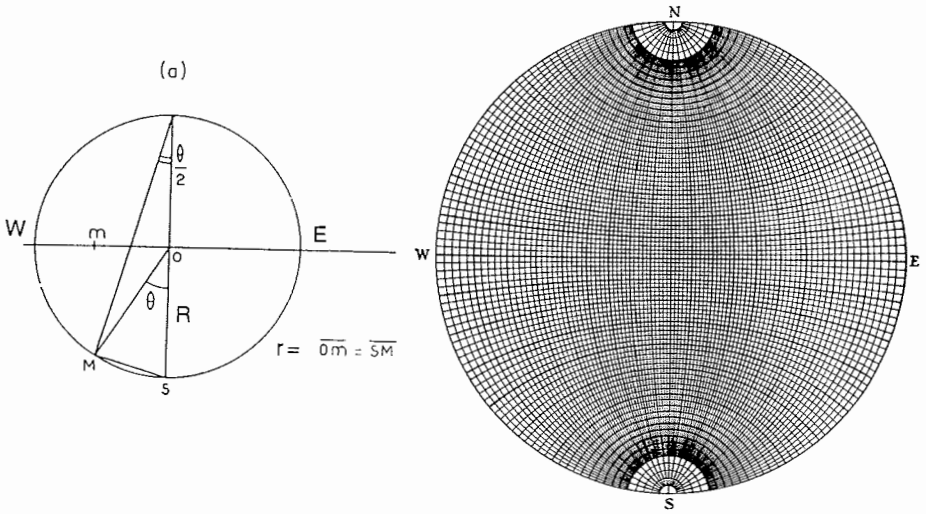

Fig. 3.8 - The equal area projection. **a)** The sphere viewed from the side. A line through a c-axis inclined θ from the vertical intersects the spherical surface in the point M. M is projected to the point m in the horizontal plane, such that Om = SM = r. The radius of the sphere is R.
b) The 2-D Schmidt net represents the spherical surface.

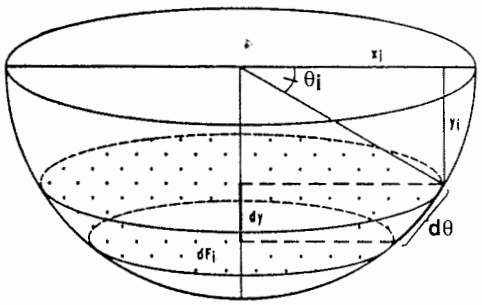

Fig. 3.9 - Deriving the Degree of orientation (R) assuming uniform distribution of c-axes on the hemiphere.

Special techniques are available for plotting the refraction corrected c-axis data on the Schmidt net by hand, but these have now been replaced by computer programs. The program Ariane, developed by J.F. Adam (1989) has been used in this work. It enables the presentation of the c-axis data either as point diagrams or as different kinds of contoured and shaded orientation density diagrams. A contoured diagram is constructed by counting the number of points that fall within each 1% of the total area of the diagram and drawing contour lines through elements of equal point density. In early work on ice fabrics (e.g. Rigsby, 1951; Kamb, 1972; Gow & Williamson, 1976), it was customary to present contoured diagrams. Later it was pointed out in a review paper that the percentage of c-axes falling in 1% of the area of an equal area net is not a statistically significant parameter, and thus the presentation of point diagrams and the use of other methods to determine fabric strength was recommended (Hooke et al.,1980). In this work, only point diagrams are presented and the statistical parameters described in the following section are used to evaluate fabric concentration.

Fabric statistics

In recent years, two parameters have commonly been used as measures of fabric strength (Kohnen & Gow, 1979; Herron et al., 1985; Paterson, 1994). One is α, the half-apex angle of a cone which contains 90% of the measured c-axes. α decreases with increased fabric strength, but has the disadvantage that it is insensitive to the distribution of c-axes within the cone. The other parameter is R/N, the normalized length of the resultant vector. It is obtained by treating the c-axes as unit vectors, calculating the length of their vector sum R (= S below) and dividing by the number of axes N to obtain the normalized length. This parameter varies between 0.5 for random and 1 for completely parallel orientations.

The Ariane program calculates several statistical parameters, including two which closely resemble α and R/N, and an eigenvalue statistic describing fabric shape. The program treats each c-axis as a unit vector with spherical coordinates (r, ϕ, θ), where $r = 1$ and ϕ is the azimuth and θ the tilt angle measured on the U-stage. Conversion to cartesian coordinates (x, y, z) is required to calculate some parameters. The four parameters used in this work are as follows.

1. Degree of orientation - R (German: Regelungsgrad): To derive this parameter (Wallbrecher, 1978), assume each c-axis is represented by a unit vector within the unit hemisphere in Fig. 3.9. If the c-axes are uniformly distributed within the hemisphere, the number of end points per unit area is

$$\frac{n_i}{dF_i} = k \quad \text{(constant)} \qquad (3.10)$$

The length of the vector sum of the n_i axes is

$$S = \sum y_i n_i \qquad (3.11)$$

since the x-components cancel out. (3.10) and (3.11) combine to give

$$S = \sum y_i k\, dF_i = k\sum \sin\theta_i\, dF_i \qquad (3.12)$$

Since $k = n_i/dF_i = N/2\pi r^2 = N/2\pi$, where r=1 is the radius of the hemisphere and N is the number of axes, and $dF_i = 2\pi \cos\theta_i\, d\theta$, (3.12) gives

$$S = \frac{N}{2\pi}\sum \sin\theta_i\, 2\pi \cos\theta_i\, d\theta = \frac{N}{2}\sum \sin 2\theta\, d\theta \qquad (3.13)$$

Replacing the summation with integration over the hemisphere yields

$$S = \frac{N}{2}\int_0^{\pi/2} \sin 2\theta\, d\theta = \frac{N}{2}\frac{1 - \cos\pi}{2} = \frac{N}{2} \qquad (3.14)$$

for the vector sum of N uniformly distributed axes. If all c-axes are parallel, S = N and thus for any distribution

$$\frac{N}{2} \le S \le N$$

The degree of orientation in percent can now be defined as

$$R = \frac{(2S - N)}{N} * 100\% \qquad (3.15)$$

which varies between 0% for the uniform distribution and 100% for completely parallel orientations.

The derivation assumes that the c-axes are uniformly distributed within the fabric pattern being considered, a condition which is not strictly fulfilled in the natural fabrics. The results presented in later chapters nevertheless indicate that R is an excellent measure of fabric strength, and particularly well suited for describing the evolution from a random to a strong single maximum fabric.

R has thus been chosen as the main parameter for describing fabric strength in this work.

2. Spherical aperture - α_s. This parameter is defined by Wallbrecher (1979) as

$$\alpha_s = \arcsin\left(\sqrt{2\frac{1 - 1/N}{k}}\right) [°] \qquad (3.16)$$

where N is the number of axes and k = (N-1/N-S) is the so-called concentration parameter (Fisher, 1953), which is a measure of the scatter of the c-axes about the average axis. The spherical aperture can be described as the radius of a circle centered on the average c-axis in the fabric diagram, and containing within it an uniform distribution of c-axes which has the same R-value as the measured distribution. α_s can be visualized very much like the cone half-angle α, and it has the advantage that it takes the strength of the distribution within the cone into account, which α does not.

3. Eigenvalues - s_1, s_2, s_3. To analyse fabric shapes an eigenvalue calculation is performed for each fabric diagram. Each c-axis is converted into cartesian coordinates and the cross product matrix (or orientation tensor) determined by standard methods (Wallbrecher, 1986). The eigenvectors of this matrix represent three orthogonal unit vectors along the axes of an ellipsoid which best fits the distribution of c-axes; the eigenvalues are the lengths of these axes. By dividing each eigenvalue by N, the normalized eigenvalues (s_1,s_2,s_3) are obtained. They obey the conditions

$$s_1 \leq s_2 \leq s_3 \qquad \text{and} \qquad s_1 + s_2 + s_3 = 1 \qquad (3.17)$$

Direct comparison of the eigenvalues reveals information about fabric shapes. A random fabric will have $s_1 \approx s_2 \approx s_3 \approx 1/3$ and a symmetrical single maximum will have $0 \leq s_1 \approx s_2 \leq 1/6$ and $2/3 \leq s_3 \leq 1$. In addition, they can be used to distinguish between unimodal and girdle fabrics by computing the parameter

$$q = \frac{\ln(s_3/s_2)}{\ln(s_2/s_1)} \qquad (3.18)$$

(Woodcock, 1977; see also Adam,1989). The parameter q lies in the interval [0;1] for girdle fabrics and [1,∞[for unimodal fabrics.

4. RESULTS

In this chapter, the general trends in crystal size and orientation along the entire GRIP core will be presented and briefly described. More detailed results from interesting sections of the core will be presented in later chapters.

4.1 THE CRYSTAL SIZE PROFILE

The profile of horizontal crystal diameters along the entire core is presented in Fig. 4.1. Vertical crystal diameters at selected depths are also indicated. The results are obtained by linear intercept measurements on the thin sections shown in Fig. 4.2. The measurements start at a depth of 110 m, where the crystal size is 1.6 mm. A steady increase in crystal size is observed down to 700 m, where the horizontal diameter reaches a limiting value of about 4 mm and the vertical diameter attains a value of 3 mm. Crystal size is nearly constant through the remaining part of the Holocene ice, but decreases to 2.8 mm at 1650 m, 25 m below the transition into the Wisconsin ice (see Section 5.1 for more detailed data across this transition). The crystal size decreases through the upper part of the Wisconsin ice and reaches a minimum of 2.0 mm at 1980 m depth. Below this depth, grain size tends to increase slightly.

The Wisconsin-Eemian transition occurs at 2790 m, and three points within the Eemian are shown on this graph. The first point (2797 m) shows that an increase in crystal size occurs below the transition. A value of 4.3 mm is found in one of the cool stages in the Eemian sequence (2806 m), but a drastic increase to 14.0 mm occurs by 2860 m. A continuous record of vertical crystal size in the Eemian, indicating that it varies strongly with climatic parameters, will be presented in Section 5.1 (see also Thorsteinsson et al., 1995).

As the Saalean glacial is entered at 2865 m, crystal size returns to smaller values (4-5 mm), but then below 2900 m it steadily increases. It reaches a maximum value of 33.3 mm just above the transition into basal silty ice at 3022.5 m, where an abrupt decrease to 5 mm (not shown in Fig. 4.1) occurs. Crystal size variations in the silty ice have been discussed in detail by Tison et al. (1994) and a brief overview will be given in Section 5.1.

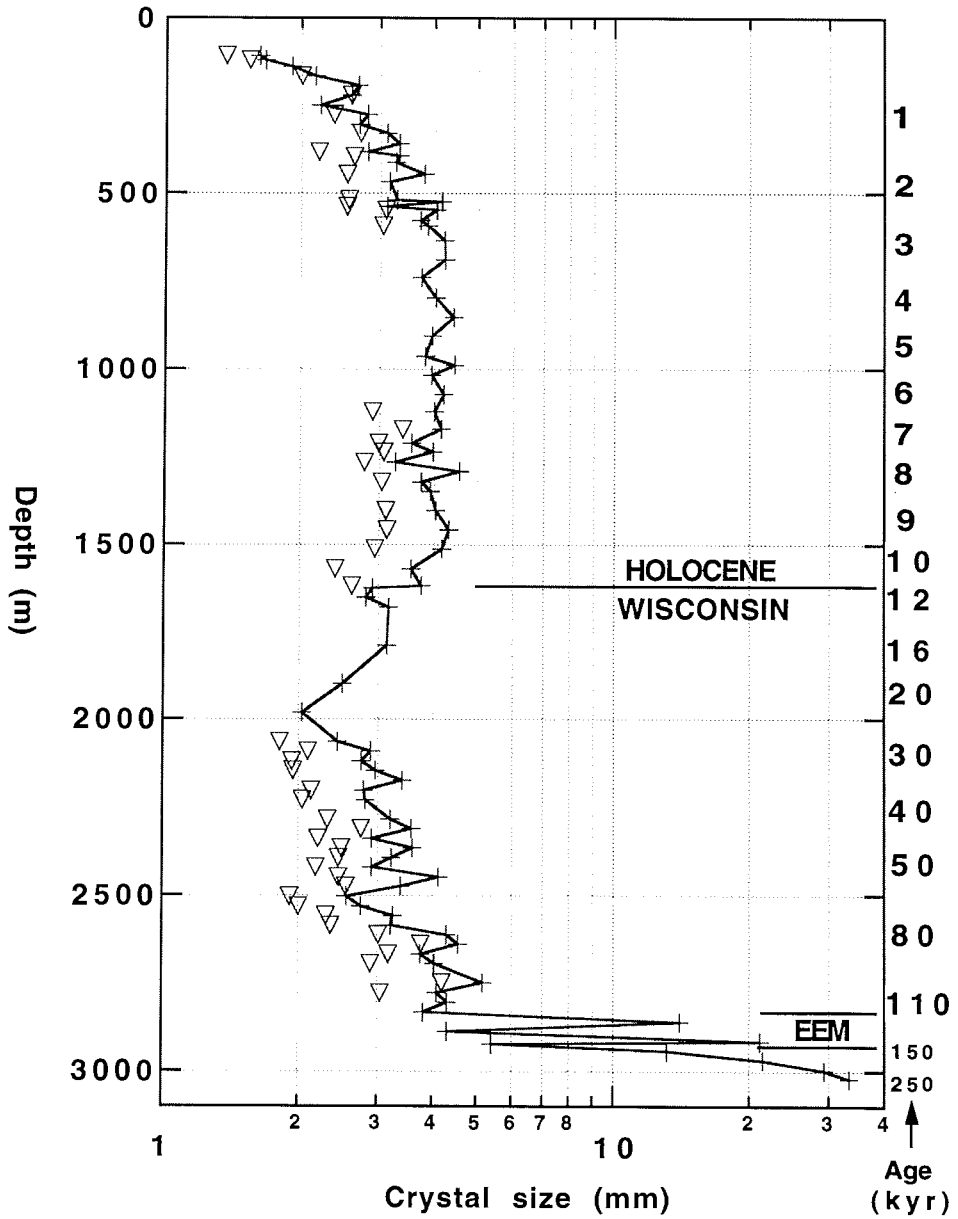

Fig. 4.1 - The crystal size profile for the whole GRIP core. All values are averages of crystal diameters, measured with the linear intercept method. Crosses denote horizontal diameters, triangles vertical ones. The GRIP timescale according to Dansgaard et al. (1993) is indicated to the right. Note that the crystal sizes are plotted on a logarithmic scale.

4.2 CRYSTAL ORIENTATION FABRICS

Fabric diagrams from 34 different depths, spanning the entire core, are presented in Fig. 4.2. The orientations determined on vertical sections have been rotated into the horizontal plane, using the Ariane program. Thus all the diagrams in Fig. 4.2 show the c-axis distributions as viewed from above, along the core axis. No information is available on the true horizontal orientation of the diagrams, since there was no azimuth control on the cores during drilling.

The degree of orientation (R), spherical aperture (α_S) and normalized eigenvalues (s_1,s_2,s_3) have been calculated for each diagram. The results are presented in Fig. 4.3 (excluding No. 28 and 30). The two uppermost diagrams in Fig. 4.2 show a random fabric with R < 20% and $\alpha_S > 60°$ (Fig. 4.3a). The s_3 eigenvalue is somewhat higher than the other two (Fig. 4.3b), indicating that the fabric has already started contracting. The fabric strength increases quite rapidly between 249 m and 470 m, where an increased concentration in the middle of the diagram is evident and fewer axes lie close to the horizontal. The strengthening is gradual in the remainder of the Holocene ice and by a depth of 1500 m R has attained the value 72%. The spherical aperture is 32° at this depth, and the s_3 eigenvalue has increased to 0.77, whereas s_1 and s_2 are 0.09 and 0.13, respectively. The central broad maximum becomes more concentrated between 500 and 1500 m, but the distribution of points within the maximum is usually slightly non-uniform.

No sharp fabric contrast is observed at the Holocene-Wisconsin boundary (see also Chapter 6). Instead, the steady trend towards a stronger fabric continues into the Wisconsin ice, with the central maximum still contracting and fewer and fewer axes lying outside it. The fabrics between 2174 m and 2779 m are all of the strong single maximum type. R is generally higher than 90%, reaching a maximum of 98% at 2587 m. α_S is between 10° and 20° and the s_3 eigenvalue has increased to above 0.9, whereas s_1 and s_2 are lower than 0.05.

Fabric diagram No. 29, from 2807 m depth in fine grained (4.3 mm) ice in the Eemian cold stage 5e2, still shows a strong single maximum. At 2862 m (warm stage 5e5 in the Early Eemian) a very different fabric is obtained. This fabric can best be described as a girdle, clustered around a plane which is tilted about 20° from the vertical. The ice is here very coarse grained, with an average horizontal grain size of 15 mm. The points are not uniformly distributed within the girdle, but appear to cluster into several separate maxima.

The first Saalean fabric diagram at 2889 m (No. 31; crystal size = 4.3 mm) shows a strong single maximum, with several crystals lying on opposite sides quite far outside the central maximum. The three lowest diagrams are measured in the increasingly coarse grained ice in the lowest 80 m of the

Fig. 4.2 - Fabric diagrams from c-axis orientation measurements on 32 thin sections in the GRIP core. A photo of the thin section is presented along with each diagram. Diagrams No. 1-27, 29 and 31 are obtained from measurements on horizontal thin sections; No. 28, 30 and 32-34 are from vertical ones. Photos No. 1-25 are from horizontal thin sections, No. 26-34 from vertical ones.

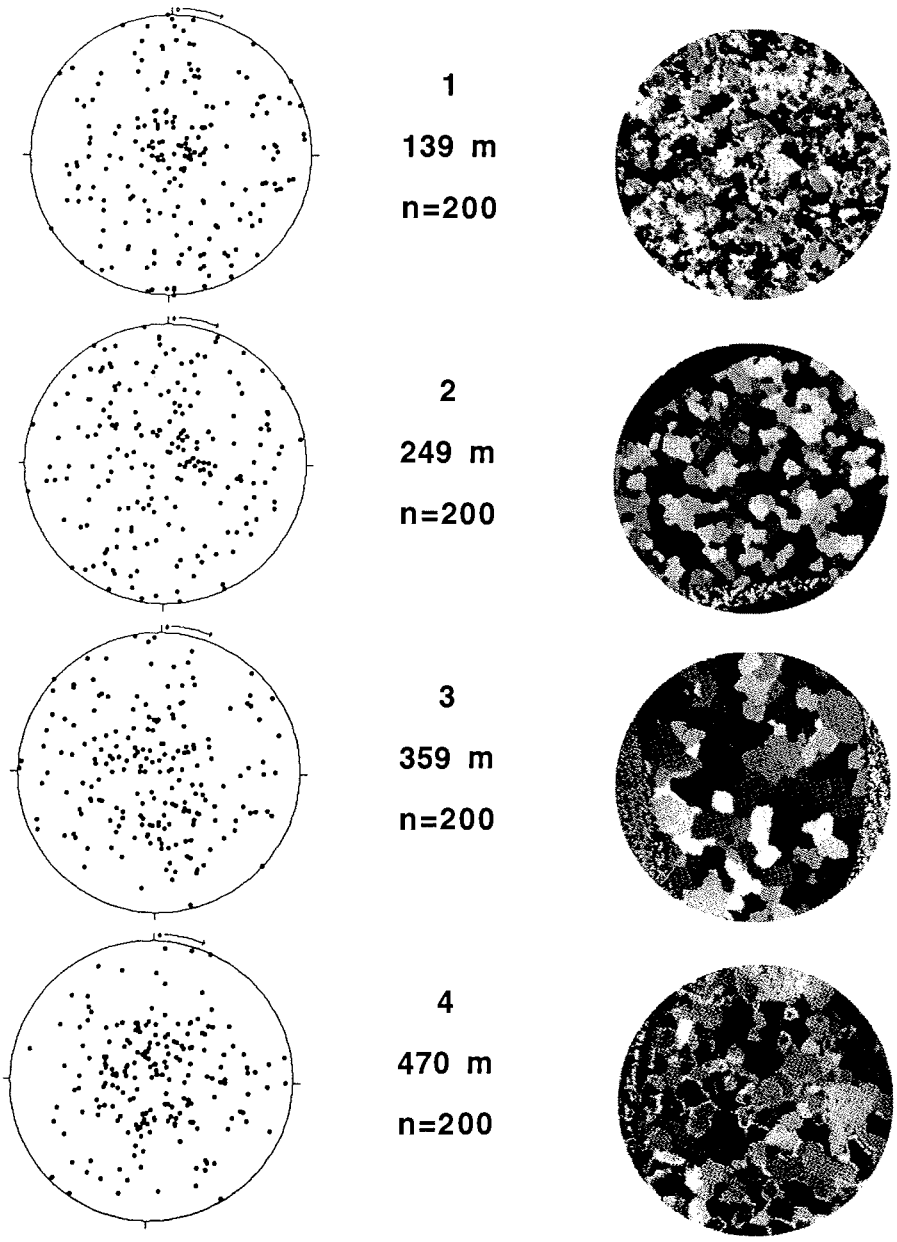

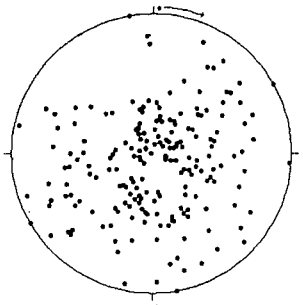

5

579 m

n=200

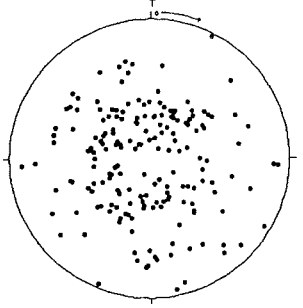

6

689 m

n=188

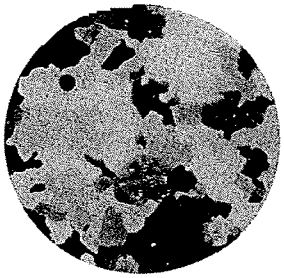

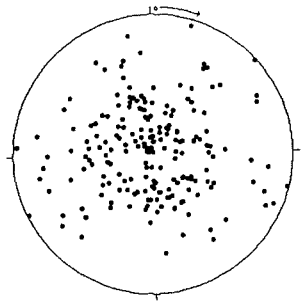

7

799 m

n=200

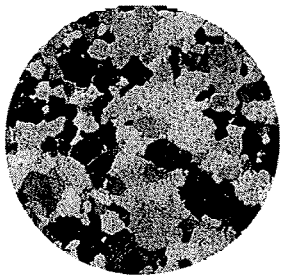

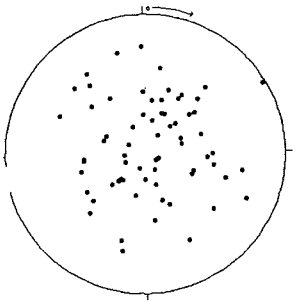

8

908 m

n=68

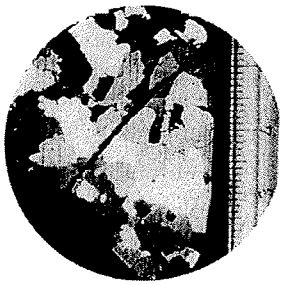

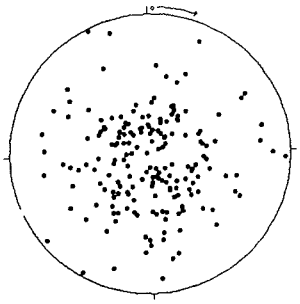

9

991 m

n=190

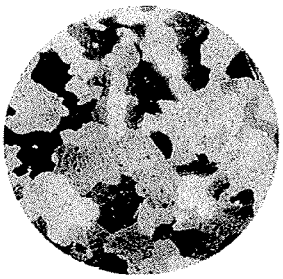

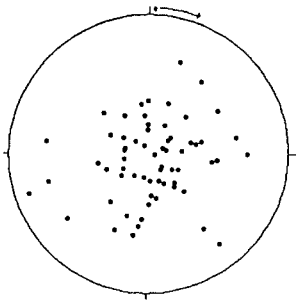

10

1074 m

n=64

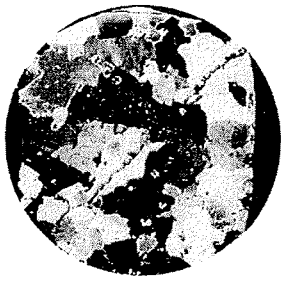

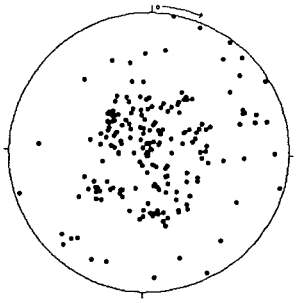

11

1173 m

n=201

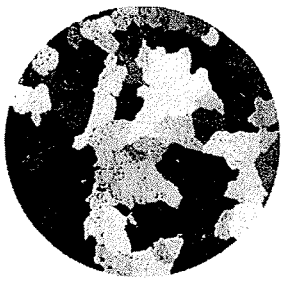

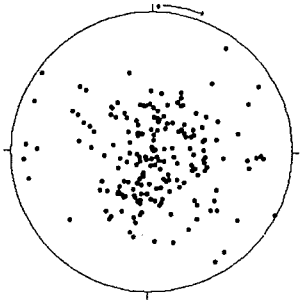

12

1293 m

n=194

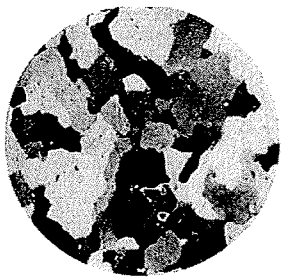

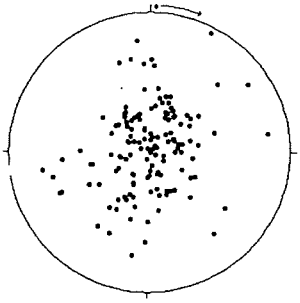

13

1404 m

n=143

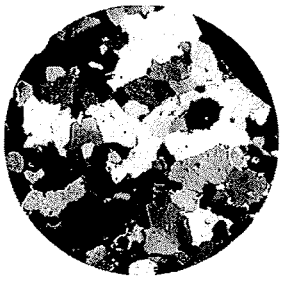

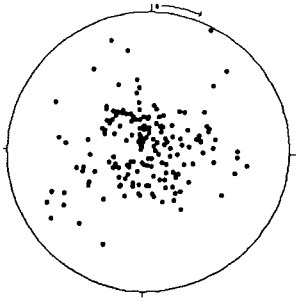

14

1514 m

n=174

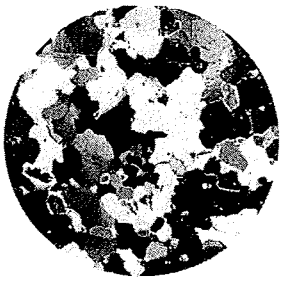

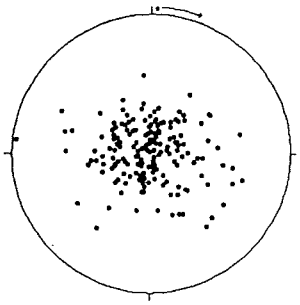

15
1569 m
n=171

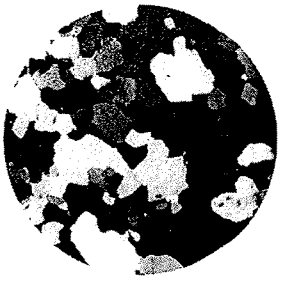

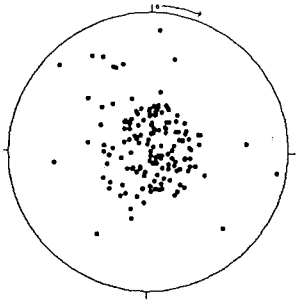

16
1652 m
n=160

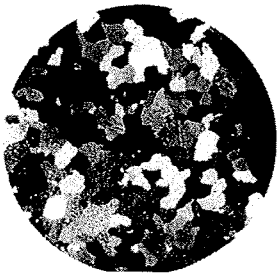

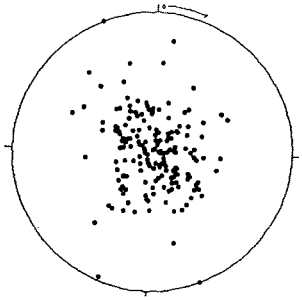

17
1790 m
n=174

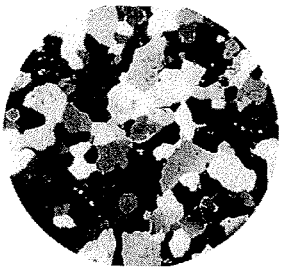

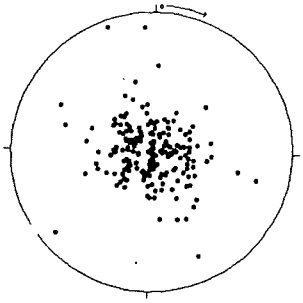

18
1899 m
n=200

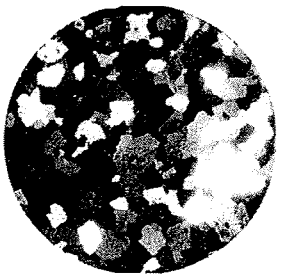

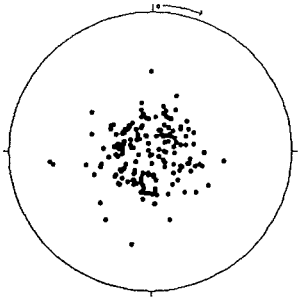

19
1982 m
n=175

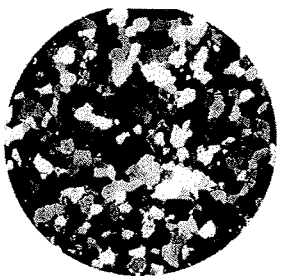

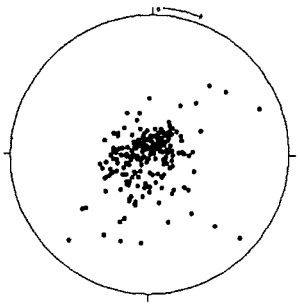

20
2064 m
n=200

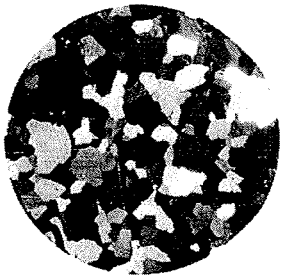

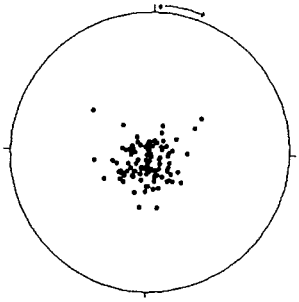

21
2174 m
n=100

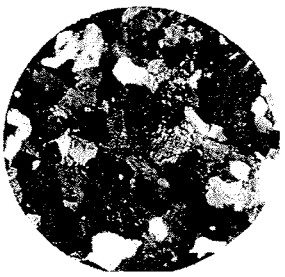

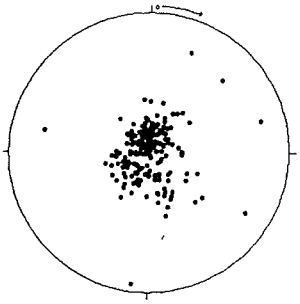

22
2284 m
n=200

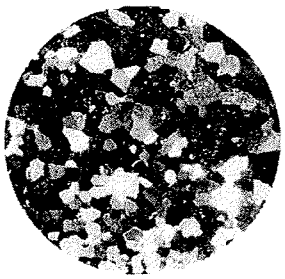

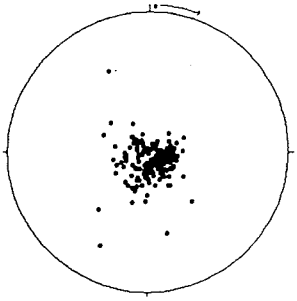

23
2394 m
n=170

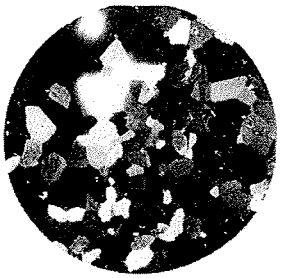

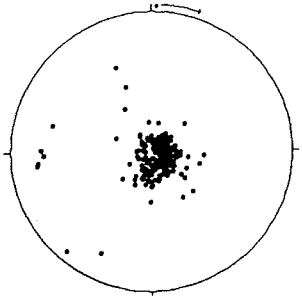

24
2449 m
n=189

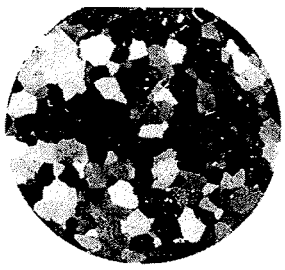

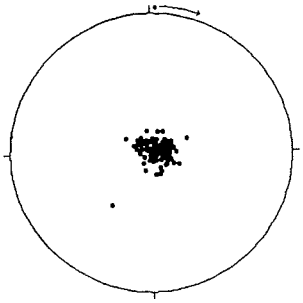

25

2587 m

n=120

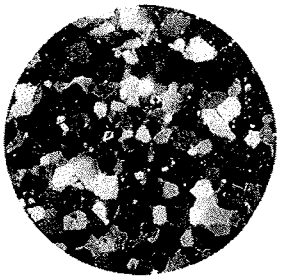

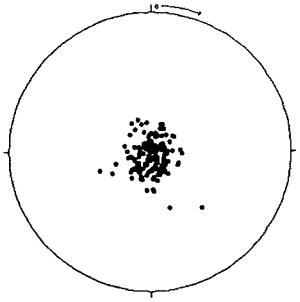

26

2696 m

n=150

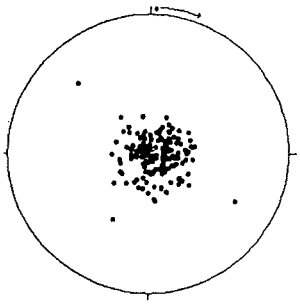

27

2779 m

n=163

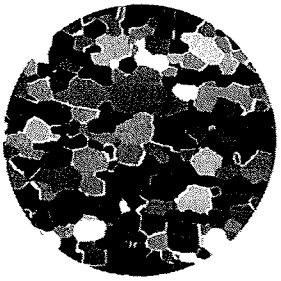

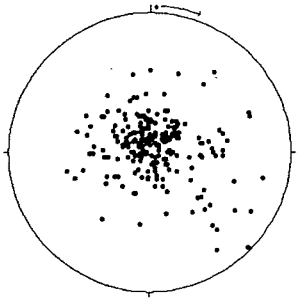

28

2796 m

n=230

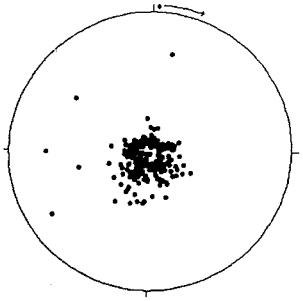

29

2807 m

n=200

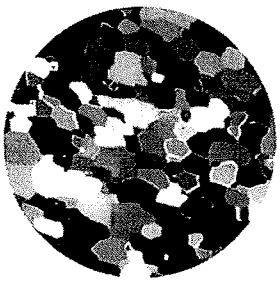

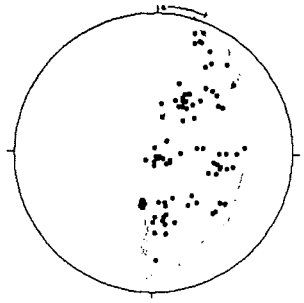

30
2862 m
n=88

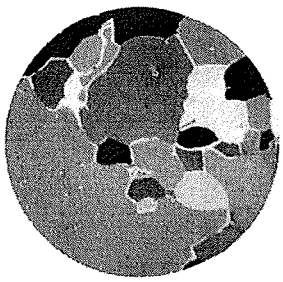

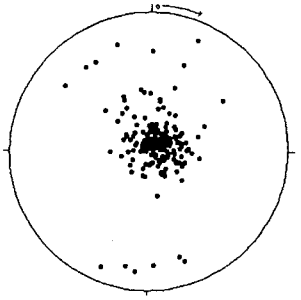

31
2889 m
n=192

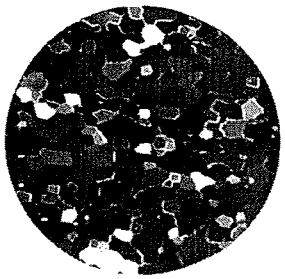

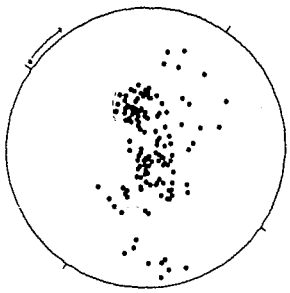

32
2944 m
n=141

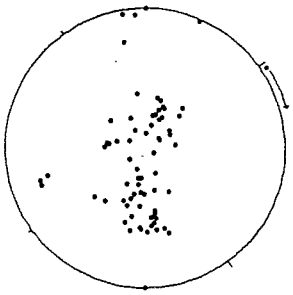

33
2971 m
n=71

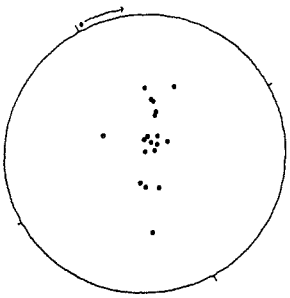

34
2999 m
n=19

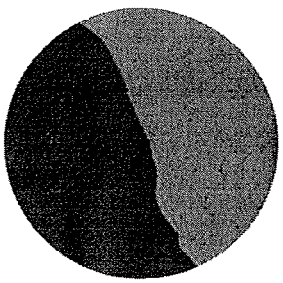

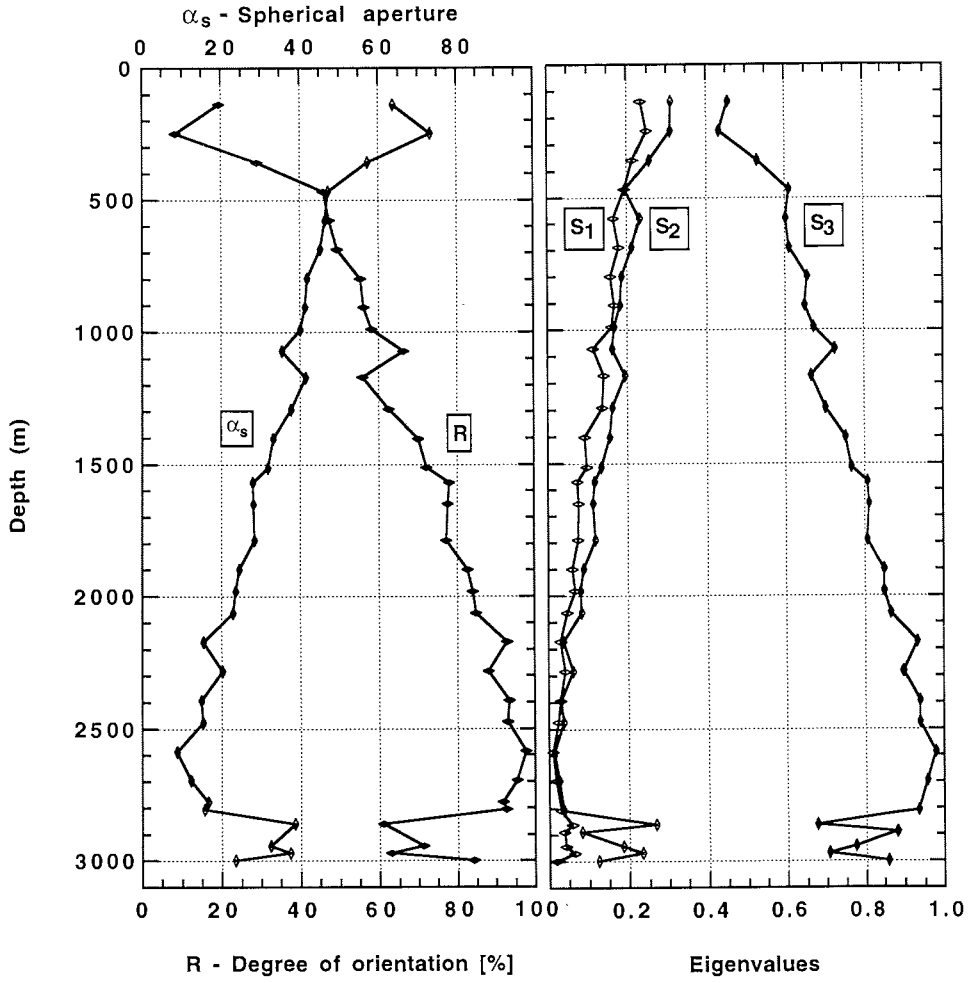

Fig. 4.3 - a) Degree of orientation (R) and spherical aperture (α_S) calculated for the fabric diagrams in Fig. 4.2. The parameters indicate a steady strengthening of the fabric down to 2600 m depth and a weakening below 2850 m.
b) Eigenvalues of the fabric diagrams in Fig. 4.2. The increase of s_3 and decrease of s_1 and s_2 is consistent with a strengthening of the fabric in one, preferred direction. The relatively small difference between s_1 and s_2 above 2850 m indicates that the point distribution does not deviate greatly from a circular shape. But in the stretched fabrics in the lowermost 150 m, the s_2-s_1 difference is seen to increase considerably.

core. The fabrics at 2944, 2971 and 2999 m appear as stretched, elliptically shaped single maxima. Fewer axes were measured for these diagrams than normal, since the grain size is larger and therefore fewer crystals are contained in each thin section. A weaker, less symmetric distribution is evident from the data in Fig. 4.3.

5. DISCUSSION

The results presented in Chapter 4 will now be discussed in detail. For an introductory overview of recrystallization regimes and fabric development processes the reader is referred to Sections 2.3 and 2.4.

5.1 CRYSTAL SIZE VARIATIONS

The normal grain growth regime

As discussed in Section 2.3, normal grain growth can by approximated by a parabolic growth law of the form

$$D^2 = D_0^2 + k \cdot t \qquad (2.20)$$

where D is the diameter at time t, D_0 is the initial diameter and k is the growth rate. The growth law predicts that grain area increases linearly with time. The steady increase in grain size between 100 m and 700 m in the GRIP core (Fig. 4.1) indicates that normal grain growth prevails in this depth interval. In Fig. 5.1, all grain size data obtained from this interval have been plotted against age, using the GRIP timescale. The data have been converted into areas assuming circular grain cross sections; the slope of the regression line is found to be $3.7*10^{-3}$ mm^2/yr. To correct for the sectioning effect, the grain areas must be multiplied by the correction factor 1.5 (Section 3.2). This yields a value of $k = 5.6*10^{-3}$ mm^2/yr for the grain-growth rate in the GRIP core, which compares very well with the value $5.8*10^{-3}$ mm^2/yr predicted by the regression line in Fig. 2.18. Woods (1994) reported a very similar value, $5.2*10^{-3}$ mm^2/yr, for the upper 600 m of the GISP2 core.

As mentioned in Section 2.3, the value of n in the growth law $D^n = kt$ is in general not 2 in metallurgical systems, but lies between 2 and 3 (Alley et al., 1986; Atkinson, 1988). In Fig. 5.2, growth curves assuming n=2, n=2.5 and n=3 have been fitted to the grain size data in the normal grain growth regime. The curve with n=2.5 is clearly seen to fit the data better than the two other curves. It is not clear, what causes the deviation from n=2 (Atkinson, 1988). The drag-effect of impurities is one possibility, but detailed studies of such

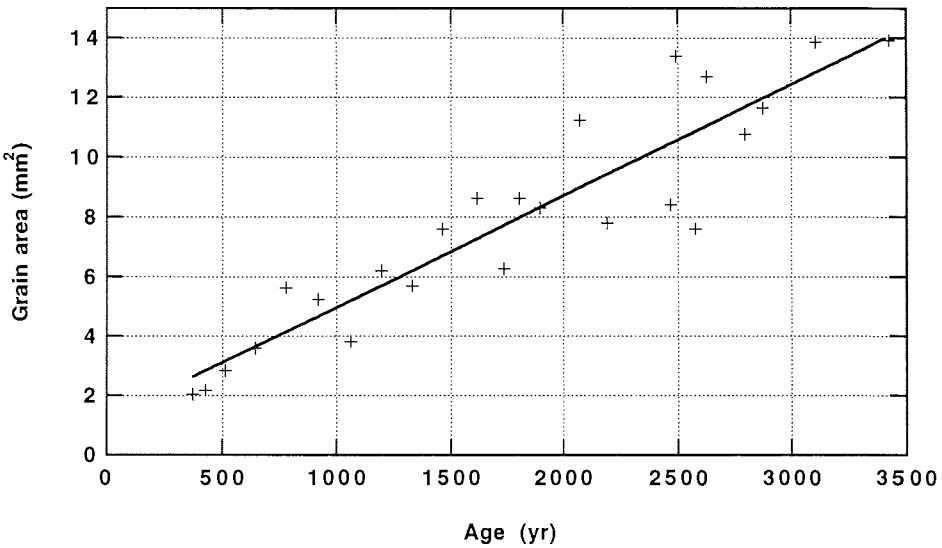

Fig. 5.1 Grain area versus age in the normal grain growth regime, assuming circular grain cross sections.

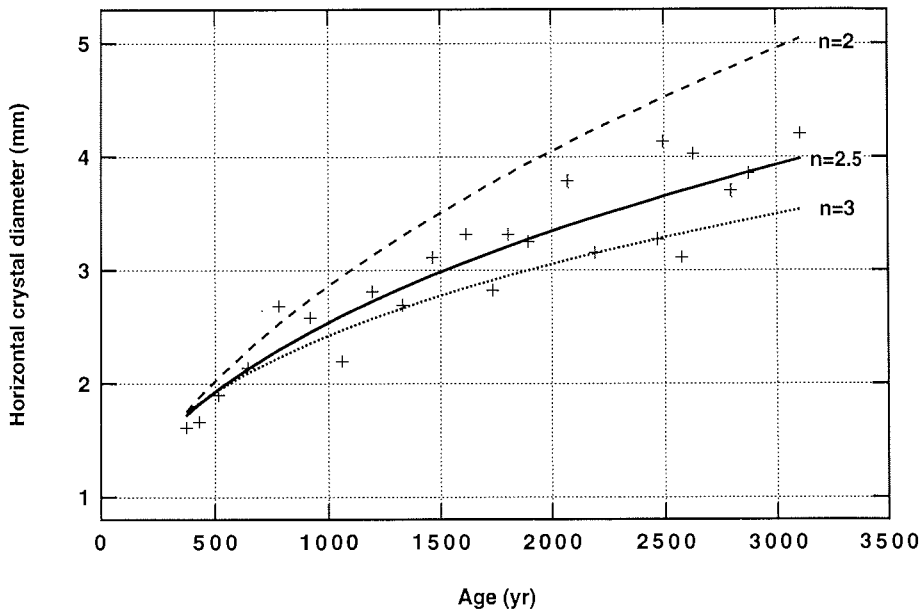

Fig. 5.2 Grain growth curves fitted to crystal size data in the normal grain growth regime, assuming different exponents, n, in the grain growth law. The full curve, which assumes n=2.5, fits much better to the data than the curves assuming n=2 and n=3.

effects have not been performed on the Holocene ice in the GRIP core. Results from the GISP2 core indicate that the effect of impurities on normal grain growth in this core cannot be excluded (Alley & Woods, in press), although it is not sufficient to stop grain growth.

Another characteristic of normal grain growth is the time-invariant shape of the grain-size distribution, when normalized by the average grain size (Atkinson, 1988; Srolovitz et al., 1984). Experimental data for metals suggest that the grain sizes are approximately log-normally distributed, i.e., the logarithms of the normalized grain sizes follow a Gaussian (Normal) distribution. No such data have been published on the grain-size distribution in deep ice cores.

Fig. 5.3 shows normalized grain-size distributions determined on three thin sections in the upper part of the GRIP core. A log-normal distribution has been fitted to the data in each case. The data from 221.1 m fit such a distribution reasonably well, with the exception of the high peak at $\approx 0.5\ \bar{d}$. The data from 633.6 m depth clearly appear to be log-normally distributed. At 1249.0 m, a tendency towards two populations is evident, one below $d/\bar{d}=1$, and one above. This sample is not from the normal grain growth regime, but the shape can still be approximated by a log-normal distribution. In all three cases, the maximum grain size appears to be close to three times the average size.

Although the data indicate approximately log-normally distributed grain sizes during grain growth, the data must be interpreted with care, since they have not been corrected for the sectioning effect. Some grains will be cut near their maximum diameters, whereas others will not, and this is likely to bias the results.

The polygonization regime

The stop in grain growth below 700 m has also been observed at a similar depth in other Greenland ice cores (Herron & Langway, 1982; Herron et al., 1985) and at 400 m depth in the Byrd core (Gow & Williamson, 1976). An effect of varying growth temperatures can be excluded as a cause, since surface temperature conditions have been stable in the Holocene and because the ice sheet is essentially isothermal down to 1800 m depth. Similarly, impurity-drag effects can be ruled out, since the impurity content is very low in the Holocene ice and does not increase at 700 m depth (Wolff et al., 1995). Gow & Williamson (1976) attributed the stop in grain growth to the effects of increasing strain in the ice; Alley (1992) suggested that the mechanism of polygonization (rotation recrystallization) is responsible, i.e. bending and eventually fragmentation of the ice crystals under increasing load (Section 2.3). If the rates of subdivision and grain growth are equal, average grain size will remain constant.

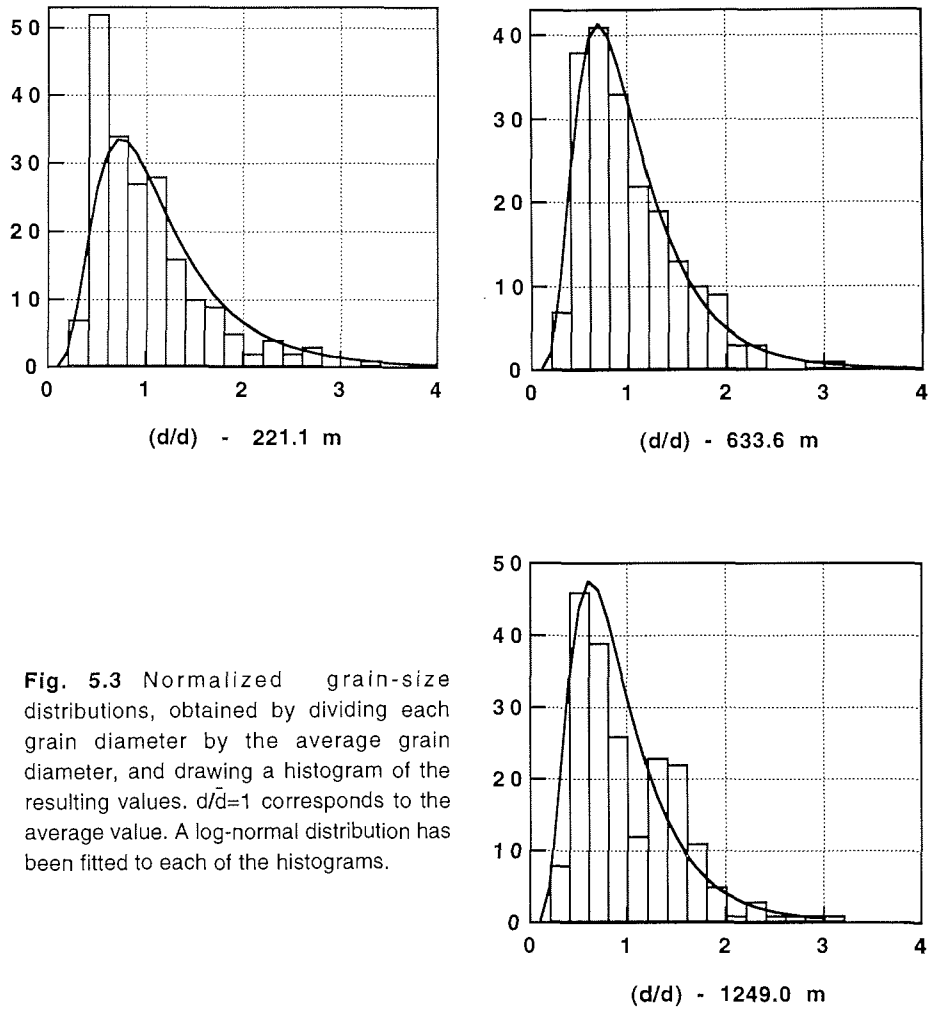

Fig. 5.3 Normalized grain-size distributions, obtained by dividing each grain diameter by the average grain diameter, and drawing a histogram of the resulting values. $d/\bar{d}=1$ corresponds to the average value. A log-normal distribution has been fitted to each of the histograms.

Polygonization of grains can be observed in thin sections, since misoriented parts of a grain which has become bent will reach extinction at slightly different inclinations in polarized light. Strain shadows are also commonly observed in those parts of grains where the lattice is being distorted. In addition, sub-grain boundaries forming between grain regions with different lattice orientations are observable as straight, thin lines crossing the grains. These phenomena were first observed at 380 m depth in the GRIP core and appear to occur commonly below 600 m, which supports the hypothesis that the stop in grain growth below 700 m is due to polygonization. Further evidence for subdivision of crystals can be inferred from the fact that both horizontal and vertical grain diameters are essentially constant in the interval 600-1600 m (Fig. 4.1). Since annual layers thin from 18 to 9 cm in this interval

(Dahl-Jensen et al., 1993) and since most crystals can be expected to experience the same vertical strain as the bulk ice, one would expect that with depth the crystals would become increasingly flattened and elongated in the horizontal plane, unless they are continually being subdivided by polygonization. Deeper in the core, little change is observed in the aspect ratio (ratio of horizontal to vertical diameters). Averages of the aspect ratios in the intervals 100-700 m, 700-1620 m and 1625-2790 m are shown in Table 5.1.

Another process which could stop the increase in grain size is the nucleation of new grains. Since this process is expected to produce grains with c-axes approximately 45° from the vertical (Section 2.4), fabrics would be expected to be affected, but this has not been observed. However, the effect would not be clearly detected in the fabric diagrams unless nucleation were occurring at a high rate. Nucleation of new grains however, is unlikely to be significant at a temperature of -32 °C, and in addition, the driving force for such recrystallization is not high enough (Section 2.3).
Alley et al. (1995) have measured the angles between the c-axes of neighbouring grains above and below the level where grain growth stops in the Byrd core, in order to test which process is responsible. Their reasoning is that polygonization would increase the number of small angles between adjacent grains, nucleation would increase the number of high angles and that impurity effects (boundary pinning) would not have a significant effect on nearest-neighbour relations. Their results support the hypothesis that polygonization causes the stop in grain growth.

The rate of polygonization can be estimated by the following simple calculation: Assume that each grain affected by this process is split into two grains. Let δt be the mean time interval during which each grain grows until being divided in two, such that the average grain area a_0 remains constant. A newly polygonized grain of size $a_0/2$ grows until it reaches the size a_0, and

TABLE 5.1 - ASPECT RATIOS

Interval	Regime	Aspect ratio
100 - 700 m :	Grain growth regime	1.22
700 - 1620 m :	Polygonization regime (Holocene)	1.32
1625 - 2790 m :	Polygonization regime (Wisconsin)	1.36

then it must polygonize again. Thus δt is given by

$$\frac{a_o}{2} + k\delta t = a_o \quad \Rightarrow \quad \delta t = \frac{a_o}{2k} \qquad (5.1)$$

With an average grain diameter of 4 mm (a_o = 13 mm) in the polygonization regime, and assuming the same growth rate as above 700 m ($k = 3.7*10^{-3}$ mm^2/yr, uncorrected), δt = 1800 years. Thus, within a sample containing 100 grains, grain size is constant if on average one grain polygonizes roughly every 20 years.

The stop in grain growth occurs at a depth where the vertical strain in the ice has reached 25% (Fig. 2.30). Since the ice becomes increasingly strained with depth, polygonization can be assumed to prevail at all depths below 700 m. The lower boundary of the polygonization regime can be taken as the level where grain sizes exceed the value attained at 700 m, implying that the effects of age and high temperature have overridden the effects of polygonization. This boundary can tentatively be put at the transition between Wisconsin and Eemian ice at ≈2800 m depth.

The Wisconsin ice: Impurity effects

The smaller crystal size in the Wisconsin ice is a feature common to all deep ice cores which reach into this period (Paterson, 1991). The following explanations of the crystal size decrease have been proposed:

1. Increased shearing in the Wisconsin ice, counteracting grain growth (Gow & Williamson, 1976).
2. A "memory" of the lower surface temperatures during the ice age, built into the crystal structure in the initial stages of firn densification (Petit et al., 1987).
3. Drag effects of impurities, located at grain boundaries (Koerner & Fisher, 1979; Alley et al., 1986).

Shearing is unlikely to cause smaller crystal sizes in the GRIP Wisconsin ice, because horizontal movement is negligible at this depth at the ice divide. The temperature-memory effect of Petit et al. (1987) probably can also be excluded, since this theory, originally developed for the uppermost 900 m of the Dome C ice core, does not take the polygonization process into account.

However, since the crystal growth rate varies with in-situ ice temperature one can ask whether the lower in situ temperature during the ice age is responsible for the smaller crystal sizes. The present temperature profile (Fig. 2.28), showing an approximately isothermal ice sheet down to 1800 m depth,

is due to heat advection processes, but the temperature in the normal grain growth regime must have been much lower during the Wisconsin than at present. The limiting grain size attained at 700 m depth during the ice age can be roughly estimated as follows: Assuming an accumulation rate of 50% of the present value (Dahl-Jensen et al., 1993), the age of the ice at 700 m would have been 7000 years at that time (Eq. 2.27). Assuming a growth temperature 22 K lower than in the Holocene (Johnsen et al., 1995), the Arrhenius term $k = k_0 \exp(-Q/RT)$ predicts a growth rate of $7*10^{-4}$ mm^2/yr. If the initial grain size is taken to be 1 mm, Eq. 2.20 predicts a limiting grain size of 2.7 mm under these conditions, which would have remained constant since this ice reached the 700 m level, if polygonization and grain growth were in balance (as they presently are in the interval 700-1600 m). The result fits very well indeed with the 2.8 mm average horizontal crystal size in the interval 1625.5-2000 m. However, the sharp change in crystal size across the Holocene-Wisconsin transition (Fig. 5.4) cannot be attributed to differences in growth temperature, since heat conduction would quickly have diffused the initial temperature gradient over such a small depth interval. The drag effects of impurities, discussed below, thus appear to be a more plausible mechanism.

Due to more vigorous atmospheric circulation during the ice age, higher concentrations of soluble and insoluble impurities are found in the Wisconsin parts of polar ice cores, for example at Dye 3 and Camp Century (Hammer et al., 1985; Herron & Langway, 1985), GRIP (Fuhrer et al., 1993; de Angelis et al., 1995; Legrand et al., 1995) and GISP2 (Mayewski et al., 1994). From data collected on Arctic Canadian ice caps, Fisher & Koerner (1979) suggested that microparticles inhibited grain growth in this ice. Duval & Lorius (1980) calculated the effects of microparticles (atmospheric dust in the size range 0.1-10 μm) on grain-boundary migration rates and concluded that the dust concentration in polar ice cores was too low to have a significant effect on grain-growth rates* . Alley et al. (1986a, 1986b) have analyzed these effects theoretically and compared theoretical predictions with ice-core observations. Their leading results are as follows.

1. The concentrations of microparticles (dust) in Holocene and Wisconsin parts of existing deep ice cores are too low to have a significant effect on grain growth. Only in ice with a very high content of atmospheric dust, volcanic ash or bedrock material are insoluble impurities expected to influence crystal sizes; small crystals (1-2 mm) are usually found in dirty looking ice.
2. Air bubbles do not appear to influence crystal growth significantly. [In the GRIP core, the disappearance of air bubbles appears prior to the Holocene-Wisconsin transition and the Wisconsin ice is devoid of bubbles].

---

* Duval & Lorius (1980) estimated the influence of microparticles on grain boundary migration with the equation: $P = \gamma(2/R - f/r_p)$, where γ is the surface energy, R is the grain radius, f is the fraction of the total volume occupied by the microparticles and r_p is the mean particle radius. This relation is essentially equation (2.16) with the term f/r_p added to it.

3. Soluble impurities, mainly chloride, sodium and sulphate ions, segregate to grain boundaries and, if present in high enough concentrations, significantly slow the migration of grain boundaries and thereby the grain growth. Alley et al. (1986b) conclude that the five-fold increase in the content of these impurities across the Holocene-Wisconsin transition in the Dome C core causes the drop in crystal size at this transition. Paterson (1991) reached the same conclusion regarding the transition in the Camp Century, Dye 3 and Byrd ice cores while Langway et al. (1988) found a strong anticorrelation between chloride/sulphate and crystal size along the Wisconsin ice in the Dye 3 core.

The data available on chloride and sulphate variations in the GRIP core are not extensive, but continuous measurements of calcium (Ca^{2+}) concentration have been performed in ice from 1300-3022 m depth (Fuhrer et al.,1993; Fuhrer, 1995). Since calcium is mainly derived from terrestrial dust (Clausen & Langway, 1989), calcium variations in the core can be assumed to closely mirror variations in the dust. Data from the Eemian part of the GRIP core also indicate that sodium, chloride and sulphate ions vary with climate in a similar manner as calcium and dust, i.e., their concentrations are low during warm periods and high during cold ones (GRIP Members, 1993; M. Legrand, pers. comm.). Such co-variation of major impurities is also observed across the stadial-interstadial climatic variations in the Wisconsin ice in the GISP2 core (Mayewski et al., 1994). It thus appears that variations in calcium content in the GRIP core can be assumed to reflect the general variation of soluble and insoluble impurities.

Fig. 5.4 shows grain size data in the interval 1300-2780 m, plotted together with calcium values obtained at the same levels. This interval includes the lowest 300 m of the Holocene and the entire Wisconsin ice. An anticorrelation is evident from these data. A tenfold increase in calcium occurs across the Holocene-Wisconsin transition; across the same transition crystal size decreases from 3.8 to 2.9 mm. Very high calcium values are found in ice dating from the last glacial maximum (1900-2000 m); there the smallest crystals (2.0 mm) occur. At 2750 m, the calcium content reaches its minimum in the Wisconsin ice (17 ppb), whereas the grain size reaches its maximum (5.25 mm). It should be pointed out, though, if impurities control grain-growth rates, that a fairly low impurity content appears sufficient to slow grain growth. The two samples at 1679 and 1790 m, for example, exhibit the same grain size, but widely different calcium values (28 and 220 ppb). This is in accordance with data from the Eemian part of the core (Thorsteinsson et al., 1995; see next section), where the inhibitive effect of impurities appears to play a role when calcium concentrations reach above 0.3 µmol/l (12 ppb), but reaches saturation above 0.6 µmol/l (24 ppb).

Thin sections have not been sampled in detail across the Dansgaard-Oeschger interstadial events, but the anticorrelation of grain size with calcium,

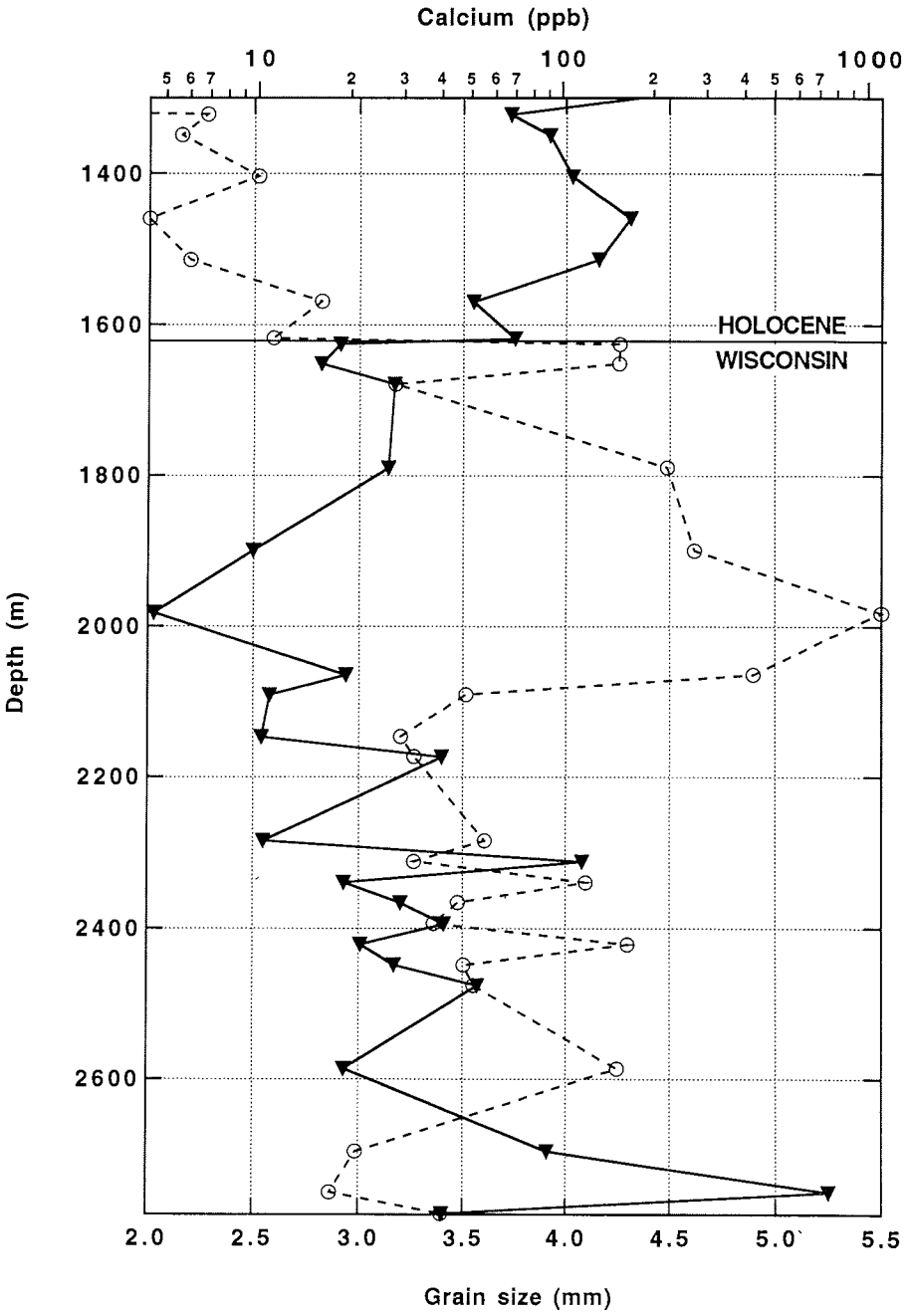

Fig. 5.4 Variation in horizontal grain size (triangles) and calcium (circles) between 1300 m and 2780 m. Note that the grain size data shown here are more detailed than in Fig. 4.1.

which in turn is strongly anticorrelated with $\delta^{18}O$ (Fuhrer et al., 1993), indicates that grain size is larger in the warm interstadial periods. The downward increase in grain size in the Wisconsin ice can probably be attributed to the increase in temperature, but the growth rate is very low. Between 2000 and 2700 m grain size has increased from 2 mm to 4 mm in ≈70.000 years, yielding a growth rate of $1.3*10^{-4}$ mm^2/yr, which is 1-2 orders of magnitude lower than predicted by the Arrhenius term for the temperatures in this interval. Clearly, impurities and/or grain subdivision are exerting a strong inhibitive effect on grain growth in the Wisconsin ice.

The Eemian ice: Crystal size as a climatic parameter

The unexpected results from oxygen-isotope analysis, indicating climatic instability during the Eemian interglacial, made it necessary to study other ice-core parameters in this period for comparison (GRIP Members, 1993). Within the framework of this collaboration, thin sections were prepared, continuously over the entire Eemian section (2790-2865 m), using leftover vertical strips from continuous chemistry measurements. The strips were 2 cm wide and 55 cm long. Vertical grain size was determined by counting linear intercepts along each 55 cm interval. The following discussion focusses on major results from a study of the Eemian grain-size variations, reported by Thorsteinsson et al. (1995).

The continuous crystal size profile is presented in Fig. 5.5, along with the $\delta^{18}O$ and calcium profiles, covering the interval identified as the Eemian. The climatic record indicated by the $\delta^{18}O$ isotope profile (Fig. 5.5a) has been described in detail by the GRIP Members (1993) and Dansgaard et al. (1993). The record indicates considerable climatic instability during the Eemian (marine isotopic stage 5e). Rapid variations occur early in the warm stage 5e5, which is followed by alternating cool (5e4 and 5e2) and warm periods (5e3 and 5e1). In addition, a catastrophic cold event (Event 1) is observed near the end of the Eemian, with $\delta^{18}O$ values plunging to -41‰ for roughly 70 years.

Turning now to the crystal size profile (Fig. 5.5b), a striking correlation between this record and the $\delta^{18}O$ profile is obvious from the figure. The average vertical crystal size is typically 3-4 mm in ice just above and below the Eemian and similar values are obtained in the cold stages of the interglacial. Much bigger crystals are observed in the warm periods, however, with average diameters ranging between 5 and 10 mm in stages 5e1 and 5e3, and reaching 20 mm in stage 5e5. The largest single crystal found in 5e5 has a vertical diameter of 70 mm, but average values drop to 3-5 mm during the cold events. In the catastrophic cold event occurring towards the end of the Eemian (Event 1 at 2797.0 - 2797.2 m depth), an extremely sharp drop in crystal size is observed, (see Fig. 5.6).

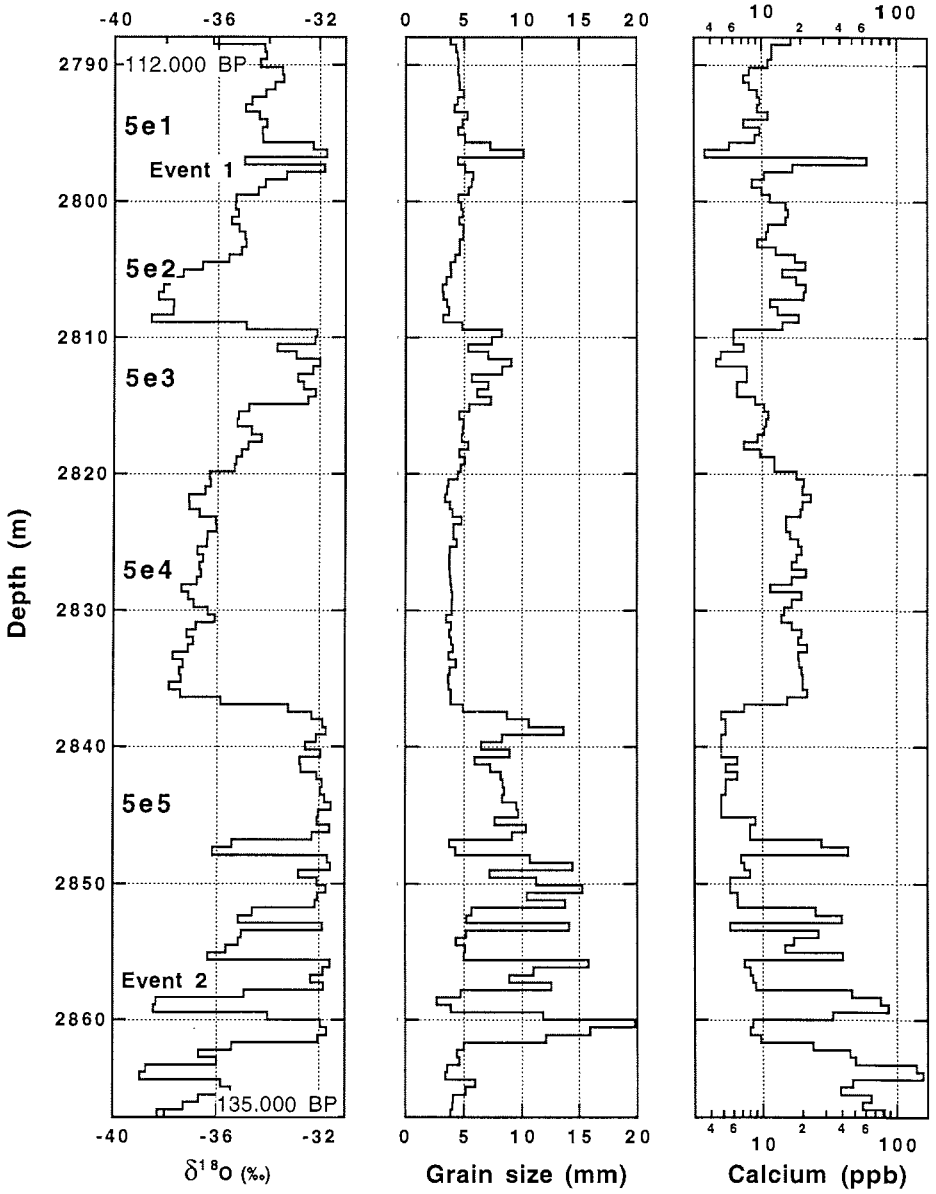

Fig. 5.5 a) Oxygen-isotope variations in the Eemian part of the GRIP core, as originally identified by GRIP Members (1993) plotted as 55 cm averages. Lower δ-values indicate colder temperatures at the time of deposition. The five sub-stages and the catastrophic Cold Events 1 & 2 are indicated. The resolution of the data in these diagrams is too low to show the full magnitude of Event 1, where δ-values reach a minimum of -40%. Age estimates are from GRIP members (1993). **b)** The crystal size profile over the Eemian (intercepts averaged over 55 cm intervals). **c)** The calcium profile, plotted on a logarithmic scale. This profile is expected to reflect the variations in impurity content in the Eemian.

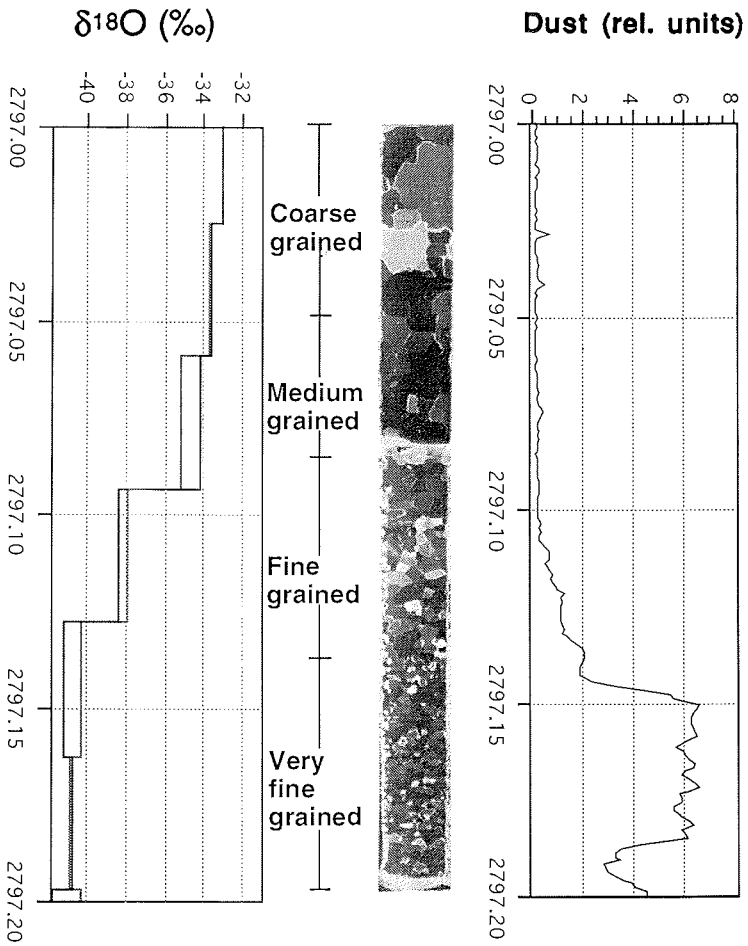

Fig. 5.6 The photo shows the sharp decrease in crystal size observed as Event 1 is entered. Average crystal size is 5-10 mm in the layers immediately above the event and 1 mm at the height of the event. A continuous dust profile, showing an increase in dust content in relative units, is plotted to the right of the photo. The maximum dust content reached is 1.2 mg/l, but outside the event the dust content is less than 0.1 mg/l. - The plot on the left shows $\delta^{18}O$ values from 3.4 cm samples. The solid line shows measured values, the broken line deconvoluted values to account for molecular diffusion in the ice (GRIP Members, 1993). δ-values are seen to drop steadily from -33 ‰ to a minimum of -41 ‰ at the height of the event.

Fig. 5.5c shows the continuous calcium profile. Comparison with the crystal size profile shows that high calcium content during cold periods (and therefore almost certainly elevated content of other impurities), correlates with small crystals, whereas a low calcium concentration is found in coarse grained ice dating from warm periods.

The grain sizes in the cold stages 5e2 and 5e4 are comparable with Wisconsin values and thus are probably due to slow, impurity-hindered grain boundary migration, combined with polygonization, whereas the large grains could result from nucleation and rapid growth of new grains (migration recrystallization). The relatively high temperature in the Eemian ice (-16 to -13 °C) favours this recrystallization process and the concentration of impurities is too low to slow the migration of grain boundaries. Note, however, that production of entirely new grains does not seem necessary; an enhanced rate of grain growth as compared with the rate of polygonization appears sufficient.

The detailed data on grain sizes and impurity content in the Eemian ice open up the possibility of studying the drag effects of impurities in detail. Below, the possible effects of atmospheric dust will first be evaluated, and then the effects of soluble impurities.

At Summit, impurity concentrations are comparable to those found at other Greenland locations. The dust content in the Warm-Eemian layers is typically on the order of 0.05 mg/l or less, but rises in Events 1 and 2 to 1.0 and 0.5 mg/l, respectively (see Figs. 2 and 3). These last values are comparable to Wisconsin values at Dye 3 (Hammer et al., 1985). Alley et al. (1986a) derived the following equation for the grain-boundary drag effect of microparticles:

$$\frac{P_p}{P_i} = \frac{9V_pR}{4r_p} \qquad (5.2)$$

where P_i is the intrinsic driving force for grain growth, P_p is the drag force due to microparticles, V_p is the volume fraction of particles, r_p the particle radius and R the average grain radius. The ratio P_p/P_i represents the relative fractional reduction in grain-growth rate. The relation is seen to predict an increased drag-effect with larger grain sizes, higher volume concentrations and smaller particle sizes. Applying this to the cold events 1 and 2 in the GRIP Eemian ice, where the crystals are smallest and the drag effects should thus be at a maximum, we use for the height of Event 1 a dust concentration of 1 mg/l ($V_p = 3.7*10^{-7}$), a grain radius R=1 mm and an average particle radius r_p=0.1 µm; probably an underestimate. This yields a P_p/P_i ratio of 0.01, i.e., only a 1% reduction in growth rate. For Event 2, the corresponding figure is less than 1% and still lower for the cold stages 5e2 and 5e4. From the available data, the model thus predicts drag effects far too low to be responsible for the observed grain size variations in the Eemian ice. Only if

the average particle radius were much smaller than r_p=0.1 μm, would a significant drag effect be expected; this can not be considered realistic (J.P. Steffensen, pers. comm.). As mentioned before, a strong anticorrelation between grain sizes and calcium/dust content can be inferred from the profiles in Fig. 5.5. If dust is the main factor controlling grain growth, then the results presented here suggest that a dust concentration of 0.5 mg/l is sufficient to cause smaller grain sizes in the cold Eemian stages and events.

Although continuous profiles of major ions, other than calcium, are not available from the Eemian ice, it can nevertheless be inferred from the available data that sodium, chloride and sulphate ions also are anticorrelated with crystal size (see Fig. 5.7). Table 5.2 presents typical values of these ions in the Eemian stages, together with values from Dye 3 and Camp Century. The following conclusions can be drawn from this comparison of the GRIP data with the other Greenland sites:

TABLE 5.2 - Impurity data

Ice core	Period	Dust (mg/kg)	Ca^{2+} (ppb)	Cl^- (ppb)	SO_4^{2-} (ppb)
GRIP	Warm Eemian	0.02	10	10	30
	Cold Eemian	0.5-1.0	20-40	20-25	55
	Event 1 max.	1.2	250	80	178
	Event 2 max.	0.5	120	40	96
Dye 3	Holocene	0.1	-----	19	22
	Wisconsin	0.5-3	-----	73	104
Camp Century	Holocene	0.1	5.1	34	34
	Wisconsin	1-2	50-160	95	168

Data on Dye 3 and Camp Century are from the following sources: Thompson & Thompson (1981); Herron & Langway (1985); Hammer et al. (1985); Paterson (1991).
GRIP data on dust,Cl^- and SO_4^{2-} have been provided by J.P. Steffensen & M. Legrand. The values presented for Warm Eemian are expected to be typical for the periods 5e1, 5e3 and 5e5; Cold Eemian values are typical for the periods 5e2 and 5e4.

1. Warm-Eemian values of Ca^{2+}, Cl^- and SO_4^{2-} are lower than or similar to Holocene values at Camp Century and Dye 3 - impurity drag effects are thus not expected in the warm stages with coarse-grained ice.
2. Values obtained in Eemian cold stages 5e2 and 5e4 are 25-50% of Wisconsin values at Camp Century and Dye 3.
3. Maximum values of these ions are obtained at the height of Event 1; these appear similar to ice age values at Camp Century.

Langway et al. (1988) demonstrated that crystal size is anticorrelated with sulphate in Wisconsin ice from Dye 3; Paterson (1991) concluded that chloride and sulphate ions are most important in slowing grain growth in the Camp Century, Dye 3 and Byrd ice cores. As evident from Fig. 5.7, however, these are not the only impurities which show an anticorrelation with crystal size and it seems difficult to conclude which impurity is most important. The data sets of these impurities available from the Eemian ice are not extensive enough for reliable correlation studies (except for calcium, see below), and in addition, it is not unlikely that the various impurities combine to produce the observed effect. It should be pointed out, though, that the concentration of chloride in the cold Eemian stages 5e2 and 5e4 with small crystals is typically 20-25 ppb, which is comparable to Holocene values at Camp Century (34 ppb) and Dye 3 (19 ppb), where grain growth is not inhibited, and much lower than Wisconsin values in these ice cores (95 and 73 ppb, respectively). If chloride ions were the controlling impurity, then the results presented here suggest that a concentration of 20 ppb is sufficient to slow grain growth.

Figure 5.8 dispays scattergrams for three data sets in Fig. 5.5; grain size, $\delta^{18}O$ and calcium. Clearly, grain size does not display a linear relationship to either of the two parameters, but separation of the data into the groups I-IV indicated on the graphs provides some interesting insights:

First, grain size (GS) for the group marked I in both the Ca/GS and $\delta^{18}O$/GS plots (GS>7 mm) appears largely independent of the other parameters. This clearly demonstrates that grain growth/recrystallization is not impeded in ice from warm periods with low impurity content (Ca < 0.3 µmol/l or 12 ppb) and corroborates the finding of Fisher & Koerner (1986) that a threshold impurity level must be reached before an effect on grain growth is observed.

In the group II in the Ca/GS plot (GS<7 mm and Ca<0.6 µmol/l), it appears that the inhibitive effect of impurities is beginning to play a role. Here, Ca is not significantly higher than for group I. However, for this group of samples (73 data points), both Ca/GS and $\delta^{18}O$/GS display strong linear relationships, much better than the entire data set, with correlation coefficients R = -0.71 and R = 0.84, respectively. It appears that for Ca >0.6 µmol/l (24 ppb) the inhibitive effect is already at its maximum, since group III in the Ca/GS plot (Ca> 0.6 µmol/l) does not have significantly smaller grain sizes.

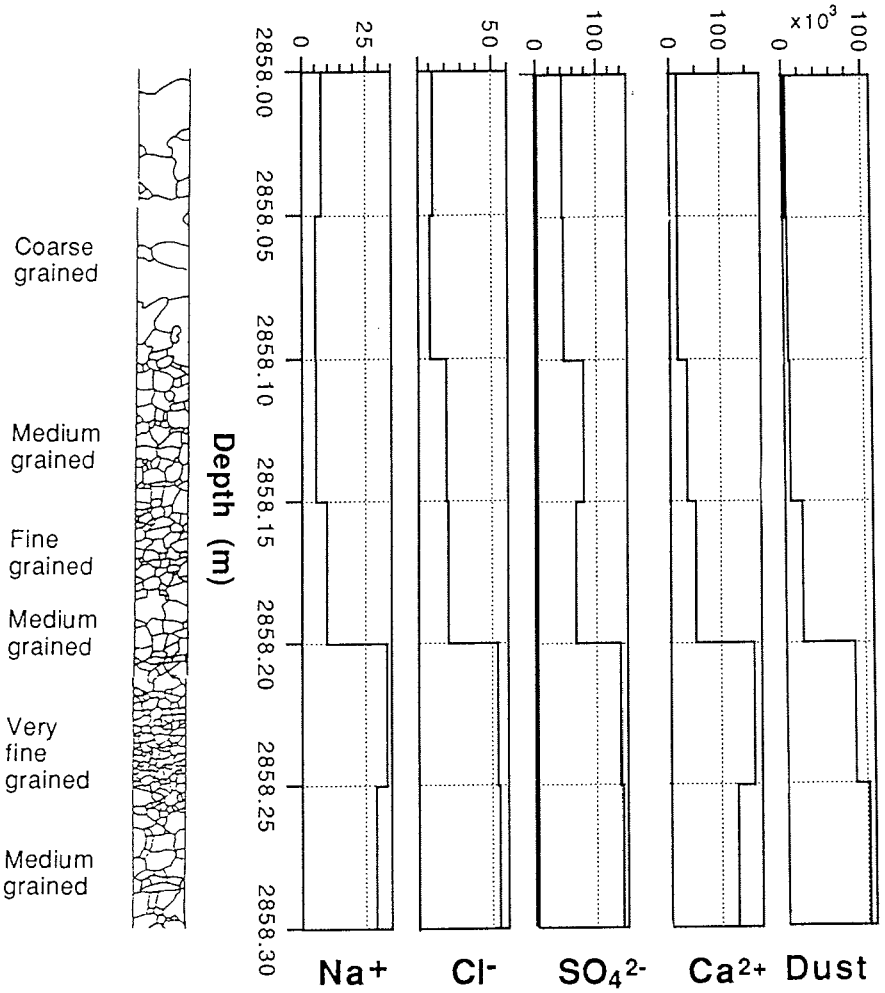

Fig. 5.7 Decrease in crystal size and increase in soluble and insoluble impurities in a 30 cm section as Event 2 is entered. Grain boundaries drawn from photos of vertical core strips are indicated on the diagram to the left. The width of the strip is 1.8 cm. Impurity measurements were performed on 5 cm samples (J.P. Steffensen, personal communication). Note the different scales. Grain size drops from 10 to 3 mm; the increase in sulphate is 3-fold, in sodium and chloride 5-fold and in calcium 8-fold. Concentrations are in ppb. Dust is expressed in number of particles > 0.5 μm in each 5 cm sample, and increases 20-fold from 5000 to 100 000 particles. The maximum value corresponds to 0.5 mg/l.

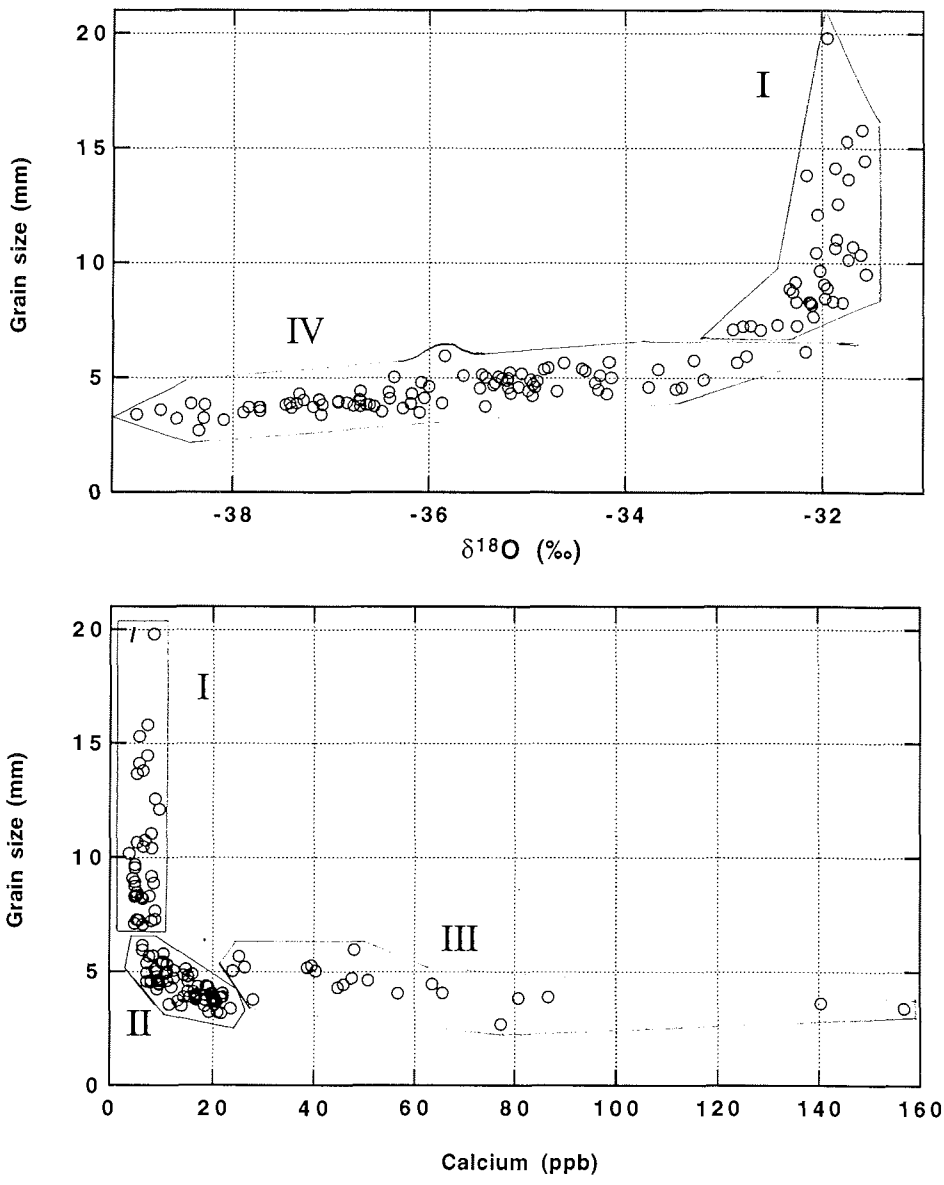

Fig. 5.8 Plots of grain size versus a) $\delta^{18}O$ and b) calcium. The data points represent 55 cm averages. The data groups I - IV referred to in the text are indicated. Groups II and III in the Ca-GS plot correspond to group IV in the $\delta^{18}O$-GS plot.

The most striking feature observed in these plots is the strong linear relationship between grain size and $\delta^{18}O$ between δ = -33 ‰ and δ = -39 ‰ (group IV in the $\delta^{18}O$/GS plot). The correlation coefficient is R = 0.81 (93 values) between $\delta^{18}O$ and grain size for this group of points, which strongly suggests that some factor related to $\delta^{18}O$ is controlling grain growth in this ice. For the points in the Ca-GS plot corresponding to group IV in the $\delta^{18}O$-GS plot, the correlation coefficient between Ca and GS is only -0.30 (cf. -0.71 for group II). Samples with widely varying Ca-values have similar grain sizes for this group of points; a behaviour which might be caused by a saturation effect.

A further indication for stronger variation of grain size with $\delta^{18}O$ than with impurities can be inferred from a close inspection of Fig. 5.6, where grain size, $\delta^{18}O$ and dust values in Event 1 are displayed. Both $\delta^{18}O$ and grain size appear to decrease gradually from 2797.0 m to 2797.15 m, whereas the dust level first starts rising below 2797.10 m and only below 2797.14 m exceeds the value 0.5 mg/l (= 3 on the relative scale of Fig. 5.6) which previously was found to be the minimum dust content for inhibition of grain growth (if this effect is present).

The lowest 160 m: Migration recrystallization?

In Fig. 5.9, crystal sizes below the Eemian ice are depicted along with $\delta^{18}O$ and calcium data. Note that only spot measurements of crystal size are available from this interval. Small crystals are found in the low-δ/high-Ca ice between 2880 and 2900 m, which probably dates from the Saalean ice age (although flow disturbances are evident in this interval). Crystal size increases abruptly to 20 mm in the narrow, high-δ/low-Ca layer between 2915 and 2920 m, but drops to 5 mm below this layer. The correlation of crystal size with $\delta^{18}O$ and calcium breaks down below 2940 m; the crystal size increases steadily downward to 3022 m while the other parameters do not display large variation in this interval. Here, the effect of high temperature near the bottom appears to override the inhibitive effect of impurities, even though the calcium level (20-100 pp) is above the threshold level found in the Eemian ice. In addition, the inhibitive effect of sodium and chloride ions would be expected to vanish at -21 °C, the NaCl-H_2O eutectic temperature, above which a liquid NaCl-phase might speed grain growth (Alley et al., 1986b). It seems, however, difficult to argue that such a process is acting to increase grain-growth rates in the lowest 100 m, since the temperature already reaches -21 °C at 2500 m and impurities appear to slow grain growth down to 2940 m.

The presence of coarse grained ice (> 1 cm) in the warm stages of the Eemian and below the Saalean stands in contrast to the situation at Camp Century and Dye 3 (Herron & Langway, 1982; Herron et al., 1985), where the lowest part of the ice sheet is fine grained throughout. Alley & Woods (in review) have reported the occurrence of coarse grained ice in the lowest 200 m of the

GISP2 core, and thus the situation in Central Greenland appears similar to that at Byrd Station, Antarctica, where coarse grained ice is present in the lowest 350 m of the ice sheet (Gow & Williamson, 1976). The temperature in this part of the Byrd borehole increases from -15 °C at 1800 m depth to the pressure melting point (-2 °C) at the bottom, and Gow & Williamson (1976) thus interpreted the large grains to result from recrystallization (migration recrystallization according to the terminology in Table 2.1 - see Section 2.3). Since the temperature reaches -15 °C in the GRIP core where coarse grained ice first appears (2800 m), and increases to -9 °C at the bottom, the ice is probably warm enough for rapid recrystallization to occur. The process is, however, poorly understood, and a study of fabric diagrams No. 28 and 30-32 in Fig. 4.2, which all are from coarse grained samples, does not lend direct support to its occurrence. As demonstrated in laboratory tests, new grains in recrystallization form with c-axes at high angles (≈45°) to the axis of compression (Budd & Jacka, 1989; Alley, 1992 - see Section 2.4). A ring-like c-axis distribution with multiple maxima results, and has been observed in the lowest 100 m of the Byrd core (Gow & Williamson, 1976). Such fabrics are not observed in the lowest part of the GRIP core, although some clustering into separate maxima can be detected, particularly in the fabric at 2861.65 m. A fabric diagram measured on thin sections cut just above the transition into the silty ice shows some resemblance to the Byrd girdle fabrics (Tison et al., 1994; Fig. 2), although the girdle is not well developed.

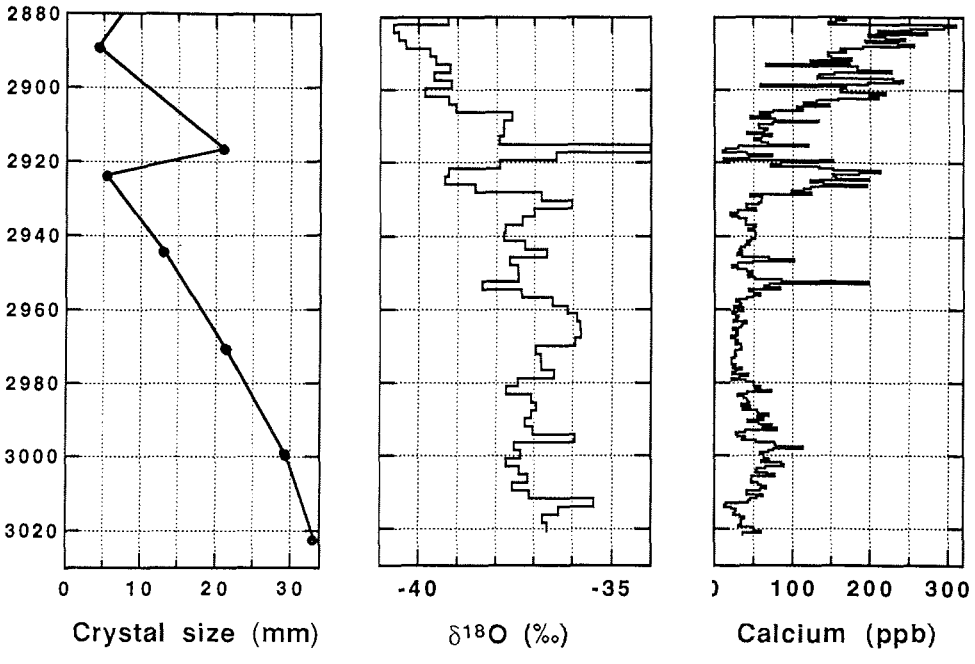

Fig. 5.9 Crystal size, $\delta^{18}O$ (2.2 m averages) and calcium (0.55 m averages) below 2880 m in the GRIP core.

Migration recrystallization is believed to produce grains which have interlocking shapes (Duval & Castelnau, 1995), in contrast with the equant shapes observed in the normal grain growth and polygonization regimes. Inspection of the photographs of thin sections No. 30, 32 and 33 in Fig. 4.2 indeed reveals that some of the large grains display irregular, interlocking shapes, but this is not observed in all thin sections from the coarse grained ice. It should also be remembered, that the nucleation of new grains will actually counteract an increase in grain size, unless the new grains grow very rapidly.

An alternative explanation of the presence of large crystals (up to >10 cm in diameter) in the lowest part of the core is simply the high age of the ice, combined with the effect of higher temperatures near the bottom. The low-impurity parts would have experienced accelerated rates of grain growth near the bottom and polygonization/nucleation would not be rapid enough to counteract the increase in grain size.

The silty ice

The lowest 6 meters of the GRIP core consist of debris laden basal ice, usually termed silty ice. Comprehensive studies on this part of the core have been carried out by the Belgian group at the Université Libre de Bruxelles, in cooperation with other institutes involved in GRIP. The work done at ULB involved preparation of a continuous series of thin sections spanning the basal ice unit, for detailed studies of textures and fabrics, performed jointly by ULB and AWI and reported by Tison et al. (1994). A brief overview of results from crystal size measurements in the silty ice, carried out at AWI, is presented in this section.

Souchez et al. (1994, 1995) have presented data on isotopic composition and gas concentrations in the silty ice. They interpret this ice as being of local origin, initially formed at the ground surface in the absence of the ice sheet. At a later stage, it was overridden by the growing ice sheet and mixing between the glacial ice and the ground-formed ice occurred. No indication of melting-refreezing processes has been found in the basal ice, but extremely high concentrations of CO_2 and methane, which preclude atmospheric origin, indicate formation in a marshy environment.

In Fig. 5.10, results from crystal size measurements in the silty ice are shown, along with data on debris content and δD. δD varies completely in parallel with $\delta^{18}O$ (R. Souchez, personal communication). The rapid variations in the uppermost 1 m of the sequence reflect the interbedding of clean, coarse grained glacial ice with fine grained ice containing dirt particles. Below 3024 m, crystal size shows variations which, on close inspection, appear anticorrelated with the weight percentage of impurities. A similar result was

obtained in a study of grain sizes and impurity content in basal ice from the Dye 3 core (Thorsteinsson, 1990); fine grained ice was also found in silty ice cores from Camp Century (Herron & Langway, 1979) and Byrd Station (Gow et al., 1979).

Comparison of the profiles in Fig. 5.10 reveals a surprising anticorrelation between grain size and δD (and $\delta^{18}O$) values. Small crystals appear in ice with higher δ-values and larger crystals in ice with lower δ-values - the opposite of the relation found in the Eemian ice and other parts of the core. But since the crystal size is anticorrelated with impurities in both cases, this can be taken as a strong indication that impurities do exert an influence on the migration of grain boundaries, if present in sufficient concentrations. The variation of δ-values with impurity content must be related to the formation process of this ice.

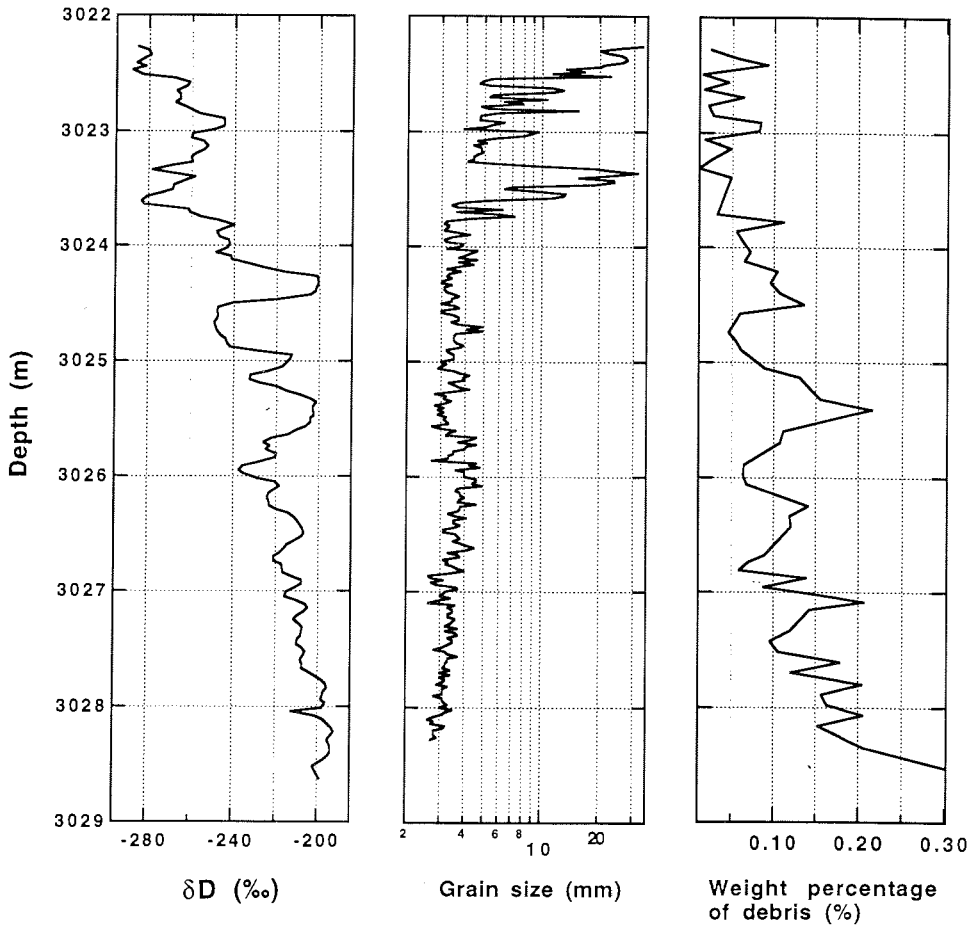

Fig. 5.10 Data on crystal size, δD and debris content in the silty ice.

5.2 CRYSTAL FABRIC DEVELOPMENT

Overview

It is evident from Figs. 4.2 and 4.3 that the development from a random to a preferred fabric is very steady and regular in the GRIP core. This would seem to indicate a stable flow regime at Summit, and the evolution towards a single maximum fabric is consistent with the ice divide position, where ice movement is mainly vertically downwards. Alley (1988) concluded from a modelling study that an elliptical single maximum will form in pure shear, whereas a circular one will be produced under uniaxial compression (see Fig. 2.8). The GRIP fabrics show little deviation from circular shape and thus the fabric development appears to be dominated by the rotation of c-axes towards the axis of vertical uniaxial compression. The compression axis can be taken to coincide with the core axis, since the drill hole did not deviate more than 3° from the vertical (Johnsen et al., 1994). For the diagrams in the upper 2800 m, the average c-axis does not deviate more than 10° from the center of the diagram, and is usually within 1-6° of the core axis.

Histograms of the c-axis inclinations from the vertical at five different depths are presented in Fig. 5.11, to give some idea of the inclination changes during the formation of the single maximum. A strong single maximum can be said to have formed below 2100 m depth, where R exceeds 90% and $\alpha_s < 20°$.

Fig. 5.12 shows the percentages of c-axes in each 10° interval, calculated for the fabric diagrams between 100 m and 2800 m depths. The main features are: The intervals 80-90°, 70-79° and 60-69° start out with as many, or more, c-axes as the other intervals, but the percentage of axes within them decreases drastically already in the uppermost part of the core. The curves for the intervals 50-59° and 40-49° are very similar and show almost steady percentages down to 700 m and a slow decrease from this depth downward. The curve for 30-39° shows a rapid increase to a maximum of 24% at 900 m, and a decrease below that. The increase down to 900 m is clearly due to the axes, which initially were further out, rotating through this interval. In the interval 20-29° a maximum of 30% is reached at 1600 m and below that a rapid drop is observed. Finally, the curves for 10-19° and 0-9° both show steady increase in the entire interval being considered, and in the lowermost part about 50% of the c-axes are within 10° of the vertical.

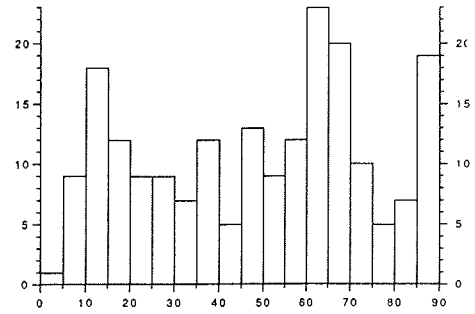

139.15 m

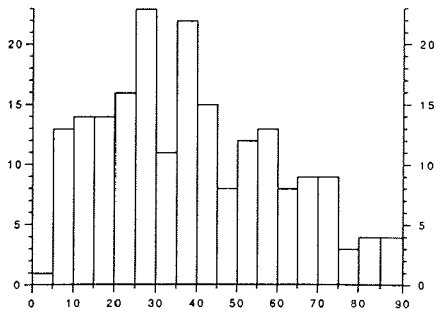

579.15 m

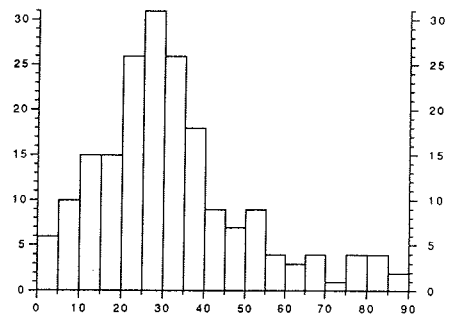

1292.51 m

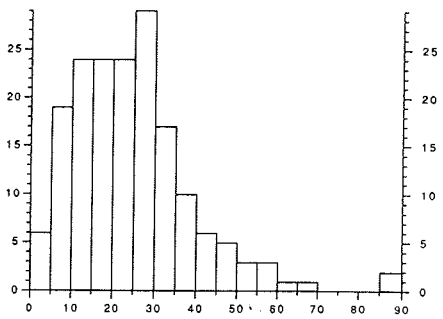

1789.7 m

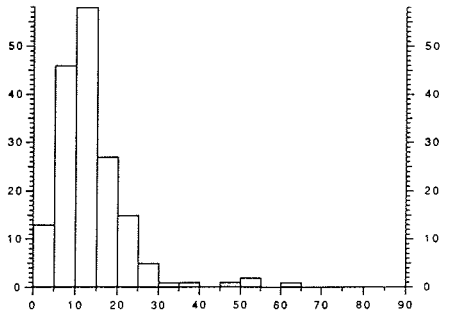

2394.15 m

Fig. 5.11 - C-axis inclination histograms for fabric diagrams No. 1, 5, 12, 17 and 23 in Fig. 4.2. The number of c-axes within each 5° interval is shown. 0° is the vertical.

Formation of the single maximum

Since the fabric starts to contract already in the normal grain growth regime (above 700 m), it seems clear that grain rotation and grain growth can occur simultaneously. The onset of polygonization at 700 m does not appear to slow the fabric evolution, although polygonization can be expected to counteract the process of rotation towards the vertical. However, this effect will not be great, and a subgrain which initially has rotated away from the axis of compression while it was being polygonized, will eventually rotate towards it again. The entire polygonization regime appears affected by grain rotation towards the vertical, both the low-impurity Holocene part and the Wisconsin ice with high impurity content. Nucleation of new grains with c-axes initially at 45° from the vertical is unlikely to be occurring to any significant extent; the fabrics between 2100 m and 2850 m show very few axes outside the central single maximum.

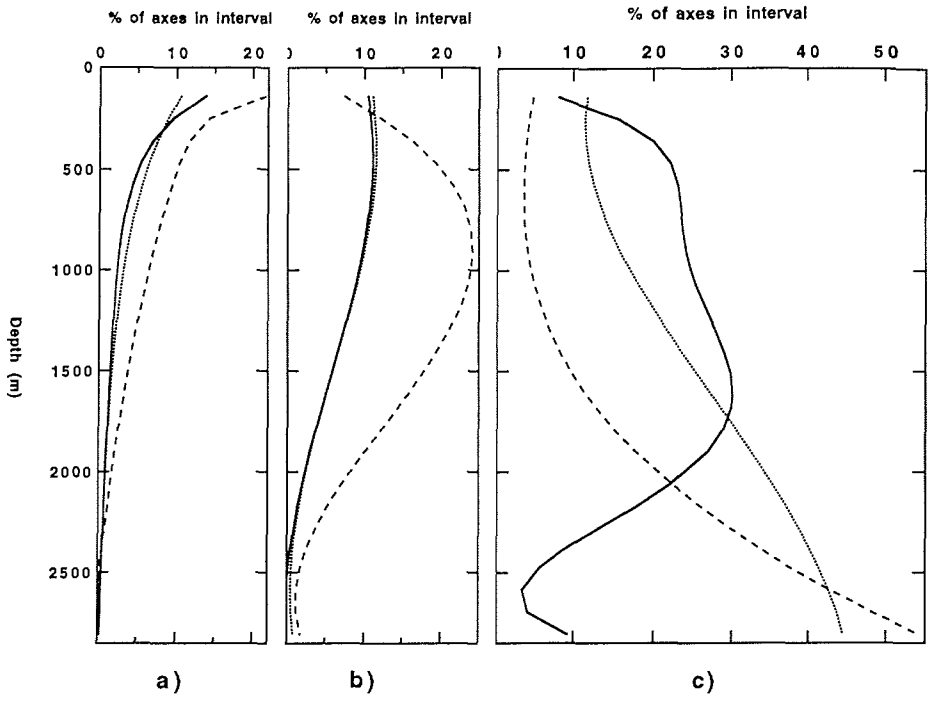

Fig. 5.12 - Percentages of c-axes within each 10° interval of the fabric diagrams in the upper 2800 m. Curves fitted to raw data are shown. **a)** Full line: 80-90° from the vertical; dotted line: 70-79°; dashed line: 60-69°. **b)** Full: 50-59°; dotted: 40-49°; dashed: 30-39°. **c)** Full: 20-29°; dotted: 10-19°; dashed: 0-9°.

In deformation tests carried out in the laboratory, strong single maximum fabrics have been produced under simple shear conditions (Bouchez & Duval, 1982; Budd & Jacka, 1989). In the GRIP core, stratigraphic features indicative of simple shear deformation are first observed after the single maximum has been attained (Chapter 6). Therefore, simple shear is not likely to be of importance in producing the single maximum, but is rather initiated after its formation.

In laboratory tests, simple shear deformation produces two maxima, one at the pole of the shear plane and the other near the shear plane, in the shear direction (Kamb, 1972; Bouchez & Duval, 1982; Paterson, 1994). The second maximum tends to disappear as deformation proceeds. Such two maxima fabrics have not been observed with certainty in ice sheets, however, and inspection of the GRIP fabrics shows no clear indication of a second maximum. The fabric at 2889.15 m has some outlying c-axes near the shear plane, but these appear on both sides of the single maximum. The absence of a second maximum is probably an additional indication that simple shear does not play a role in producing the single maximum at Summit, but is initiated after the single maximum has formed.

Assuming that the strong single maximum is fully developed at 2100 m depth, its formation is achieved in 30.000 years. In the Byrd, Camp Century and Dye 3 cores, fabrics of similar strength appear to have formed below the Holocene-Wisconsin transition, in 12-15.000 years old ice (Gow & Williamson, 1976; Herron & Langway, 1985; Herron et al., 1985). The rotation rate is likely to proceed faster at these drill sites, since ice temperatures and strain-rates are higher than at Summit.

Azuma & Higashi (1987) presented clear evidence from experiments and modelling that the single maximum in the Dye 3 core was formed by grain rotation towards the axis of vertical compression. They related fabric strength to strain by plotting the median angle θ_m of fabrics versus cumulative vertical strain. In Fig. 5.13, the results of Azuma & Higashi from the upper 800 m of the Dye 3 core have been plotted along with results from the upper 2800 m of the GRIP core. The good agreement found between the data from both cores, for strains up to 50%, indicates that fabric strengthening is primarily related to the total strain experienced by the ice.

Fabrics in coarse grained ice

Migration recrystallization, forming coarse grained ice at relatively high temperature is believed to show a fabric signature in the form of a girdle with multiple maxima, centered on the axis of compression (Gow & Williamson, 1976; Alley, 1992 - see discussion in Sections 2.3 and 2.4). No such girdle has been found in fabrics from coarse grained ice in the GRIP core. All fabrics from below 2850 m depth display some degree of stretching in the horizontal plane, which could indicate a change in stress conditions in the lowest part of the ice sheet. The fabric at 2862 m (No. 30) resembles the vertical girdles, centered on the axis of longitudinal extension, which are obtained below 1200 m depth in the Vostok core (Lipenkov et al., 1989). Similarly, the three fabrics below 2900 m depth (No. 32-34) resemble pure shear fabrics modelled by Alley (1988), in which stretching into elliptical shapes is found to occur transverse to the tensional axis. These fabrics could thus indicate that tensional stresses, probably in the east-west direction, are acting in the lowest 170 m of the ice sheet.

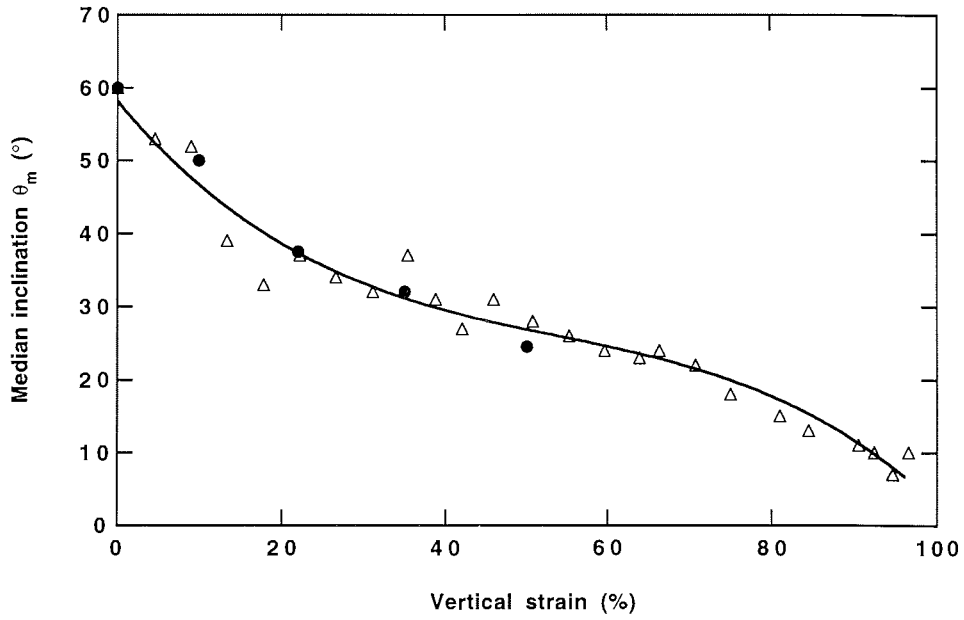

Fig. 5.13- Median inclination θ_m versus vertical compressive strain. θ_m is the angle from the vertical within which 50% of the c-axes in a fabric diagram lie. Strain is found from $(1-a/a_o)*100\%$, where a_o is the original thickness of a layer at the surface and a its thickness at the present depth. The curve is fitted to the GRIP data, which are shown as triangles. The filled circles are data from the Dye 3 core, taken from Azuma & Higashi (1985).

Simulation of the GRIP fabrics

In recent years, several studies dealing with the modelling of fabric evolution have been published. The geometrical model outlined in Section 2.4 was successfully used by Azuma & Higashi (1985) to simulate fabric evolution in the upper 800 m of the Dye 3 core. Van der Veen & Whillans (1994) and Castelnau & Duval (1995) used the so-called static model to simulate fabric development. In this model, the stress on each grain equals the bulk stress applied to the sample, and each grain is assumed to deform only by basal glide. Modelled fabrics are similar to those observed in ice sheets, including simple shear fabrics. A difficulty with this model is that the deformation of adjacent crystals is incompatible; i.e. gaps and overlaps between crystals are produced.

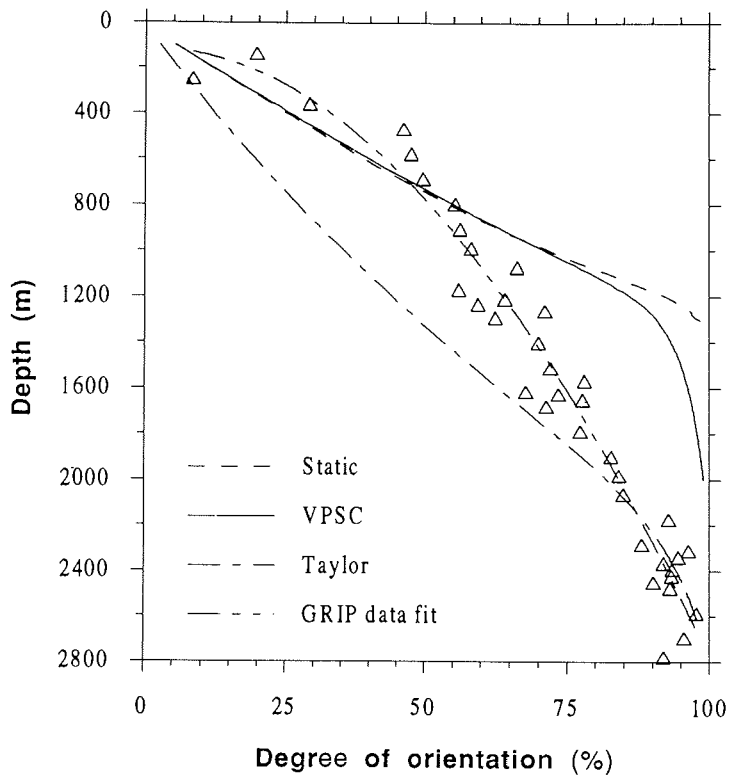

Fig. 5.14 - Evolution of the degree of orientation with depth: Results from three different models compared with GRIP data (triangles). From Castelnau et al. (in press).

Castelnau et al. (1995) have recently applied both the Taylor model (Taylor, 1938) and the Viscoplastic Self-Consistent (VPSC) theory of Hutchinson (1976) to fabric development in ice. The Taylor model assumes homogeneous strain rate within the polycrystal; i.e. grains with different orientations deform at the same rate. This assumption leads to compatible deformations between grains, but violates stress equilibrium across grain boundaries. The VPSC model takes into account compatibility and stress equilibrium, and the stresses and strain rates of the individual grains can be different from the bulk stress and strain rate. Slip on prismatic and pyramidal planes is taken into account, in addition to basal slip. Crystals are assumed to deform by dislocation glide only and recrystallization processes are not taken into account.

The models outlined above have recently been used to simulate the fabric evolution in the GRIP core (Castelnau et al, in press). The input to each model is a randomly oriented polycrystal containing 200 grains, and the imposed deformation is vertical uniaxial compression. The rotation of each grain for a certain strain increment is calculated, and the simulation is carried out to the level of total strain reached at 2800 m in the core. Figure 5.15 summarizes the results, presented as the evolution of the degree of orientation (R) for modelled fabrics along with GRIP data. It appears that the static and VPSC models reproduce the actual fabric evolution fairly well down to a depth of 800 m, but below that these models predict a much more rapid strengthening of the fabric than observed in the core. As shown by Castelnau et al. (in press), this discrepancy can been attributed to the effects of rotation recrystallization (polygonization), which tends to slow grain rotation towards the axis of compression. The Taylor model predicts a slower initial fabric evolution, but fits with the GRIP data below 2000 m depth. This model, however, does not yield a realistic prediction of fabric development since a considerable contribution of non-basal slip systems is required to produce the observed results (Castelnau et al., 1995).

5.3 FLOW PROPERTIES OF SUMMIT ICE

The results from the crystal fabric measurements clearly demonstrate that the ice at Summit becomes strongly anisotropic with depth. The gradual development towards a single maximum fabric can be expected to harden the ice against vertical compression and soften it against simple shear. In addition, variations in crystal size and impurity content might influence the flow properties. Variations in flow properties will, in turn, introduce complications in the age-depth relation and have to be taken into account in realistic modelling of the large-scale flow behaviour of the ice sheet. Of special interest is the problem of rheological contrasts across climatic transitions, which will be discussed in the following sections. After that, some results from deformation tests on GRIP samples will be described briefly.

The "soft" ice age ice problem

During the last two decades, results from borehole measurements and mechanical tests on core samples from Northern Hemisphere ice sheets have demonstrated that the ice age ice (Wisconsin ice) in the lower parts of the ice sheets is "softer" than the Holocene ice above, i.e., that it deforms 3-4 times more readily in horizontal shear. Hooke (1973) found higher inclinations (and therefore enhanced deformation rates) in Wisconsin ice in boreholes drilled on the Barnes ice cap in Arctic Canada, and similar results have been obtained from the Devon and Agassiz ice caps (Paterson, 1977; Fisher & Koerner, 1986). More recent measurements in the Dye 3 and Camp Century boreholes (Hansen & Gundestrup, 1988; Gundestrup et al., 1993) show a common pattern, which in Fig. 5.15 is illustrated with data from Dye 3. The horizontal shear strain rate is very low in the Holocene ice, increases rapidly at the transition into the Wisconsin ice, and increases still further when the silty ice, which comprises the lowest 25 m of this core, is entered.

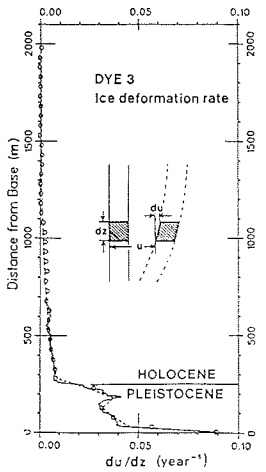

Fig. 5.15 Horizontal shear strain rate in the Dye 3 borehole, calculated from inclination measurements. A rapid increase is observed at the Holocene-Wisconsin transition. From Dahl-Jensen & Gundestrup (1987), modified.

Fisher & Koerner (1986) concluded that the rapid deformation of ice age ice in the Agassiz ice cap was best related to impurity content and that fabric changes were not responsible. Similarly, Dahl-Jensen & Gundestrup (1987) concluded that the enhanced flow of the Wisconsin ice at Dye 3 was mainly due to the high concentration of dust or soluble impurities and/or to the small grain size. Shoji & Langway (1988), on the other hand, concluded from mechanical tests on Dye 3 core samples, that the softening effect in the Wisconsin ice, under conditions of shearing, was mainly due to the strong single maximum fabric of this ice. Pimienta et al. (1988) performed mechanical tests on samples from different climatic periods in the Vostok core, with widely varying impurity content. They found little difference in viscosity between the samples and thus concluded that impurities did not influence the mechanical behaviour of Vostok ice.

Paterson (1991) has reviewed the available data on the subject of the "soft" ice age ice. He concludes that the strengthening of the fabric to a strong single maximum, observed to occur across the Holocene-Wisconsin transitions in the Byrd, Camp Century and Dye 3 cores, is the cause of the enhanced rates of horizontal shearing in the ice age ice. He further concludes that soluble impurities (mainly chloride and sulphate) and small grain size also play a role, in that the impurities impede grain growth in the Wisconsin ice, and that the small grains more easily develop a strong single maximum fabric than larger ones, which favours further shear deformation. The deformation, in turn, contributes to to keeping the crystals small by increasing the rate of polygonization.

The Holocene-Wisconsin transition in the GRIP core

Several lines of evidence indicate that the Wisconsin ice at Summit does not flow more readily than the Holocene ice above. Firstly, the transition occurs at a depth of 54% of the total ice thickness, where horizontal shearing is probably still negligible. The corresponding depths are 84% and 88% of the total ice thickness at Camp Century and Dye 3, respectively. Secondly, the ice divide position ensures that horizontal movement is very low at Summit, as shown by surface velocity and borehole inclination measurements to date (Chapter 3). The Camp Century and Dye 3 sites are, on the other hand, located in flank flow regimes, off the ice divide. Thirdly, the data obtained on the core and presented in Fig. 5.16 clearly show that a significant fabric strengthening hardly occurs across the Holocene-Wisconsin transition. The two fabrics measured 5.5 m and 2.2 m above and below the transition, respectively, both display broad single maximum fabrics with similar appearances, and although the Wisconsin fabric has a higher degree of orientation than the Holocene fabric, it is weaker than the fabric at 1569.2 m. It is also evident from Fig. 4.3, that there is no sharp strengthening of fabrics as the Wisconsin ice is entered, but rather a continuation of a downward trend.

Crystal size decreases from 3.8 mm to 2.9 mm at the transition but this decrease is of a smaller magnitude than at the other Greenland sites. At Dye 3, crystal size drops from 5 mm to 2 mm at the transition (Herron et al, 1985). Since the increase in impurity content at the two sites is comparable, this difference might indicate an effect of the strong shearing below the transition in the Dye 3 core on the crystal size, in addition to the drag-effects of impurities.

Results from ultrasonic velocity measurements on the GISP2 core do not indicate a significant fabric strengthening at the Holocene-Wisconsin transition in this core either (Anandakrishnan et al., 1994). "Soft" ice age ice is thus not expected under the stress conditions prevailing at Summit. It is clear, however, that the lower part of the Wisconsin ice, which is rather fine grained and displays a strong fabric, would be "soft" if it were subjected to strong shearing.

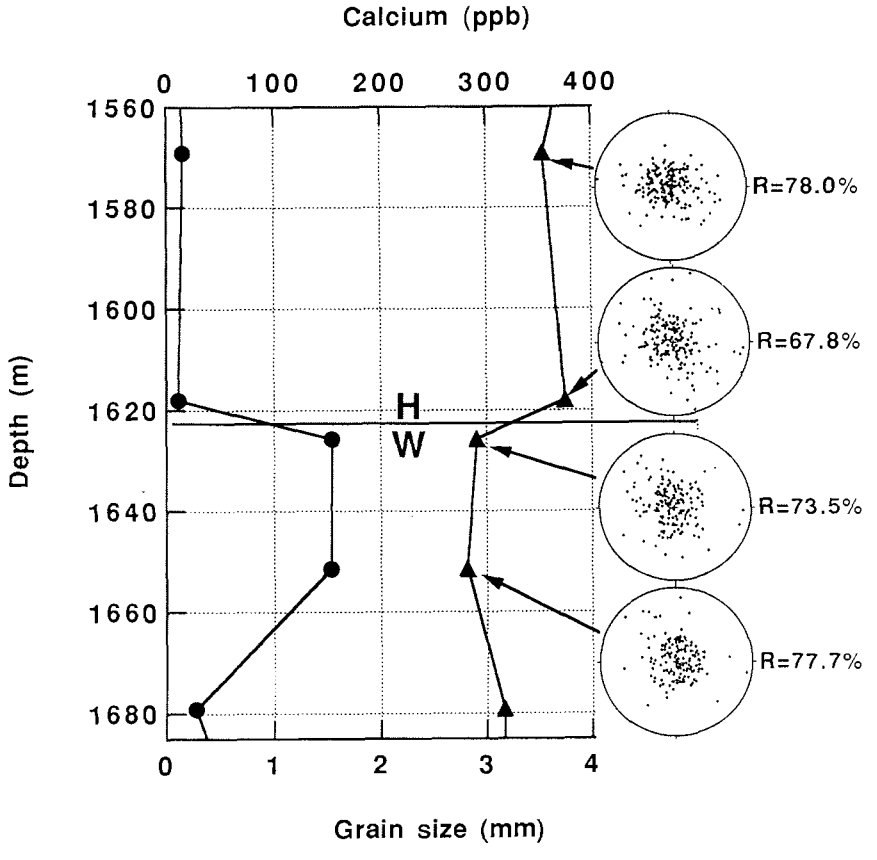

Fig. 5.16 Crystal size (triangles), calcium (circles) and crystal fabric changes across the Holocene-Wisconsin transition in the GRIP core, which occurs at 1623.6 m depth (Johnsen et al., 1992). The Degree of orientation (R) for each fabric is indicated.

Rheological contrasts in the lowest 250 m

Fabrics No. 27 and 28 in Fig. 4.2 are cut 10 m above and 5.6 m below the Wisconsin-Eemian transition, respectively. The horizontal crystal size in the Wisconsin thin section is 4.1 mm, and its degree of orientation is R = 91.9%; a typical value for strong single maximum fabrics. In the Eemian section, crystal size has increased to 8.8 mm and R has decreased to 79.3%. Clearly, the fabric weakens as the more coarse grained Eemian ice is entered. A re-strengthening occurs in the fine-grained ice of Stage 5e2 (No. 29; 2806.65 m), but the stretched fabric at 2861.65 m (No. 30) is obtained on coarse grained ice. Below the transition into fine grained ice below 2865 m, which probably is of Saalean origin, a strong single maximum reappears (No. 31; 2889.15 m), although some axes lie outside the central maximum.

Taking a closer look at one of the rapid cold events in the Eemian sequence, Fig. 5.17 shows fabrics measured above, below and within Event 1. Crystal sizes are indicated (see also Fig. 5.6), and it seems clear that the fabric strengthens in the fine-grained ice within the Event.

It thus appears that fabric strength is related to grain size in the interval 2780-2900 m, with the fine grained ice retaining the strong single maximum whereas the coarse grained ice displays weaker fabrics. The conclusions of Paterson (1991), mentioned above, could be invoked to explain this variation in fabric strength, since impurity content is inversely correlated with grain size in this interval. Alternatively, the weak fabrics of the coarse grained ice could be explained by recrystallization processes, which would cause this ice to lose its previously attained fabric.

The rapid variations in textures and fabrics in the lowest 250 m of the core are likely to cause significant variation in flow properties. Fine grained ice with a strongly preferred fabric will most likely be soft in shear but hard in vertical compression. As stated by Alley (1992), much less clarity exists regarding the flow properties of coarse grained ice, but it seems very unlikely that such ice can form under conditions of rapid deformation. Budd & Jacka (1989) discussed the possibility that coarse grained ice found at the base of ice sheets (e.g. at Byrd Station) formed by annealing at relatively high temperatures, under conditions of reduced stress due to variation in bedrock topography. Such ice would be nearly stagnant, undergoing extensive crystal growth and the formation of recrystallization fabrics. If this applies to the formation of coarse grained ice at Summit, it appears that the "warm" layers in the Eemian ice represent rather stiff, coarse grained layers sandwiched between fine grained layers from cold periods, capable of deforming more rapidly under conditions of shearing. In particular, the "Saalean" layer between 2865 m and 2915 m can be expected to have undergone shear deformation, as will be discussed further in a later chapter. Future inclination surveys in the borehole will probably reveal higher deformation rates in this

part of the hole than at any other depth. Little deformation is expected in the lowest 100 m of the ice sheet, which is very coarse grained.

How the variations in flow properties will influence the layer-thinning process in the ice is likely to depend on the dominating stress system. If vertical compression dominates, the fine-grained layers with a strong fabric will be harder and thin more slowly than the coarse-grained layers with a weaker fabric. If, on the other hand, simple-shear dominates, the fine-grained layers will undergo more rapid shearing and thinning. Although vertical compression appears to dominate at present, stratigraphic studies have revealed the presence of simple-shear features in the lowest part of the core (Chapter 6). This ice thus appears to have gone through a complex deformation history, perhaps alternating between different stress states as the ice divide migrated.

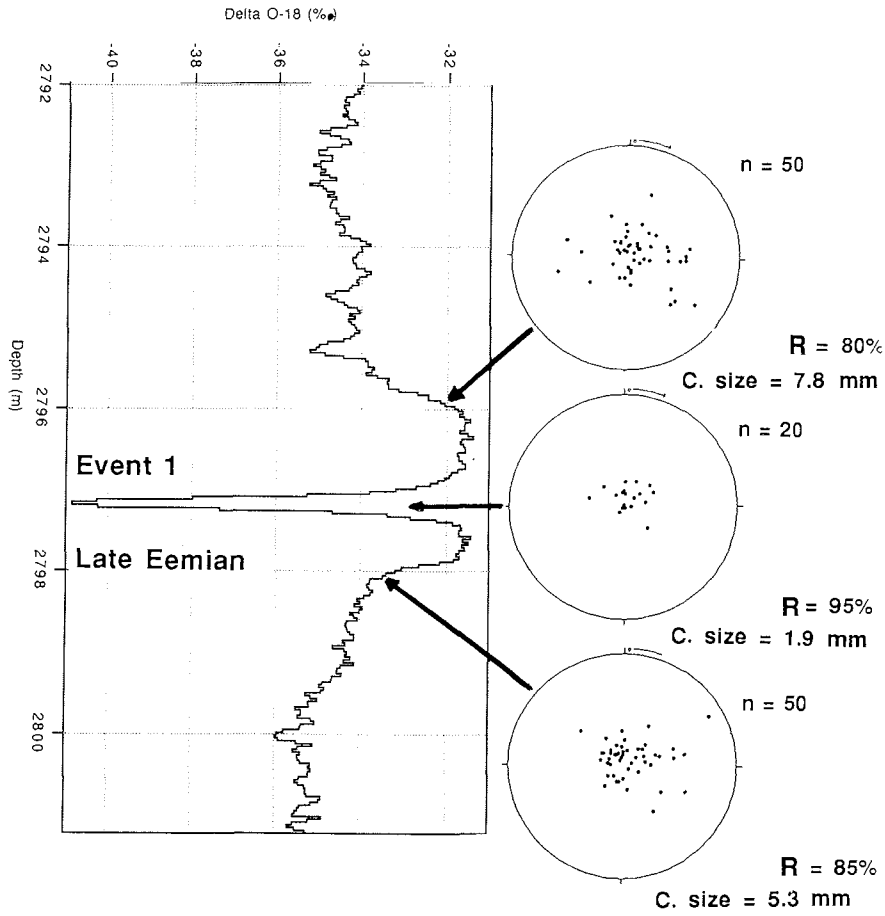

Fig. 5.17 Fabric diagrams from Event 1 and surrounding ice. The middle diagram results from c-axis measurements on small crystals at the height of the event (2797.08-2797.19 m), the other two from more coarse grained ice above and below. Crystal size (d) and Degree of orientation (R) are indicated.

Variation in geometric softness

As discussed in Chapter 2.4, a crystal subjected to uniaxial compression will have resolved shear stress acting on its basal plane, proportional to the geometric factor (Schmid factor) $S = \cos\varphi\sin\varphi$, where φ is the angle between the c-axis and the axis of compression (Fig. 2.24). The average Schmid factor for an ice sample of N crystals; $\Sigma\cos\varphi_i\sin\varphi_i/N$, is a measure of the softness of the sample under uniaxial compression. The variation of this factor between 100 and 2800 m depth in the GRIP core, determined from the fabric data, is shown in Fig. 5.18.

The softness increases down to 800 m depth, where vertical strain reaches 30%. This initial increase is due to the decrease of the median value of φ from 60° (for random orientations) to 45°; the position of maximum resolved shear stress (Alley, 1988). Below 800 m, the softness parameter decreases steadily as the fabric strengthens. In the strong single maximum region below 2500 m, vertical strain exceeds 90% and the softness parameter has been halved in comparison with the ice between 500 and 1000 m. As discussed in the following section, this hardening with depth is clearly evident in results from uniaxial compression tests carried out on samples from the GRIP core.

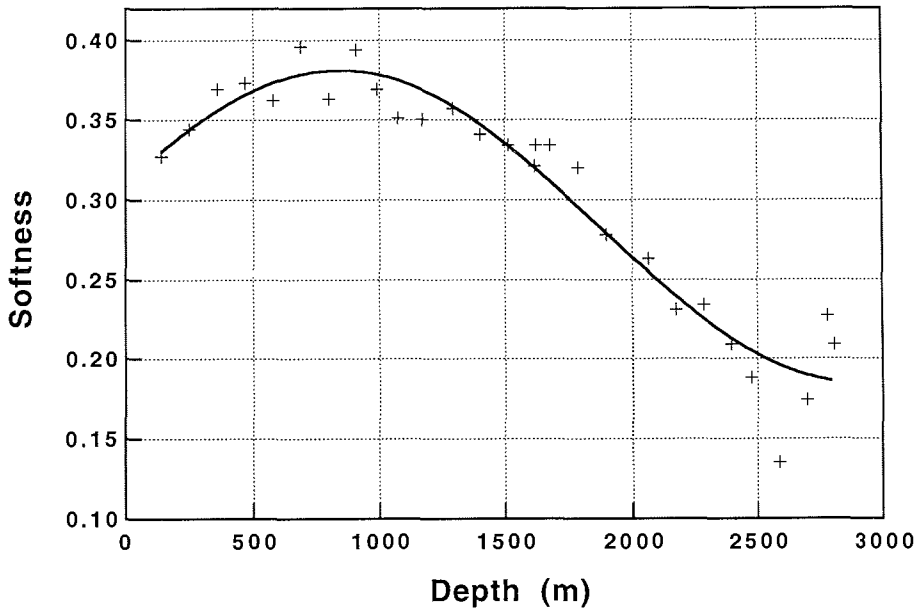

Fig. 5.18 Variation of the average geometric Schmid factor in the upper 2800 m of the GRIP core.

Deformation tests on GRIP core samples

At the University of Copenhagen, deformation tests have been carried out on samples from the GRIP core since April 1993 (Dahl-Jensen et al., in press). Cylindrical specimens, 5 cm in length and 2.5 cm in diameter, have been deformed in unconfined uniaxial compression under a constant octahedral stress* of 3.0 bars, at a temperature of -16 °C. The samples have been cut from the Holocene, Wisconsin, Eemian and Pre-Eemian periods and thus show a considerable variation in crystal size, fabric and impurity content. This study can therefore be expected to yield valuable information on the effect of these factors on the rheological properties of polar ice.

Crystal size and c-axis orientations have been measured on the samples before and after the tests, by the author of this work. The discussion below focusses on the effects of these parameters on the initial deformation of the samples, and on the changes in crystal size and fabric during deformation.

Creep curves from four tests are shown in Fig. 5.19 (reproduced by permission of D. Dahl-Jensen). Samples No. 1 and 2 are from 550 m and 1435 m depths in the Holocene ice, respectively, No. 3 (2095 m) is from a warm interstadial in the Wisconsin ice and No. 4 (2107 m) from an adjacent cold stadial period. The results are shown as both strain vs. time and strain rate vs. strain. Initial fabrics of these samples are shown to the left in Fig. 5.20 (No. 1-4). They seem typical for these depths; the fabric is nearly random in No. 1, has started contracting in No. 2 and a single maximum has formed in No. 3 and 4. The initial crystal sizes are also indicated.

The typical creep-curve pattern described in Section 2.2 is observed in these tests: Primary, decelerating creep to 1-2% strain, then a transition through secondary, minimum creep rate (absent in No. 2 and 4) to a fairly steady, tertiary creep rate.

It appears clear that the initial c-axis fabric exerts a marked influence on the initial rate of deformation. After 3000 hours, the weakly oriented samples 1 and 2 have reached about 13% strain whereas the strongly oriented samples have both reached less than 3% strain. A similar conclusion is reached if the comparison is restricted to primary creep only (up to 1% strain), during which the fabric is unlikely to undergo a major change: Samples 1 and 2 reach 1% strain after 100-150 hours whereas samples 3 and 4 reach 1% strain after 3-400 hours. Clearly, the strong single maximum fabrics make the ice hard in vertical compression. Initial crystal sizes in the four samples are similar and the small differences are unlikely to have a significant effect on the rate of deformation. The Holocene samples have lower impurity content and their more rapid deformation in compression is thus clearly not due to any softening effect of impurities. In this respect, comparison of the two Wisconsin samples

* For a definition of octahedral stress see Lile (1978).

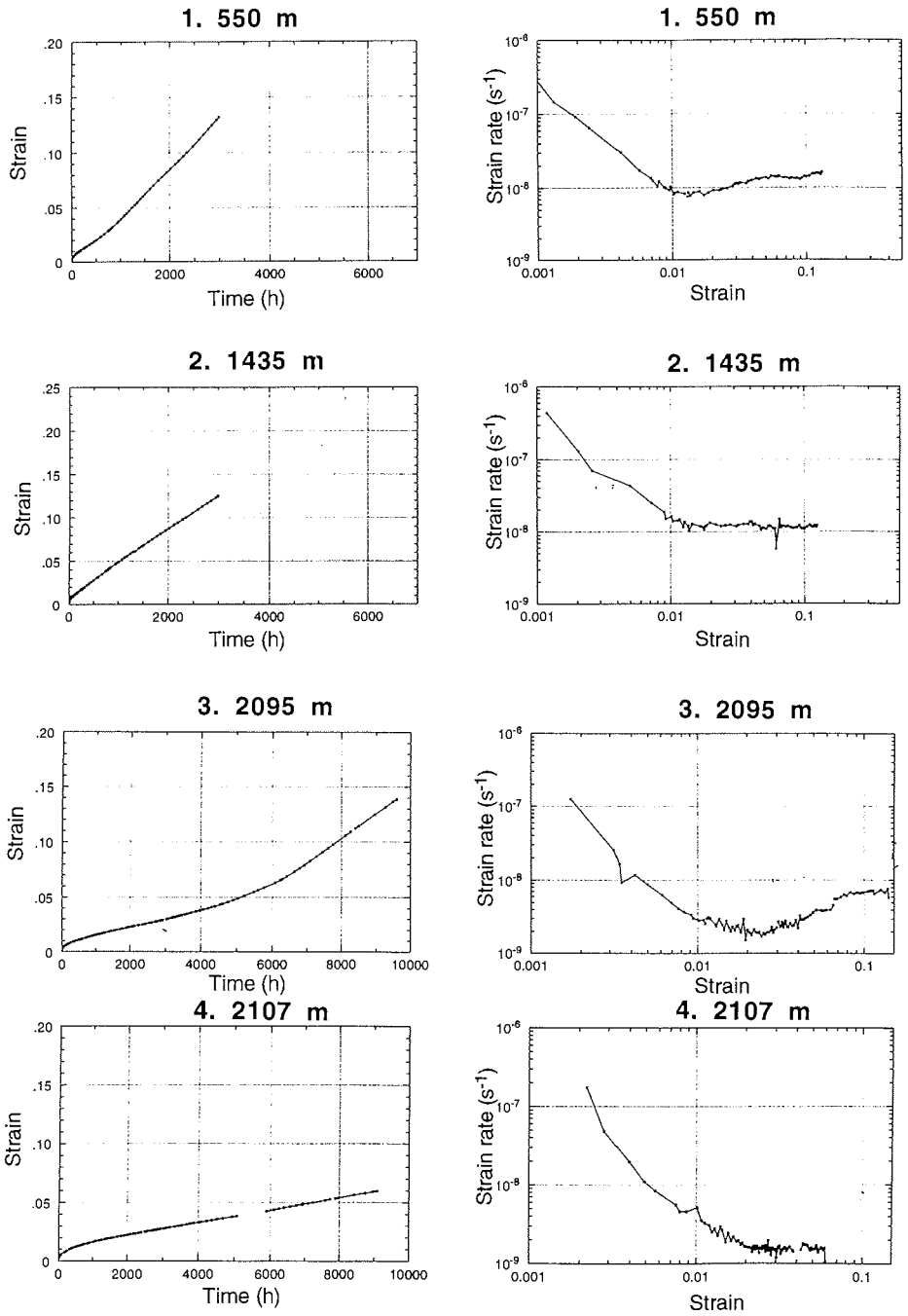

Fig. 5.19 - Creep curves for four GRIP samples, deformed in uniaxial compression. Left: Strain vs. time. Right: Strain rate vs. strain. Reproduced by permission of D. Dahl-Jensen.

is also of interest. They have similar crystal sizes and fabric strengths in the beginning, but No. 4 has 60 times higher dust content than No. 3 (Dahl-Jensen, personal communication). Nevertheless their initial deformation rate is similar (first 3000 hours), again indicating that the higher impurity content has no softening effect in vertical compression.

Fabrics and crystal sizes of the samples after deformation are shown to the right in Fig. 5.20. The crystal size has increased in samples No.1-3, indicating that recrystallization has taken place. Since the thin sections from the deformed samples are small and thus contain few crystals, statistically reliable determination of the c-axis orientations is not possible. Nevertheless, the fabrics of the deformed samples indicate that the formation of a circular girdle, centered on the compression axis, is taking place during the tests.

Other tests give further evidence of recrystallization during defomation of the samples, as indicated by fabrics No. 5 and 6 in Fig. 5.20. An initially coarse grained Eemian sample from 2812 m depth has after the test been reduced in grain size from 16.0 mm to 5.6 mm and a girdle fabric has formed. A sample from 2954 m depth, from a region of disturbed stratigraphy, initially has a single maximum offset from the center of the fabric diagram. Its crystal size decreases during deformation and here it is very clear that a recrystallization girdle has formed.

To further check the change in c-axis orientation during the deformation tests, the percentage of c-axes between 20° and 45° from the axis of vertical compression, before and after tests, has been calculated. This interval is chosen since recrystallization probably produces crystals with c-axes initially at ≈45°, which then rotate towards the vertical (Alley, 1992). An increased percentage of crystals in this interval is thus expected. Also, the average Schmid factor S (see previous section) has been calculated for each measured sample. The Schmid factor is a measure of the softness of the sample in compression and has a maximum of 0.5 for 45°, when the resolved shear stress along the basal planes reaches a maximum.

The results are presented in Table 5.3. With two exceptions (No. 1 during 3rd test and No. 6 during 1st test, here clearly due to few crystals in start), there is a clear tendency in these results: The majority of the c-axes concentrates in the interval between 20° and 45° as the tests proceed, and the softness of the samples against compression increases. The assertion that the increased creep rate in tertiary creep is due to recrystallization, producing grains more favourably oriented for basal glide, is thus strongly supported by these results. The fact that girdle fabrics form during the deformation tests, but are not observed in the ice sheet, can probably be explained by the much higher strain rates experienced by the ice in the tests than in the ice sheet.

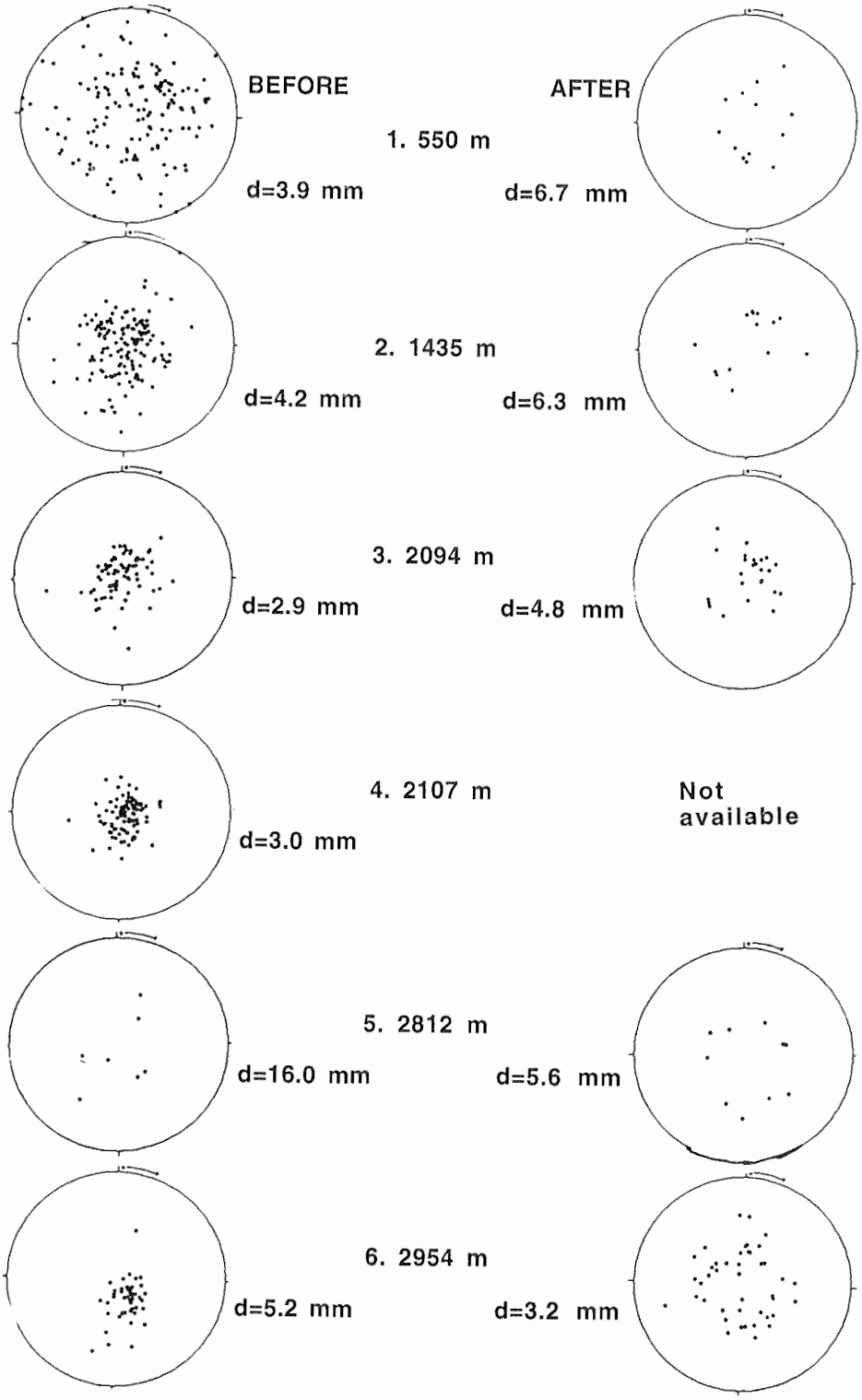
BEFORE
AFTER
1. 550 m
d=3.9 mm
d=6.7 mm
2. 1435 m
d=4.2 mm
d=6.3 mm
3. 2094 m
d=2.9 mm
d=4.8 mm
4. 2107 m
Not available
d=3.0 mm
5. 2812 m
d=16.0 mm
d=5.6 mm
6. 2954 m
d=5.2 mm
d=3.2 mm

TABLE 5.3 - FABRIC CHANGES DURING COPENHAGEN TESTS

Sample	Status	% of c-axes in [20°,45°]	Schmid factor
1. 550 m	Before tests	48 %	0.39
- -	After 1. test	60 %	0.41
- -	After 2. test	94 %	0.44
- -	After 3. test	85 %	0.40
2. 1435 m	Before tests	51 %	0.33
- -	After 1. test	72 %	0.41
- -	After 2. test	86 %	0.42
3. 2094 m	Before tests	36 %	0.27
- -	After 1. test	50 %	0.34
4. 2107 m	Before tests	28 %	0.24
5. 2757 m	Before tests	45 %	0.29
- -	After 1. test	64 %	0.42
6. 2812 m	Before tests	71 % (n=7)	0.41
- -	After 1. test	50 %	0.41
- -	After 2. test	80 %	0.45
7. 2953.7 m	Before tests	43 %	0.42
- -	After 1. test	65 %	0.43
- -	After 2. test	100 %	0.47
8. 2954 m	Before tests	46 %	0.32
- -	After 1.test	86 %	0.41

Most samples have been compressed more than once. Strain reaches 10-20% in each test.

TABLE 5.4 - FLOW LAW PARAMETERS IN GRENOBLE TESTS (from Milsch, 1994)

SAMPLE	A/A_O	R (%)
Artificial isotropic	1.00	0-20 %
GRIP - 1328 m	0.80	65 %
GRIP - 1768 m	0.42	75 %
GRIP - 1988 m	0.31	85 %
GRIP - 2208 m	0.18	92 %
GRIP - 2318 m	0.11	92 %
GRIP - 2544 m	0.16	93 %
GRIP - 2703 m	0.17	93 %

Uniaxial compression tests on GRIP samples have also been carried out at the Laboratoire de Glaciologie in Grenoble, by H. Milsch & P. Duval (Milsch, 1994). Holocene and Wisconsin samples of different fabric strength have been tested and the results are similar to those obtained in the Copenhagen studies; i.e. a hardening of the samples against vertical compression with increased fabric strength. For the minimum (secondary) strain rate in each of the tests, Milsch (1994) calculated the flow law parameter A in Glen´s law (Eq. 2.13), which for the special case of uniaxial compression can be shown to have the form $\dot{\varepsilon}_z = \frac{2}{9} A \sigma_z^3$. A flow law exponent of n=3 (Paterson, 1994; p. 92) was assumed. The results, expressed in the form A/A_o, where A_o is the flow law parameter obtained for an isotropic sample, are shown in Table 5.4. The hardening with increasing anisotropy is evident from these data. The hardest sample displays a A/A_o ratio of 0.11; i.e. it deforms an order of magnitude more slowly in secondary creep than the isotropic sample.

The results presented in this chapter demonstrate that the ice hardens against vertical compression as the strong single maximum fabric develops. This hardening would be expected to slow the thinning of annual layers in the ice sheet. According to data from the GRIP core, annual layers thin steadily from >20 cm near the surface to 2-3 cm at 1850 m depth (Dahl-Jensen et al., 1993). However, according to sparse data between 1850 m and 2250 m, annual layer thickness is nearly constant in this interval. This is likely to result from the hardening of the ice, since the single maximum has formed by this depth.

6. STRATIGRAPHIC STUDIES

After publication of the isotopic and electrical conductivity climate records from the GISP2 core, and detailed comparison with the corresponding GRIP results (Grootes et al, 1993; Taylor et al., 1993), it became clear that the two records matched each other very well down to a depth of about 2750 m (≈100 kyr BP) but disagreed seriously below this level. Most importantly, the "Eemian" as reported from the GRIP core (GRIP Members, 1993), was not confirmed by the GISP2 record. As shown in Fig. 6.1, high, "Eemian-like" $\delta^{18}O$-values are found in the interval 2840-2850 m in the GISP2 core. Then follows a 100 m increment of low, Wisconsin-like $\delta^{18}O$-values, with the interval 2900-2950 m resembling the "Saalean" interval (2865-2910 m) in the GRIP core. Between 2950 and 3000 m (GISP2), high $\delta^{18}O$-values, oscillating with low ones, occur. The major differences between the cores indicate that either one of the records, or both, must have undergone serious flow disturbances due to irregular bedrock topography.

Several studies have been initiated to try to resolve this problem (e.g. Bender et al., 1994; Johnsen et al., 1995b; Fuchs & Leuenberger, in press), including an intercomparison of stratigraphic features in both cores (Alley et al., 1995b). In this chapter, major results from studies of stratigraphic disturbances in the GRIP core, and their effect on crystal fabrics, will be presented and discussed.

Visual stratigraphy

In the Holocene ice, summer-winter variations in bubble and grain sizes, which affect light transmission and reflection, can be used for annual-layer counting (Meese et al., 1994, Alley et al., in press). In the Wisconsin ice and earlier periods, visible cloudy bands, shown in Fig. 6.2, are the most important stratigraphic tool (Kipfstuhl & Thorsteinsson, 1993). These are layers varying in thickness from < 1 mm to a few cm, with high concentrations of microscopic inclusions scattering light. The exact nature of these inclusions has not been determined, but one possibility is that they consist of microbubbles, which form around microparticles after core retrieval. In general, the occurrence of cloudy bands correlates with high dust content in the core. The intensity of the bands varies with climate, more bands being observed in ice dating from cold periods. Ice from warm periods is normally clear immediately after retrieval, but layering can become discernible in this ice too, as the core relaxes in storage.

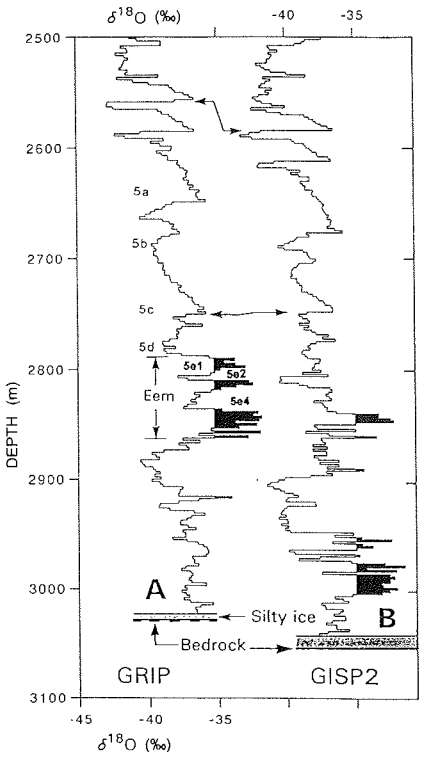

Fig. 6.1 - The $\delta^{18}O$ profiles from below 2500 m depth in the GRIP and GISP2 ice cores. Marine Isotope Stages (MIS) 5a-5e, as originally identified in the GRIP core, are indicated. $\delta^{18}O$ values which are higher than at present are set out in black. The records match very well down to 2680 m at GRIP (2700 m GISP2) but disagree seriously below 2750 m depth. - From Johnsen et al. (1995).

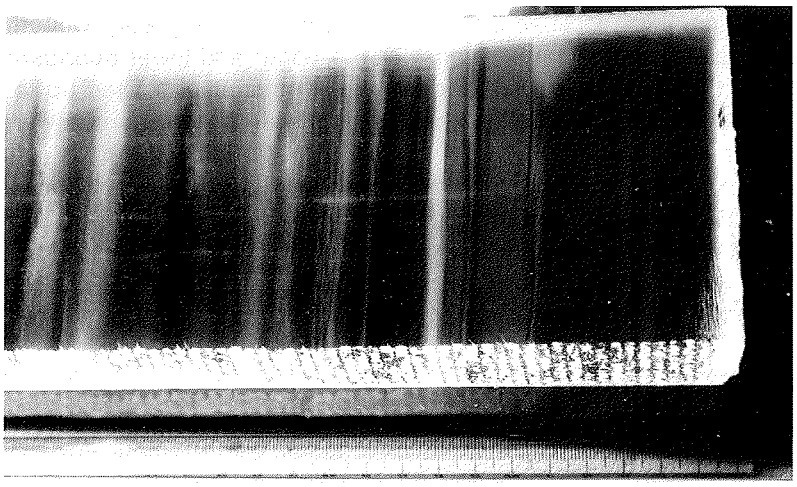

Fig. 6.2 - Cloudy band layering in the Wisconsin ice. The width of the core is 10 cm.

A systematic study of the cloudy band stratigraphy in the GRIP core was carried out by J. Kipfstuhl during the field season 1992, covering the interval 2300-3029 m. S.J. Johnsen studied layer inclinations in selected parts of the Eemian ice in the storage facility in Copenhagen (Johnsen et al., 1995b), and the stratigraphy in the lowest 300 m was further scrutinized during a Joint GRIP-GISP2 intercomparison study of the flow disturbances in both cores, carried out in Copenhagen and Denver in 1994. Major results of this comparative study have been reported by GRIP and GISP2 researchers (Alley et al., 1995b). Below, the combined results of those different studies on the GRIP core are outlined.

2300-2790 m: Lower Wisconsin, including MIS 5a-5d.

The cloudy bands are mostly undistorted in this interval, although slight wavyness of the banding can occasionally be observed and a single microfold has been detected at 2483 m. The bands are either horizontal or display low inclinations, up to 6° (consistent with a hole inclination of 3° and a bedrock slope of 3°). The only exception from this regular layer structure is in a 1 m interval at 2757 m depth, where layers dip 10° or more, and reach an inclination of 20° in a 10-20 cm increment (Fig. 6.3). Layering returns to near-horizontal below this disturbance, which coincides approximately with the level where the climate records from the two cores start to differ. The uppermost disturbance of a similar magnitude at GISP2 was found at 2679 m depth in this core (Alley et al., 1995b).

2790-2865 m: The Eemian ice.

The stratigraphic studies have not revealed any unusual features in the upper 3/4 of the Eemian, down to a depth of 2847 m. Event 1 is visible as a cloudy layer, 20 cm thick, inclined 5-6° from the horizontal (Fig. 6.4). Distortion is not evident, apart from slight wavyness at the upper and lower boundaries of this layer. In the cold stages 5e2 and 5e4 layering is also inclined up to 5-6°. No cloudy bands or other stratigraphic features are observed in the warm stages 5e1, 5e3 and 5e5.
At 2847 m depth, in one of the cold events of Stage 5e5, highly inclined layers (up to 17°) appear. Within Event 2, inclination does not exceed 8°, but distorted layering is observed at the upper and lower margins of the event, as well as within it (Fig. 6.5). Clearly, the lowest 1/4 of the Eemian has been affected by significant layer disturbances.

2865-3022 m: Lowest 160 m.

Between 2865m and 2900 m, several small disturbances are evident and layer inclinations vary between 0° and 20°. In the interval 2900-2950 m, layering is considerably distorted; an example is shown in Fig. 6.13. Little distortion has been found in the interval 2950-3022 m, but this stems perhaps

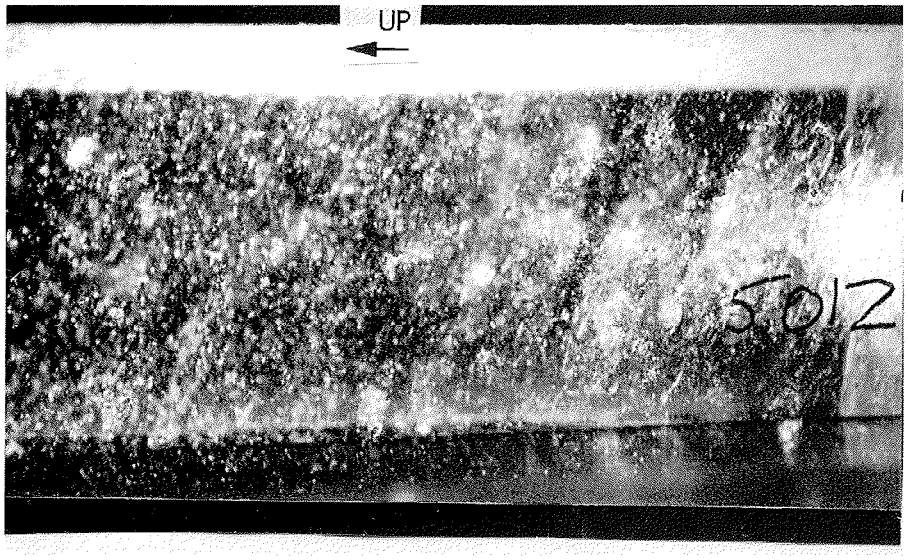

Fig. 6.3 - Disturbed layering at 2757 m depth. Maximum inclination of the layers from the horizontal is 20°.

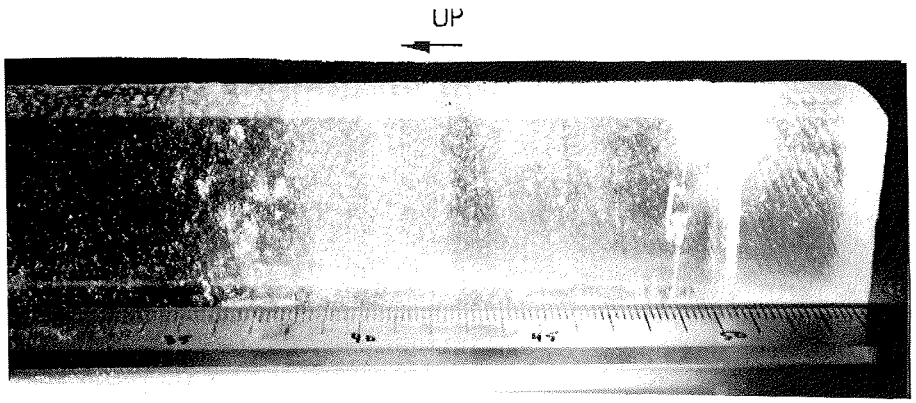

Fig. 6.4 - Catastrophic Event 1 at 2797 m depth, visible in the core as a 20 cm thick, cloudy layer.

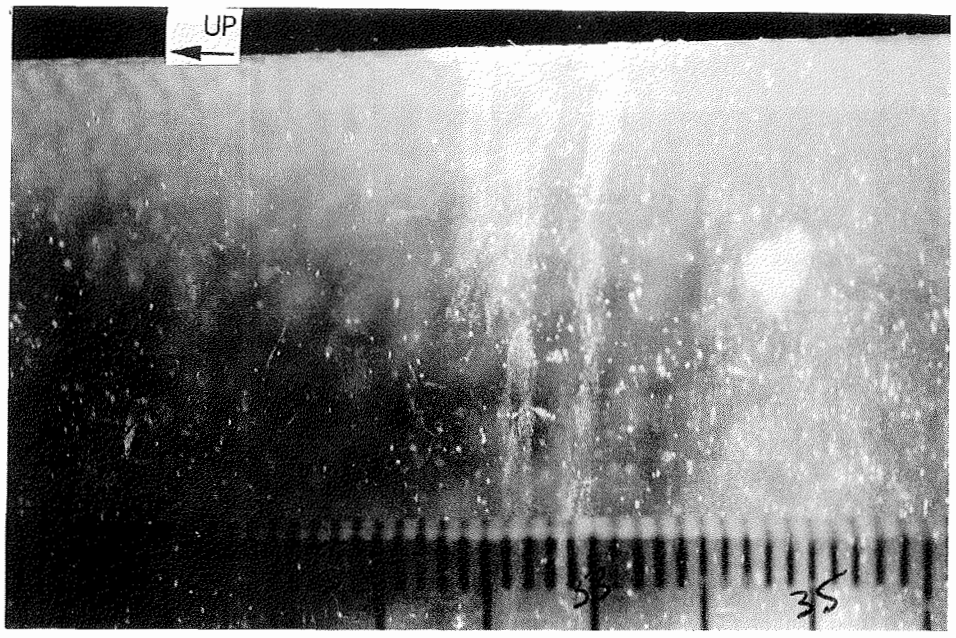

Fig. 6.5 a) - Distorted layering at the upper margin of Event 2. The disturbance appears to be an overturned fold.

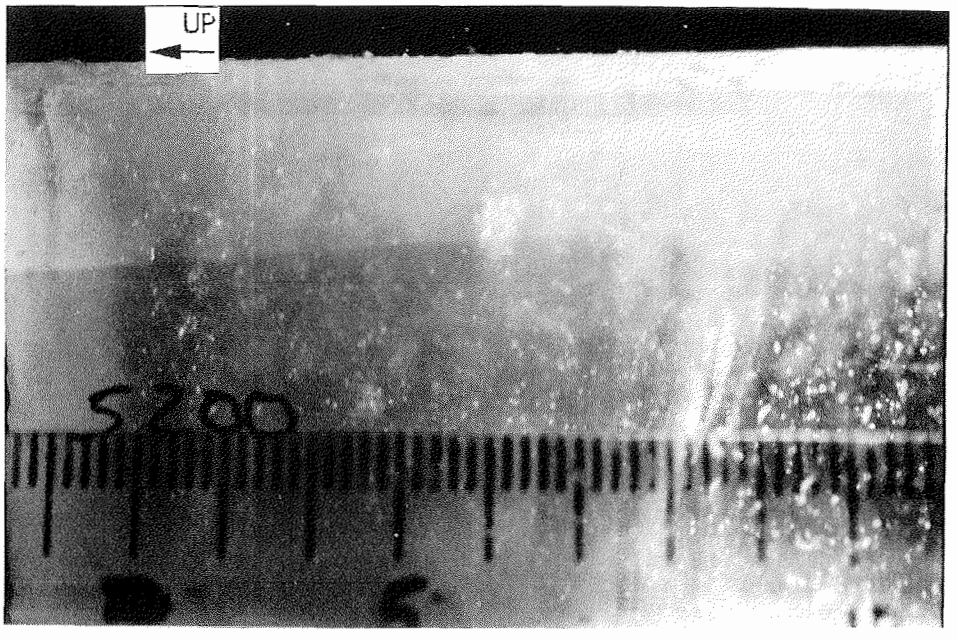

Fig. 6.5 b) - Layer distortion at the lower margin of Event 2.

from the fact that much of this ice is clear and no layering is visible. The distortions are mainly observed at junctions between cloudy and clear ice. Thus, the possibility that disturbances are present in this interval should not be excluded.

The GISP2 core.

According to Taylor et al. (1993), wave-like distortion of the cloudy bands occurs as high as at 2200 m depth in the GISP2 core, and the shallowest overturned fold detected, with a vertical displacement of 1 cm, occurs at 2400 m. Layers inclined 20° are observed in a 50 cm increment at 2679 m depth and also in a region several meters long around 2809 m (Alley et al., 1995b). These disturbances are considerably higher up in the core than the first occurrence of high $\delta^{18}O$-values below the Wisconsin ice (2840 m). Due to the disturbances, the isotopic record from below 2700 m depth in the GISP2 core has not been interpreted in terms of climatic variation (Grootes et al., 1993).

Origin of the disturbances

The two mechanisms outlined below have been suggested as a cause of the disturbed stratigraphy in the two cores:

Boudinage. This term refers to the distortion of a layer embedded in a material of the same density as the layer but with lower viscosity. Under stress, the more competent (harder) layer will deform less readily than the surrounding material and can thus become deformed into pinch-and-swell structures or pulled apart to form so-called boudins (Fig. 6.6). This phenomenon is common in geological materials (e.g. Ghosh, 1993). Gow (1972) has reported the occurrence of boudin-like structures in Antarctic glacial ice and Hambrey & Milnes (1975) described observations of boudinage in the margins of glaciers in the Swiss Alps. Staffelbach et al. (1988) discussed whether this phenomenon could have produced rapid variations in climatic parameters in the Wisconsin ice at Dye 3, variations which now have been shown to correlate with the Dansgaard-Oeschger events in the GRIP core and other records (Johnsen et al., 1992). Cunningham & Waddington (1990) applied the theory of Smith (1975, 1977) to the (modelled) layer of Eemian ice in Central Greenland (prior to the deep drillings), and found that this layer could be expected to have undergone considerable distortion due to boudinage.

The boudinage phenomenon distorts the relative thicknesses of adjacent layers but leaves them in stratigraphic order. The effect on the time-scale in an ice core would thus be to stretch some sections and contract other ones.

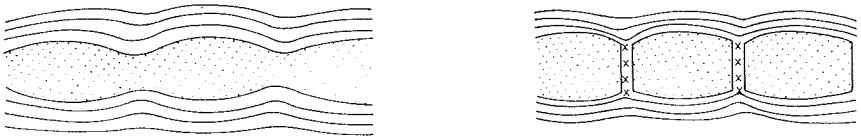

Fig. 6.6 - Left: Pinch-and swell structures. Right: Extension fracture boudinage. - From Ghosh (1993).

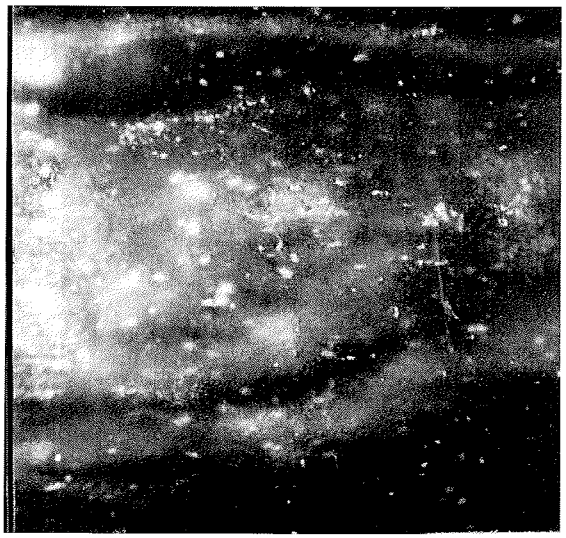

Fig. 6.7 - Thickness variation in a cloudy band. The maximum thickness of the layer is 2 cm.

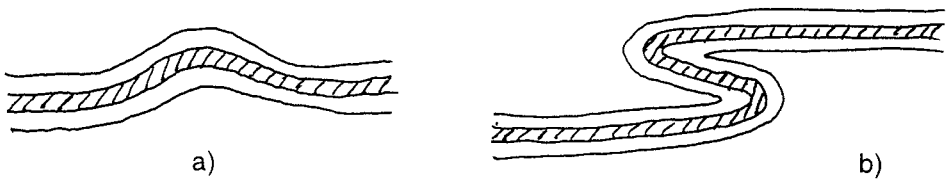

Fig. 6.8 - **a**) Open fold, **b**) overturned fold. A core drilled through an overturned fold will encounter the same layer more than once.

The classical model of boudinage applied by Cunningham & Waddington (1990) assumes that the layer being deformed into boudins is harder than the surrounding material in pure shear. This would apply to the cloudy bands, which are more fine grained than the surrounding ice, have developed a stronger fabric and consequently are harder in compression. Observations of the cloudy band stratigraphy and of the disturbed features have, however, revealed no direct evidence of boudinage phenomena. Clearly, the small cross section of the core prevents the detection of boudins which are significantly larger than the core diameter. Occasionally, cloudy bands are seen to vary in thickness across the core, as shown in Fig. 6.7, but whether this can be interpreted as boudinage is unclear. Small, overturned folds displaying an opposite sense of shear, which can form on the upper and lower margins of boudins (R.B. Alley, personal communication), have not been detected.

If the isotopically cold intervals in the GRIP Eemian ice do not represent real climatic fluctuations but have somehow been inserted into an original, undisturbed sequence of isotopically warm ice, it seems very unlikely that this can be due to boudinage. The phenomenon can distort the timescale, but does not lead to intermixing of layers from different depths. In addition, the fabric weakens in the warm Eemian ice and this ice is thus expected to be softer in pure shear than the ice above and below, contrary to the assumption of Cunningham & Waddington (1990).

Folding. Folds are commonly observed in glacier margins (e.g. Post, 1972; Hudleston, 1976), but very little is of course known of folding in the interior regions of large ice sheets. In a modelling study, Whillans & Jezek (1987) found that large-scale (wavelength of a few km) folding could arise from flow over irregular bedrock topography in the Dye 3 area. In case of overturned folding (Fig. 6.8), the layering in the ice will no longer be in chronological order and the same layer can be encountered more than once in an ice core drilled vertically through such a disturbance. This will introduce serious errors into the climatic record.

It is clear that small-scale folding has occurred at the base of the ice sheet at Summit. Both open folds and overturned folds, of dimensions from a few mm to 10 cm are abundant between 2850 and 2950 m depth, but whether the borehole has penetrated through larger folds cannot be determined. No method exists which can distinguish overturned layers from those which are in undisturbed, horizontal position. Since an overturned layer would have been penetrated 2-3 times by the core, attempts have been made to identify two or more layers with identical isotopic and impurity concentrations (J. Schwander, personal communication). The results do not indicate the presence of repeated layering. Large-scale folding in the Summit area seems unlikely, since the bedrock topography of the region does not display major irregularities (Hempel & Thyssen, 1993). It should also be kept in mind, that

the isotope record in the Dye 3 core (Dansgaard et al., 1982) is preserved down to 80 m above the bottom, even though the bedrock topography is much more rough than at Summit.

Returning to a comparison of the GRIP and GISP2 cores, the initial speculation was that GRIP, being at present in a pure shear flow regime, would experience boudinage distortion of layers, whereas overturned folding was more likely in the simple shear regime expected at the GISP2 site (Taylor et al., 1993). However, the presence of overturned folds in the GRIP core clearly indicates that simple shear is, or has recently been, active at the GRIP site too, suggesting that a displacement of the ice divide has occurred. In a modelling study, Anandakrishnan et al. (1994) found that divide migration of between 10 km and 50 km was likely to take place on glacial-interglacial timescales, indicating that the GRIP site could have experienced flank flow during at least part of the Wisconsin period.

The fact that the first serious layer disturbance in the GRIP core occurs above the Eemian (highly inclined layering at 2757 m), clearly poses a problem for the climatic interpretation of this period (GRIP Members, 1993). If the rapid variations between high and low isotope values have resulted from folding or some other large scale disturbance, it seems all the more surprising that significant flow disturbances have not been detected at the boundaries of the different Eemian stages, except for the lower part of stage 5e5. Furthermore, the first presence of highly inclined layering is not necessarily an indication that the whole stratigraphy below is disturbed, since highly inclined layering occurs at 2679 m in the GISP2 core, 70-80 m above the level where serious discrepancies between the two cores show up.

Effects on fabrics

Thin sections have been made from ice samples cut across several of the observed flow disturbances, to examine their effect on the ice fabric. A few examples are discussed below.

1. Highly inclined layering at 2757 m - Fig. 6.9: From the thin section photograph it is clear that the individual grains are in inclined positions, compatible with the 20° inclination of the layering. The single maximum fabric is also clearly offset from the center of the diagram and, indeed, the calculated average c-axis is inclined 20° from the vertical.

2. Wavy layer at 2869.5 m - Fig. 6.10: The interesting feature here is the stripe of crystals lying along a line inclined about 50° from the vertical, and displaying different interference colours than the surrounding crystals. Careful observation of the cloudy band stratigraphy, drawn in Fig. 6.10.a, reveals that

the cloudy layer is in an initial folding stage, and the stripe of differently coloured crystals appears to lie in the axial plane of the fold. The fabric diagrams show that the ice surrounding the stripe displays the normal vertical single maximum fabric, whereas the crystals within the stripe are highly inclined from the vertical. The average inclination of the c-axes corresponds approximately with the inclination of the stripe, indicating that these crystals are undergoing rigid-body rotation as the ice becomes folded. The average direction of the c-axes is, however, not in the vertical plane of the thin section.

3. Distorted features at 2873 m - Fig. 6.11: Here, a clear, coarse grained layer is sandwiched between fine grained, cloudy layers. Folding appears evident and striping is observed in the fine grained ice below the clear layer. A fabric diagram from the striped part of the thin section shows two main populations of c-axes; one around the vertical, the other offset around 50° from the vertical and most likely representing crystals rotated by the folding process.

4. Large fold at 2923.8 m - Fig. 6.12: C-axes have been measured in the different parts of the fold, and in the ice surrounding it. Here, little effect on the normal vertical orientation is observed, indicating that the fabric has been reset by rotation of the c-axes towards the vertical.

A comprehensive study on the GISP2 core has revealed that stripes of the kind shown in Figs. 6.10 and 6.11 are common in the lowest 30% of this core (R.B. Alley, A.J. Gow & D.A. Meese, personal communication; Alley et al., in review). The inclination of the stripes varies from near-vertical to near-horizontal, and their intensity is variable. Alley and colleagues suggest, as a

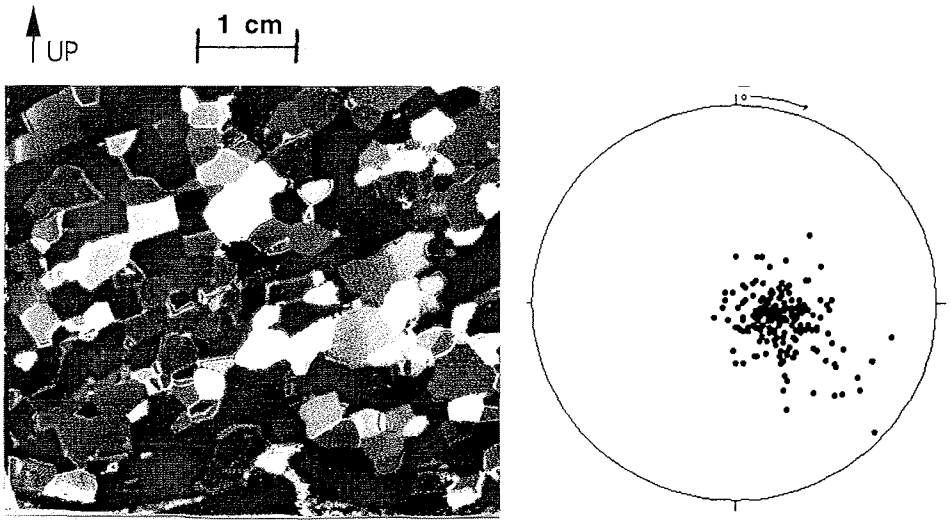

Fig. 6.9 - Thin section and fabric diagram from the inclined layer in Fig. 7.3.

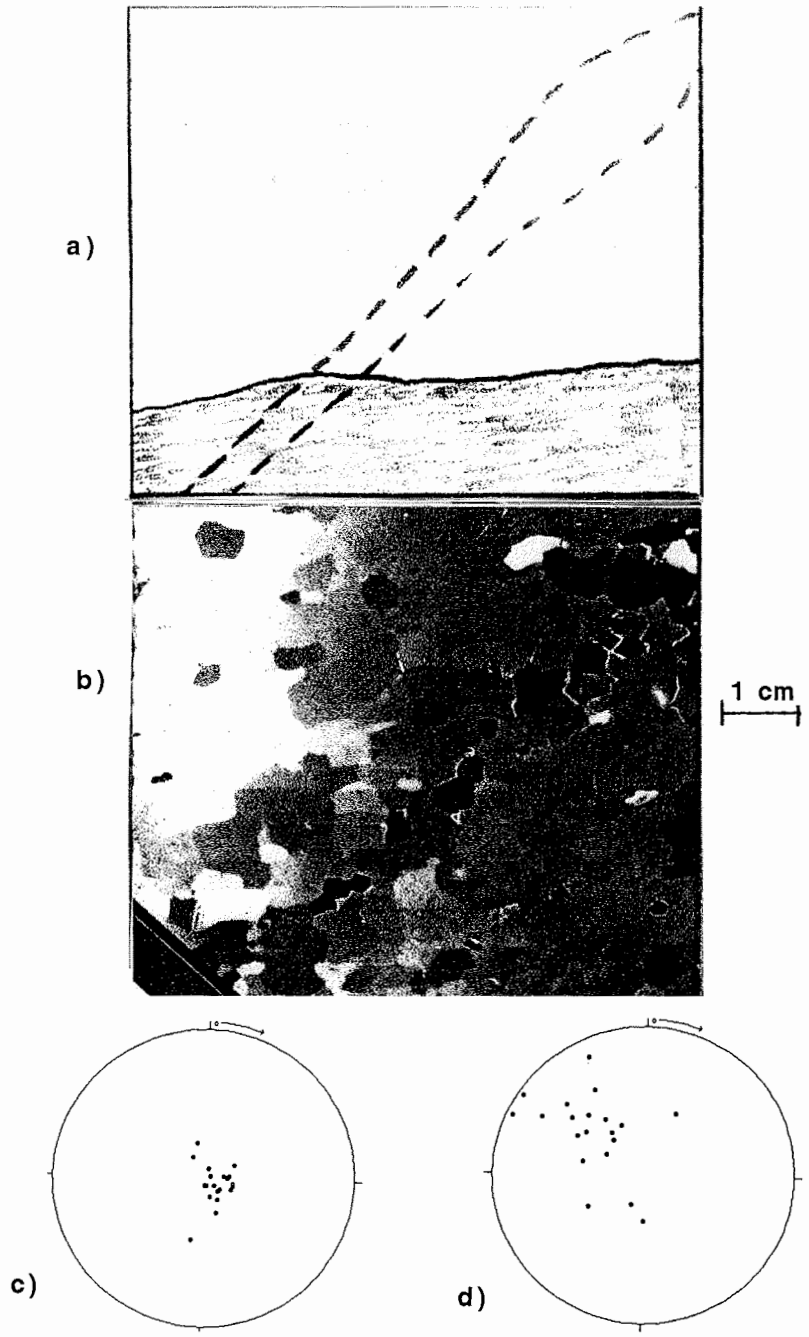

Fig. 6.10 - **a)** Drawing of the cloudy band layering at 2869.5 m depth. Slight folding of the cloudy layer is evident. The position of the stripe in b) is outlined with a broken line. **b)** Thin section from the core region shown in a), rotated to an extinction position which highlights the stripe of differently coloured crystals. **c)** C-axis orientations of 20 crystals in the ice surrounding the stripe. **d)** C-axis orientations of 20 crystals within the stripe.

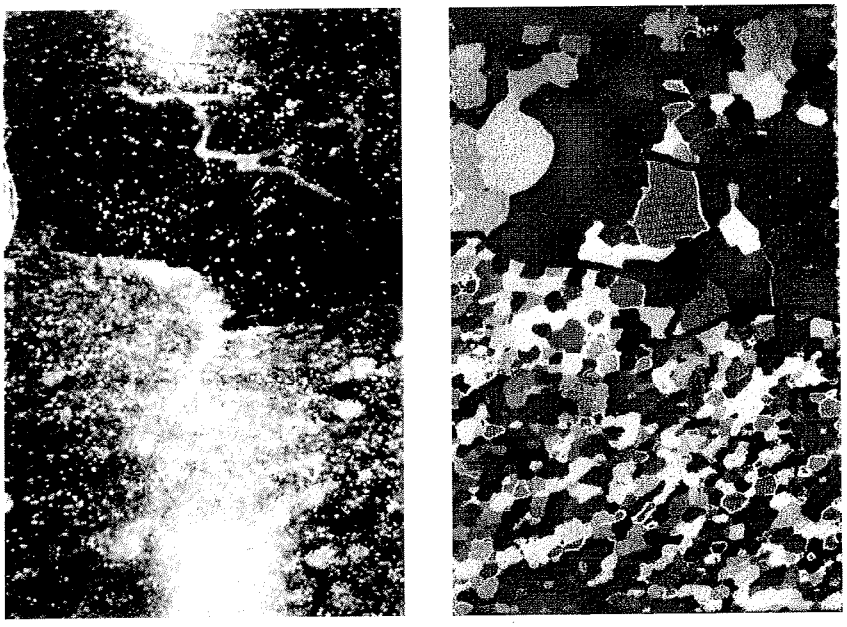

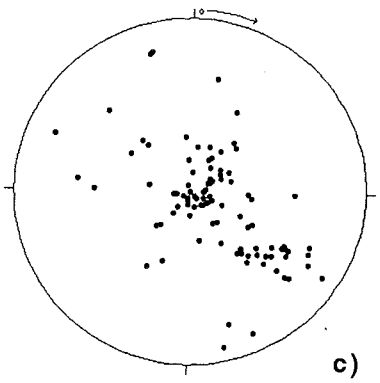

Fig. 6.11 - **a)** Distorted layer of clear ice, between cloudy layers. **b)** Thin section cut from the core part shown in a). Note difference in grain size between clear (outlined) and cloudy parts. Striping can be detected in the lower part of the section. **c)** Fabric diagram from the lower, striped part of the section.

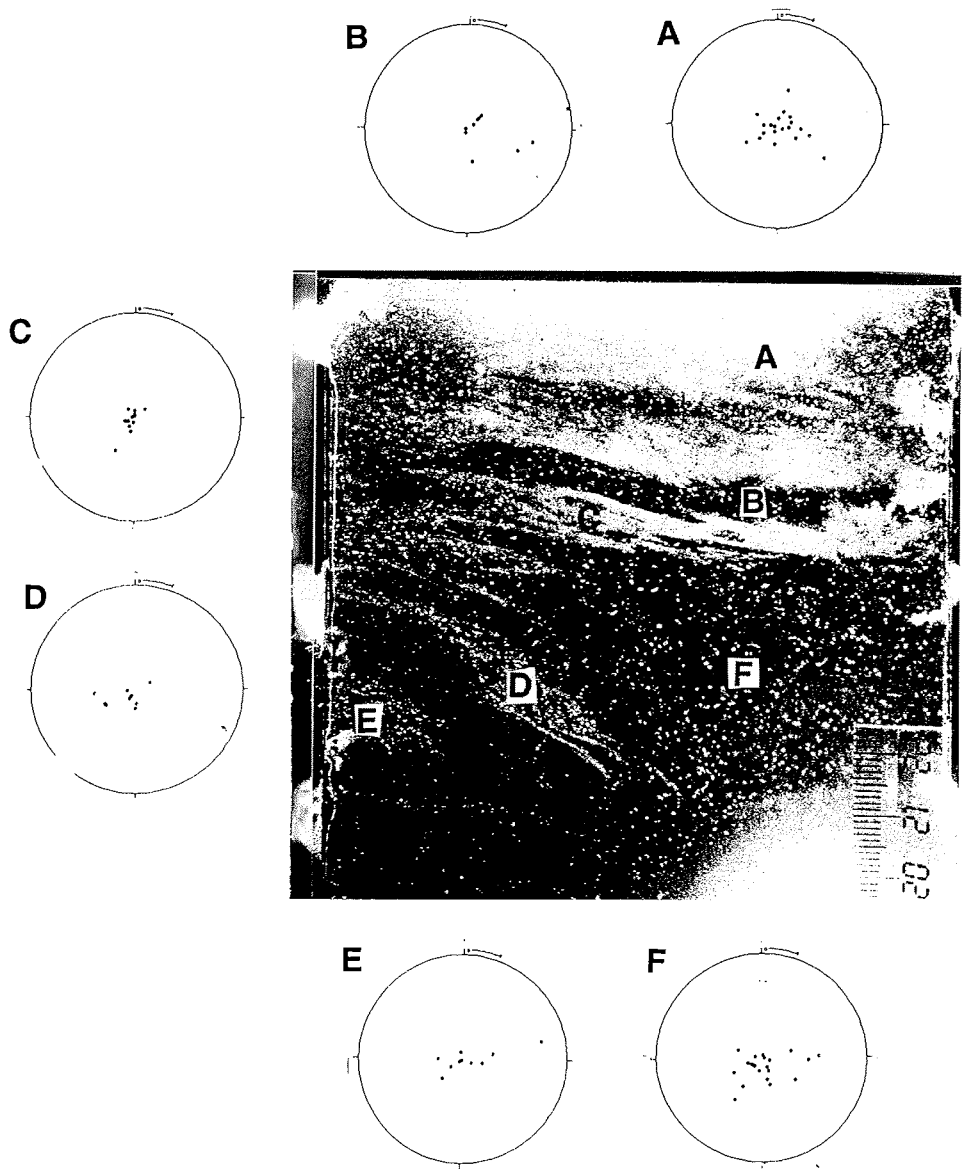

Fig. 6.12 - The largest overturned fold observed in the core. C-axis orientations determined on different parts of the corresponding thin section are shown.
A - Cloudy layer above fold. **B** - Thin, clear layer above fold. **C** - Horizontal part of cloudy fold layer. **D** - Inclined part of cloudy fold layer. **E** - Lowest part of cloudy fold layer. **F** - Clear ice outside fold.

possible explanation of their origin, organized polygonization of adjacent grains and subsequent rotation of some polygonized grains away from the vertical through simple shear. Another possibility would be the nucleation of new grains, a process which has been discussed in earlier sections.

Although the stripes have only been observed at a few selected depths in the GRIP core, particularly in the disturbed section, it seems likely that they commonly occur in the lowest few hundred meters of the core, as they do at the GISP2 site. Since they tend to occur in ice which displays a strong single maximum fabric, their effect will be to soften the ice against vertical compression, especially those stripes in which the basal planes are inclined near 45° from the vertical. This local softening is likely to further the formation of folds and other flow disturbances. Another important factor leading to the generation of these phenomena is the rheological contrast between cloudy and clear layers, demonstrated by fabric measurements and by results from deformation tests (Dahl-Jensen et al., 1996). This contrast could provide the initial "weakness" leading to the formation of the distortions and the associated fabric stripes.

The effect of the stripes on fabrics is interesting. As demonstrated in Figs. 6.10 and 6.11, the stripes contain grains whose c-axes tend to group into certain orientation populations, different from that of the surrounding ice. A double maximum fabric is f.ex evident in Fig. 6.11. Since stripes of different orientations have occasionally been observed to criss-cross each other in the cores (observed during Joint GRIP-GISP2 study), it seems likely that a thin section cut across, say two such criss-crossing stripes would display a three maxima fabric: One normal, vertical c-axis population and two offset from the vertical, one for each stripe. The striping could be thus possibly be at the origin of multiple maximum fabrics (typically 3-4 different maxima), which have been observed in Antarctic basal ice (Budd & Jacka, 1989). Further studies on ice from basal regions are necessary to clarify whether the fabric stripes observed in both Central Greenland cores are a general phenomenon in the large ice sheets, and to which extent they affect the fabrics and rheological properties of deep ice.

7. SUMMARY AND OUTLOOK

Conclusions

Crystal size variation in the GRIP core allows the identification of three major recrystallization regimes in the Central Greenland ice sheet. In the *normal grain growth* regime (0-700 m), crystal size increases steadily with the age of the ice, due to surface tension effects. In the *polygonization* regime (700-2800 m), subdivision of grains due to increasing strain prevents a further increase in crystal size. In the third regime (2800-3020 m), coarse grained ice is found in old, relatively warm ice. The formation process of its large crystals is not well understood, but may be due to the nucleation and rapid growth of new crystals; *migration recrystallization.*

In ice from the Wisconsin and Eemian periods, crystal size is anticorrelated with several impurities, including calcium, other major ions, and dust. This lends support to the hypothesis that high concentrations of impurities slow grain growth in polar ice. The effect is observed when calcium concentrations exceed 12 ppb, chloride concentrations exceed 20 ppb and the dust content rises above 0.5 mg/l.

The strong co-variation of crystal size with climatic parameters, especially in the Eemian ice, indicates that past climatic variation can be inferred from the study of crystal size changes in polar ice. This co-variation is likely to result from a complex interplay among several factors: *i)* Differences in the initial normal grain growth rate due to varying surface temperatures will result in ice from warm periods reaching a larger limiting grain size above the polygonization regime. *ii)* Impurity drag-effects in ice from cold periods will contribute to keeping this ice fine-grained. *iii)* Recrystallization at relatively high temperatures in the lowest 10% of the ice thickness, leading to the growth of large grains in ice with a low impurity content dating from warm periods, but hardly affecting fine grained ice from cold periods, will enhance the grain size differences between these two types of ice.

The crystal fabric measurements have demonstrated that the ice sheet becomes strongly anisotropic with depth. An initially random fabric near the surface is transformed to a strongly preferred fabric below 2 km depth, a development which is fully compatible with the stress system expected to dominate at the Central Greenland ice divide. The formation mechanism of the single maximum fabric is believed to be through c-axis rotation towards the axis of vertical compression by dislocation glide on the basal planes of the crystals. Simple shear is not believed to be of importance in forming the single

maximum. The single maximum fabric persists to a depth of 2800 m; below this depth, sparse c-axis data show a stretching of the fabric which could result from tensional stresses acting near the bottom. A recrystallization girdle, centered on the axis of compression, has not been found in the GRIP core.

Deep in the ice sheet, fine grained ice displays a stronger fabric than coarse grained ice. Since the fine grained ice has higher impurity content, this might indicate that the process of c-axis rotation is speeded by the presence of impurities in the ice.

Changes in fabric and crystal size lead to variation in the rheological properties of ice. The results do not indicate a major difference in flow properties across the Holocene-Wisconsin transition in the GRIP core, in contrast to the situation at Dye 3 and Camp Century. The formation of the strong single maximum leads to hardening of the ice against vertical compression. The presence of coarse grained ice in the Eemian ice and below the Saalean ice indicates that this ice has not been subject to rapid deformation.

The presence of considerable flow distortion of the original stratigraphy below 2850 m depth indicates that simple shear is, or has recently been, active at Summit, perhaps due to ice divide migration. The large-scale nature of the disturbances cannot be determined. The small-scale disturbances observed in the core are in the form of inclined layering, folding and other distortion and seem to be most prominent at the boundaries between clear and cloudy ice. This indicates differences in flow properties between these two types of ice. The disturbances are clearly observed to affect the ice fabric.

Due to the stratigraphic disturbances, the original timescale can not be considered certain below the level where the GRIP and GISP2 climatic records start to differ. This level is at 2750 m depth in the GRIP core, where the age of the ice is 100 000 years.

Recommendations

Future research on grain-size variations in ice cores should aim at a better understanding of factors controlling grain-growth rates. For example, grain size variations should be studied across ice-core increments where only a single impurity is present in elevated concentrations (e.g. volcanic sulphate or chloride peaks). In addition, since seasonal variations in $\delta^{18}O$ and various impurities are usually not in phase, comparison of these variations with grain size changes, in firn and ice cores drilled at optimum locations, would be likely to clarify which factors control grain growth in polar ice sheets.

Continuous measurements of crystal size along deep ice cores to be drilled in the future should be made, to confirm that crystal size varies with climatic parameters. Since thin section preparation is time consuming, attempts should be made to count crystal boundaries on flat core surfaces, like the one shown in Fig. 3.1.

Further work is needed to confirm that polygonization causes the stop in grain size increase at 400-700 m depth in ice cores. This could be achieved by detailed studies of misorientation angles between adjacent grains. In addition, detailed comparison of grain size distributions in the normal grain growth and polygonization regimes could yield valuable information.

A better understanding of the process leading to the formation of coarse grained ice in the lowest 250 m of the ice sheet is needed. In particular, it is important to find out whether this ice has gone through extensive recrystallization, so that no information on its previous grain-growth and fabric formation history is preserved. Thorough studies of fabrics in coarse grained ice and their relation to stress-strain conditions are needed. Detailed grain shape studies should also be carried out on such ice.

More quantitative work is needed to understand the effects of fabric evolution on ice sheet dynamics. The development of preferred fabrics should be included in future modelling of the flow and evolution of ice sheets.

Ongoing deformation tests on GRIP core samples should serve to clarify further the rheological differences between ice from different climatic periods. Greatly improved understanding can be expected to emerge from shear tests, to be carried out at the University of Copenhagen in the near future.

The flow disturbances in the lowest parts of the Central Greenland ice cores were encountered higher up in the sheet than anticipated by most researchers. This might indicate that the ice divide region is not as suitable for ice core drilling as previously assumed. Careful surveying of bedrock topography and internal layering, combined with improved modelling of ice flow near an ice divide, is essential for the selection of future drill sites. The Nord–GRIP deep core, to be drilled in North Greenland in the years 1996–1998, will hopefully resolve the current controversy surrounding the GRIP Eemian. Less accumulation at the proposed site (16 cm/yr) than at Summit (23 cm/yr), will probably ensure that ice from the Eemian will be higher up in the ice sheet at the Nord–GRIP location than at Summit, and thus less likely to have been affected by flow disturbances. The necessity of carrying out careful stratigraphic studies on this core, and other ice cores to be drilled in the future cannot be overemphasized. The occurrence of fabric stripes, their relation to flow disturbances and their effect on ice sheet rheology is likely to become an important subject of future studies.

REFERENCES

Adam, J.F. (1989). Methoden und Algorithmen zur Verwaltung und Analyse axialer 3-D-Richtungsdaten und ihrer Belegungsdichten. *Göttinger Arb. Geol. Paläontol.* **40**. Göttingen. 100 pp.

Alley, R.B. (1987). Transformations in polar firn. PhD Thesis, Univ. of Wisconsin, Madison.

Alley, R.B. (1988). Fabrics in polar ice sheets: Development and prediction. *Science,* **240**, 493-495.

Alley, R.B. (1992). Flow law hypotheses for ice sheet modelling. *J. Glaciol.*, **38** (129), 245-256.

Alley, R.B., J.H. Perepezko, & C.R. Bentley (1986a). Grain growth in polar ice I.: Theory. *J. Glaciol.,* **32** (112), 415-424.

Alley, R.B., J.H. Perepezko, & C.R. Bentley (1986b). Grain growth in polar ice II.: Application. *J. Glaciol.,* **32** (112), 425-433.

Alley, R.B., A.J. Gow & D.A. Meese (1995a). Mapping c-axis fabrics to study physical processes in ice. *J. Glaciol.*, **41** (137), 197-203.

Alley, R.B., A.J. Gow, S.J. Johnsen, J. Kipfstuhl, D.A. Meese & Th. Thorsteinsson (1995b). Comparison of deep ice cores. *Nature*, **373**, 393-394.

Alley, R.B., A.J. Gow, D.A. Meese, J.J. Fitzpatrick, E.D. Waddington & J.F. Bolzan (in review). Grain-scale processes, folding, and stratigraphic disturbance in the GISP2 ice core. Submitted to: JGR Special Issue. Proceedings of the Wolfeboro Meeting, September 1995.

Alley, R.B. & G.A. Woods (in press): Impurity influence on normal grain-growth in the GISP2 ice core. *J. Glaciol.* (in press).

Alley, R.B. & 11 others (in press). Visual-stratigraphic dating of the GISP2 ice core: basis, reproducibility, and persistence. Submitted to: JGR Special Issue. Proceedings of the Wolfeboro Meeting, September 1995.

Anandakrishnan, S., J.J. Fitzpatrick, R.B. Alley, A.J. Gow & D.A. Meese (1994). Shear-wave detection of asymmetric c-axis fabrics in the GISP2 ice core, Greenland. *J. Glaciol,* **40** (136), 491-496.

Anandakrishnan, S., R.B. Alley & E.D. Waddington (1994). Sensitivity of the ice-divide position in Greenland to climate change. *Geophys. Res. Lett.*, **21** (6), 441-444.

de Angelis, J.P. Steffensen & M. Legrand (1995). Primary aerosol (sea salt and soil dust) during the last climatic cycle: North-South comparison. *Abstract* - GISP2/GRIP Wolfeboro Workshop, September 1995.

Atkinson, H.V. (1988). Theories of normal grain growth in pure single phase systems. *Acta Metallurgica,* **36** (3), 469-491.

Azuma, N. & A Higashi (1985). Formation processes of ice fabric pattern in ice sheets. *Ann. Glaciol.,* **6**, 130-134.

Bender, M., T. Sowers, M.L. Dickson, J. Orchardo, P. Grootes, P. A. Mayewski & D.A. Meese. Climate correlations between Greenland and Antarctica during the past 100,000 years. *Nature*, **372**, 663-666.

Bernal, J.D. & Fowler, R.H. (1933). A theory of water and ionic solution, with particular reference to hydrogen and hydroxyl ions. *J. Chem. Phys.*, **1**, 515-548.

Bjerrum, N. (1951). Structure and properties of ice I. The position of the hydrogen atoms and the zero-point entropy of ice. *K. danske Vidensk. Selsk. Skr.*, **27**, 1-56.

Bouchez, J.L. & P. Duval (1982). The fabric of polycrystalline ice deformed in simple shear: Experiments in torsion, natural deformation and geometrical interpretation. *Textures and Microstructures*, **5**, 171-190.

Bragg, W.H. (1922). The crystal structure of ice. *Proc. Phys. Soc.*, **34**, 98-103.

Budd, W.F. & T.H. Jacka (1989). A review of ice rheology for ice sheet modelling. *Cold Reg. Sci. Technol.*, **16**, 107-144.

Castelnau, O. & P. Duval (1995). Simulations of anisotropy and fabric development in polar ices. *Ann. Glaciol.*, **20**, 277-282.

Castelnau, O., P. Duval, R.A. Lebensohn & G.R. Canova (1995). Viscoplastic modelling of texture development in polycrystalline ice with a self-consistent approach; comparison with bound estimates. *J. Geophys. Res.* (in press).

Castelnau, O., Th. Thorsteinsson, J. Kipfstuhl & P. Duval (in press). Modelling fabric development along the GRIP ice core, Central Greenland. *Ann. Glaciol.* (in press).

Chappellaz, J., T. Blunier, D. Raynaud, J.M. Barnola, J. Schwander & B. Stauffer (1993). Synchronous changes in atmospheric CH_4 and Greenland climate between 40 and 8 kyr. *Nature*, **366**, 443-445.

Clausen H.B. & C.C. Langway, Jr. (1989). The ionic deposits in polar ice cores. In: *The Environmental Record in Glaciers and Ice Sheets*, H. Oeschger & C.C. Langway, Jr., eds., Dahlem Workshop Report, 225-248.

Cox, K.G., N.B. Price & B. Harte (1974). *The Practical Study of Crystals, Minerals and Rocks.* McGraw-Hill. 245 pp.

Cuffey, K.M., G.D. Clow, R.B. Alley, M. Stuiver, E.D. Waddington & R.W. Saltus. Large Arctic Temperature Change at the Wisconsin-Holocene Glacial Transition. *Science*, **270**, 455-458.

Cunningham, J. & E.D. Waddington (1990). Boudinage: A source of stratigraphic disturbance in glacial ice in Central Greenland. *J. Glaciol.*, **36** (124), 269-272.

Dahl-Jensen, D. (1989). Two-dimensional thermo-mechanical modelling of flow and depth-age profiles near the ice divide in Central Greenland. *Ann. Glaciol.*, **12**, 31-36.

Dahl-Jensen, D. & Gundestrup, N. (1987). Constitutive properties of ice at Dye 3, Greenland. *The Physical basis of Ice Sheet Modelling, IAHS*, **170**, 31-43.

Dahl-Jensen, D., S.J. Johnsen, C.U. Hammer, H.B. Clausen & J. Jouzel (1993). Past accumulation rates derived from observed annual layers in the GRIP ice core from Summit, Central Greenland. *Ice in the climate system,* NATO ASI Series, **I12**; W.R. Peltier, ed. Springer-Verlag Berlin Heidelberg, 517-532.

Dahl-Jensen, D., Th. Thorsteinsson, R.B. Alley & H. Shoji (1996). Mechanical tests on GRIP samples. JGR Special Issue. Proceedings of the Wolfeboro Meeting, September 1995 (in review).

Dansgaard, W. & S.J. Johnsen (1969). A flow model and a time scale for the ice core from Camp Century, Greenland. *J. Glaciol.,* **8** (53), 215-223.

Dansgaard, W., S.J. Johnsen, H.B. Clausen & N. Gundestrup (1973). Stable isotope glaciology. *Meddelelser om Grønland,* **197** (2), 53 pp.

Dansgaard, W., H.B. Clausen, N. Gundestrup, C.U. Hammer, S.J. Johnsen, P. M. Kristinsdottir & N. Reeh (1982). A new Greenland deep ice core. *Science,* **218**, 1273-1277.

Dansgaard, W., S.J. Johnsen, H.B. Clausen, D. Dahl-Jensen, N.S. Gundestrup, C.U. Hammer, C.S. Hvidberg, J.P. Steffensen, A.E. Sveinbjörnsdottir, J. Jouzel & G. Bond (1993). Evidence for general instability of past climate from a 250 kyr ice-core record. *Nature,* **364**, 218-220.

Duval, P. (1981). Creep and fabrics of polycrystalline ice under shear and compression. *J. Glaciol.,* **27** (95), 129-139.

Duval, P. & C. Lorius (1980). Crystal size and climatic record down to the last ice age from Antarctic ice. *Earth Planet. Sci. Lett.,* **48**, 59-64.

Duval, P., M.F. Ashby & I. Anderman (1983). Rate-controlling processes in the creep of polycrystalline ice. *J. Phys. Chem.,* **87** (21), 4066-4074.

Duval, P. & O. Castelnau (1995). Dynamic recrystallization of ice in polar ice sheets. *J. Physique,* in press.

Eicken, H. (1985). Der Universal-Drehetisch - Hinweise für den arglosen Benutzer. *Special Report.*, Alfred Wegener Institute.

Ehlers, E.G. (1987). *Optical Mineralogy. I. Theory and Techniques.* Blackwell Publications. 158 pp.

Feltham, P. (1957). *Acta Metallurgica,* **5**, 97.

Fisher, R. (1953). Dispersion on a sphere. *Proc. Roy. Soc. London,* **217**, 295-305.

Fisher, D.A. & R.M. Koerner (1986). On the special rheological properties of ancient microparticle laden Northern Hemisphere ice as determined by bore-hole and core measurements. *J. Glaciol.,* **32** (112), 501-510.

Fuchs, A. & M. Leuenberger (in press). $\delta^{18}O$ of atmospheric oxygen measured on GRIP ice core revealing unexpected stratigraphic features well above bedrock. Submitted to *Geophys. Res. Lett.*

Fuhrer, K. (1995). Ammonium-, Calzium-, Wasserstoffperoxid- und Formaldehyd-messungen an einem grönländischen Tiefbohrkern: Diskussion der letzten 200.000 Jahre. *PhD Dissertation,* Physikalisches Institut, Universität Bern.

Fuhrer, K., A. Neftel, M. Anklin & V. Maggi (1993). Continuous measurements of hydrogen peroxide, formaldehyde, calcium and ammonium concentrations along the new GRIP ice core from Summit, Central Greenland. *Atmospheric Environment,* **27A** (12), 1873-1880.

Fujita, S., M. Nakawo & S. Mae (1987). Orientation of the 700 m Mizuho core and its strain history. *Proc. NIPR Symp. Polar Meteorol. Glaciol.*, 1, 122-131.

Ghosh, S.K. (1993). *Structural geology. Fundamentals and modern developments.* Pergamon, Oxford, England. 598 pp.

Glen, J.W. (1955). The creep of polycrystalline ice. *Proc. R. Soc. A.*, **228**, 519-538.

Gottstein G. & H. Mecking (1985). Recrystallization. In: *Preferred Orientation in Deformed Metals and Rocks: An Introduction to Modern Texture Analysis.* H.-R. Wenk, ed. Academic Press, pp. 183-218.

Gow, A.J. (1969). On the rates of growth of grains and crystals in south polar firn. *J. Glaciol.*, **8** (53), 241-252.

Gow, A.J. (1972). Glaciological investigations in Antarctica. *Antarctic J. U.S.*, **7** (4), 100-101.

Gow, A.J. (1994). Post-drilling recrystallization of the Byrd Station deep ice core and its relevance to current and future deep-core drilling on polar ice sheets. *Ann. Glaciol.*, **20**, 231-236.

Gow, A.J. & T. Williamson (1976). Rheological implications of the internal structure and crystal fabrics of the West Antarctic ice sheet as revealed by deep core drilling at Byrd Station. *Geol. Soc. Am. Bull.*, **87**, 1665-1677.

Gow, A. J., S. Epstein. & W. Sheehy (1979). On the origin of stratified debris in ice cores from the bottom of the Antarctic ice sheet. *J. Glaciol.*, **23** (89), 185-192.

Grootes, P., M. Stuiver, J.W.C. White, S. Johnsen & J. Jouzel (1993). Comparison of oxygen isotope records from the GISP2 and GRIP Greenland ice cores. *Nature,* **366**, 552-554.

GRIP Members (1993). Climatic instability during the last interglacial period as revealed in the Greenland Summit ice-core. *Nature* , **364**, 203-207.

Guillopé, M. & J.P. Poirier (1979). Dynamic recrystallization during creep of single-crystalline halite: An experimental study. *J. Geophys. Res.*, **84** (B10), 5557-5567.

Gundestrup, N.S., D. Dahl-Jensen, B.L. Hansen & J. Kelty (1993). Bore-hole survey at Camp Century, 1989. *Cold Reg. Sci. Technol.*, **21**, 187-193.

Gundestrup, N.S., J.P. Steffensen & J. Schwander (1994). The GRIP deep drilling camp. *Ice Drilling Technology.* Mem. Natl. Inst. Polar Res., Special Issue, **49**, 358-370.

Hansen, B.L. & N.S. Gundestrup (1988). Resurvey of bore hole at Dye 3, South Greenland. *J. Glaciol.*, **34** (117), 1-5.

Hambrey, M. & A.G. Milnes (1975). Boudinage in glacier ice - some examples. *J. Glaciol.*, **14**, 383-393.

Hammer, C.U., H.B. Clausen, W. Dansgaard, N. Gundestrup, S.J. Johnsen & N. Reeh (1978). Dating of Greenland ice cores by flow models, isotopes, volcanic debris and continental dust. *J. Glaciol.*, **20**, 3-26.

Hammer, C. U. (1980). Acidity of polar ice cores in relation to absolute dating, past volcanism and radio echos. *J. Glaciol.*, **25** (93), 359-372.

Hammer, C.U., H.B. Clausen & W. Dansgaard (1980). Greenland ice sheet evidence of post-glacial volcanism and its climatic impact. *Nature*, **288**, 230-235.

Hammer, C.U., H.B. Clausen, W. Dansgaard, A. Neftel, P. Kristinsdóttir & E. Johnson (1985). Continuous impurity analysis along the Dye 3 deep core. In: *Greenland Ice Core: Geophysics, Geochemistry and the Environment*, C.C. Langway, Jr., H. Oeschger & W. Dansgaard, eds., AGU Monograph, **33**, 90-94.

Hammer, C.U., H.B. Clausen & H. Tauber (1986). Ice core dating of the Pleistocene-Holocene boundary applied to a calibration of the ^{14}C time scale. *Radiocarbon*, **28** (2A), 284-291.

Hempel, L. & F. Thyssen (1992). Deep radio echo soundings in the vicinity of GRIP and GISP2 drill sites, Greenland. *Polarforschung,* **62** (1), 11-16.

Hempel, L. (1994). Der Zentralteil des grönländischen Inlandeises: Ergebnisse aus hochauflösenden elektromagnetischen Reflexionsmessungen. *PhD Thesis*, Universität Münster.

Herron, S.L. & C.C. Langway, Jr. (1979). The debris-laden ice at the bottom of the Greenland ice sheet. *J. Glaciol.,* **23** (89), 193-207.

Herron, S.L. & C.C. Langway, Jr. (1982). A comparison of ice fabrics and textures at Camp Century, Greenland and Byrd Station, Antarctica. *Ann. Glaciol.,* **3**, 118-124.

Herron, M.M. & C.C. Langway, Jr. (1985). Chloride, nitrate and sulfate in the Dye 3 and Camp Century, Greenland ice cores. *In: Greenland Ice Core: Geophysics, Geochemistry and the Environment*, C.C. Langway, Jr., H. Oeschger & W. Dansgaard, eds., AGU Monograph, **33**, 77-84.

Herron, S. L., C.C. Langway, Jr. & K. Brugger (1985). Ultrasonic velocities and crystalline anisotropy in the ice core from Dye 3, Greenland. In: *Greenland Ice Core: Geophysics, Geochemistry and the Environment*, C.C. Langway, Jr., H. Oeschger & W. Dansgaard, eds., AGU Monograph, **33**, 49-56.

Hillert, M. (1965). On the theory of normal and abnormal grain growth. *Acta Metallurgica,* **13** (3), 227-238.

Hobbs, B.E., W.D. Means & P.F. Williams (1976). *An outline of structural geology.* John Wiley & Sons. 571 pp.

Hobbs, P.V. (1974). *Ice physics.* Clarendon Press, Oxford, England. 837 pp.

Hodge, S.M., D.L. Wright, J.A. Bradley, R.W. Jacobel, N. Skou & B. Vaughn (1990). Determination of the surface and bed topography in Central Greenland. *J. Glaciol.,* **36** (122), 17-30.

Hondoh, T., K. Azuma & A. Higashi (1987). Self-interstitials in ice. *Journal de Physique,* C1, **48** (3), 183-187.

Hooke, R.LeB. (1973). Structure and flow in the margin of the Barnes Ice Cap, Baffin Island, N.W.T., Canada. *J. Glaciol.,* **12** (66), 423-438.

Hooke, R. LeB. & P.J. Hudleston (1980). Ice fabrics in a vertical flow plane, Barnes ice cap, Canada. *J. Glaciol.,* **25** (92), 195-214.

Hooke, R.LeB., M. Mellor, W.F. Budd, J.W. Glen, A. Higashi, T.H. Jacka, R.C. Lile, R.T. Martin, M.F. Meier, D.S. Russell-Head & J. Weertman (1980).

Mechanical properties of polycrystalline ice: An assessment of current knowledge and priorities for research. *Cold Reg. Sci. Technol.*, **3**, 263-275.

Hudleston, P.J. (1976). Recumbent folding in the base of the Barnes ice cap, Baffin Island, Northwest Territories, Canada. *Geol. Soc. Am. Bull.*, **87**, 1684-1692.

Hull, D., & D.J. Bacon (1984). *Introduction to dislocations*, 3rd ed. Pergamon, Oxford, England. 257 pp.

Hutchinson, J.W. (1976). Bounds and self-consistent estimates for creep of polycrystalline materials. *Proc. R. Soc. Lond.*, **A348**, 101-127.

Jaccard, C. (1964). Thermodynamics of irreversible processes applied to ice. *Phys. condens. Matter*, **3**, 99-118.

Jacka, T.H. (1984a). Laboratory studies on relationships between crystal size and flow rate. *Cold. Reg. Sci. Technol.*, **10**, 31-42.

Jacka, T.H. (1984b). The time and strain required for development of minimum strain rates in ice. *Cold. Reg. Sci. Technol.*, **8**, 261-268.

Jacka, T.H. & M. Maccagnan (1984). Ice crystallographic and strain rate changes with strain in compression and extension. *Cold. Reg. Sci. Technol.*, **8**, 269-286.

Jacka, T.H. & Li Jun (1995). The steady state crystal size of deforming ice. *Ann. Glaciol.*, **20**, 13-18.

Jaeger, J.C. (1962). *Elasticity, Fracture and Flow*, 2nd Ed., Methuen, London.

Johnsen, S.J., W. Dansgaard, H.B. Clausen & C.C. Langway (1972). Oxygen isotope profiles through the Antarctic and Greenland ice sheets. *Nature*, **235**, 429-434.

Johnsen, S.J., H.B. Clausen, W. Dansgaard, K. Fuhrer, N. Gundestrup, C.U. Hammer, P. Iversen, J. Jouzel, B. Stauffer & J.P. Steffensen (1992). Irregular glacial interstadials recorded in a new Greenland ice core. *Nature*, **359**, 311-313.

Johnsen, S.J., N.S. Gundestrup, S.B. Hansen, J. Schwander & H. Rufli (1994). The new improved version of the Istuk ice core drill. *Ice Drilling Technology*. Mem. Natl. Inst. Polar Res., Special Issue, **49**, 9-23.

Johnsen, S.J., D. Dahl-Jensen, W. Dansgaard, & N. Gundestrup (1995). Greenland palaeotemperatures derived from GRIP bore hole temperature and ice core isotope profiles. *Tellus* , **47B** (5), 624-630.

Johnsen, S.J., H.B. Clausen, W. Dansgaard, N.S. Gundestrup, C. U. Hammer & H. Tauber (1995b). The Eem stable isotope record along the GRIP ice core and its interpretation. *Quaternary Research*, **43**, 117-124.

Kamb, B. (1961). The glide direction in ice. *J. Glaciol.*, **3** (30), 1097-1106.

Kamb, B. (1962). Refraction corrections for Universal Stage measurements. I. Uniaxial crystals. *The American Mineralogist* , **47** (3), 227-245.

Kamb, B. (1972). Experimental recrystallization of ice under stress. *Geophys. Monogr. Am. Geophys. Union*, **18**, 211-241.

Keller, K., N. Gundestrup, D. Dahl-Jensen, C.C. Tscherning, R. Forsberg & S. Ekholm (1995). The ice deformation and mass balance at the Summit of

Greenland as determined by GPS and gravity measurements. *Geological Survey of Greenland Open File Series,* **95/5.**

Kingery, W.D., H.K. Bowen, D.R. Uhlmann (1976). *Introduction to ceramics.* John Wiley & Sons, New York. 1032 pp.

Kipfstuhl, J. & Th. Thorsteinsson (1993). Cloudy bands and visual stratigraphy of the GRIP ice core. *Abstract*, EOS Transactions, **74** (43).

Koerner, R.M. & D.A. Fisher (1979). Discontinuous flow, ice texture and dirt content in the basal layers of the Devon Island Ice Cap. *J. Glaciol.*, **23** (89), 209-222.

Kohnen, H. & A.J. Gow (1979). Ultrasonic velocity investigations of crystal anisotropy in deep ice cores from Antarctica. *J. Geophys. Res..* **84** (C8), 4865-4874.

Lange, M. (1988). A computer-controlled system for ice-fabric analysis on a Rigsby stage. *Ann. Glaciol.,* **10**, 92-94.

Langway, C.C., Jr. (1958). Ice Fabrics and the Universal Stage. *SIPRE Technical Report*, **62**.

Langway, C.C., Jr. (1967). Stratigraphic analysis of a deep ice core from Greenland. *CRREL Research Report* , **77**, 130 pp.

Langway, C.C., Jr., H. Oeschger & W. Dansgaard (1985). The Greenland ice sheet program in perspective. In: *Greenland Ice Core: Geophysics, Geochemistry and the Environment*, C.C. Langway, Jr., H. Oeschger & W. Dansgaard, eds., AGU Monograph, **33**, 90-94.

Langway, C.C., Jr., H. Shoji & N. Azuma (1988). Crystal size and orientation patterns in the Wisconsin-age ice from Dye 3, Greenland. *Ann. Glaciol.,* **10**, 109-115.

Legrand, M., C. Hammer, M. de Angelis, R. Delmas & H.B. Clausen (1995). Sulphur derived species over the last climatic cycle in Greenland. *Abstract* - GISP2/GRIP Wolfeboro Workshop, September 1995.

Li Jun. (1995). Interrelation between flow properties and crystal structure of snow and ice. *PhD Thesis,* University of Melbourne.

Lile, R.C. (1978). The effect of anisotropy on the creep of polycrystalline ice. *J. Glaciol.*, **21** (85), 475-483.

Lipenkov, V.Y., N.I. Barkov, P. Duval & P.Pimienta (1989). Crystalline texture of the 2083 m ice core at Vostok Station, Antarctica. *J. Glaciol.* , **35** (121), 392-398.

Lliboutry, L.A. (1964). *Traité de Glaciologie.* **1.** Masson, Paris.

Lliboutry, L. & P. Duval (1985). Various isotropic and anisotropic ices found in glaciers and polar ice caps and their corresponding rheologies. *Annales Geophysicae,* **3** (2), 207-224.

Louat, N.P. (1974). On the theory of normal grain growth. *Acta Metallurgica,* **22** (6) 721-724.

Lücke, K. & H.P. Stüve (1971). On the theory of impurity controlled grain boundary motion. *Acta Metallurgica,* **19**, 1087-1099.

Mayewski, P.A., L.D. Meeker, S. Whitlow, M.S. Twickler, M.C. Morrison, P. Bloomfield, G.C. Bond, R.B. Alley, A.J. Gow, P.M. Grootes, D.A. Meese, M. Ram, K.C. Taylor & W. Wumkes (1994). Changes in atmospheric

circulation and ocean ice cover over the North Atlantic during the last 41,000 years. *Science,* **263**, 1747-1751.

Meese, D.A., A.J. Gow, P.M. Grootes, P.A. Mayewski, M. Ram, M. Stuiver, K.C. Taylor, E.D. Waddington & G.A. Zielinski (1994). The accumulation record from the GISP2 core as an indicator of climate change throughout the Holocene. *Science,* **266** (5191), 1680-1682.

Miller, S.L. (1969). Clathrate hydrates of air in Antarctic ice. *Science,* **165**, 489-490.

Milsch, H. (1994). Mechanisches Verhalten von Eis längs des Bohrkerns aus dem Greenland Ice Core Project (GRIP) in Relation zur präferentiellen Gitterorientierung der Eiskristalle. *Diplom-Thesis.* Georg-August-Universität, Göttingen.

Müller, G. & M. Raith (1987). Methoden der Dünnscliffmikroskopie. *Clausthaler Tektonische Hefte,* **14**. 152 pp.

Nye, J.F. (1963). Correction factor for accumulation measured by the thickness of the annual layers in an ice sheet. *J. Glaciol.,* **4**, 785-788.

Oeschger, H., B. Stauffer, A. Neftel, J. Schwander & R. Zumbrunn (1982). Atmospheric CO_2 content in the past. *Ann. Glaciol.*, **3**, 227-232.

Paterson, W.S.B. (1977). Secondary and tertiary creep of glacier ice as measured by borehole closure rates. *Rev. Geophys. Space Phys.,* **15** (1), 47-55.

Paterson, W.S.B. (1984). Why ice age ice is sometimes "soft". *Cold. Reg. Sci. Technol.,* **20**, 75-98.

Paterson, W.S.B. (1994). *The physics of glaciers.* Pergamon, Oxford, England. 480 pp.

Pauer, F., J. Kipfstuhl & W. F. Kuhs (1995). Raman spectroscopic study on the nitrogen/oxygen ratio in the GRIP ice core. *Geophys. Res. Lett.,* **22** (8), 969-971.

Pauling, L. (1935). The structure and entropy of ice and of other crystals with some randomness of atomic arrangement. *J. Am. Chem. Soc.,* **57**, 2680-2684.

Petit, J.R, P. Duval & C. Lorius (1987). Long-term climatic changes indicated by crystal growth in polar ice. *Nature,* **326**, 62-64.

Petrenko, V.F. (1993). Structure of ordinary ice I_h. Part I: Ideal structure of ice. *CRREL Special Report 93-25.*

Petrenko, V.F. (1994). Structure of ordinary ice I_h. Part II: Defects in ice. Vol. 1: Point defects. *CRREL Special Report 94-4.*

Pimienta, P., P. Duval & V. Ya. Lipenkov (1988). Mechanical behaviour of ice along the 2040 m Vostok core, Antarctica. *Ann. Glaciol.,* **10**, 137-140.

Poirier, J.P. (1985). *Creep of crystals.* Cambridge University Press. 260 pp.

Poirier, J.P. & Guillopé, P. (1979). Deformation induced recrystallization of minerals. *Bull. Mineral.,* **102**, 67-74.

Post, A. (1972). Periodic surge origin of folded medial moraines on Bering piedmont glacier, Alaska. *J. Glaciol.,* **11**, 219-226.

Raymond, C.F. (1983). Deformation in the vicinity of ice divides. *J. Glaciol.,* **29** (103), 357-373.

Raynaud, D., J. Jouzel, J.M. Barnola, J. Chappellaz, R.J. Delmas, C. Lorius (1993). The ice record of greenhouse gases. *Science*, **259**, 926-934.

Rigsby, G. (1951). Crystal fabric studies on Emmons glacier, Mount Rainier, Washington. *J. Geology*, **49**, 590-598.

Russell-Head, D.S. & W.F. Budd (1979). Ice-sheet flow properties derived from bore-hole shear measurements combined with ice-core studies. *J. Glaciol.*, **24** (90), 117-130.

Schmid, E. & W. Boas (1935). *Kristallplastizität.* Springer, Berlin.

Schøtt, C., E.D. Waddington & C.F. Raymond (1992). Predicted time-scales for GISP2 and GRIP boreholes at Summit, Greenland. *J. Glaciol.*, **38** (128), 162-168.

Shoji, H. & C.C. Langway, Jr. (1988). Flow-law parameters of the Dye 3, Greenland, deep ice core. *Ann. Glaciol.*,**10**, 146-150.

Smith, R.B. (1975). Unified theory of the onset of folding, boudinage, and mullion structure. *Geol. Soc. Am. Bull.*, **86**, 1601-1609.

Smith, R.B. (1977). Formation of folds, boudinage, and mullions in non-Newtonian materials. *Geol. Soc. Am. Bull.*, **88**, 312-320.

Souchez, R., J.-L. Tison, R. Lorrain, M. Lemmens, L. Janssens, M. Stievenard, J. Jouzel, A. Sveinbjörnsdóttir & S. J. Johnsen (1994). Stable isotopes in the basal silty ice preserved in the Greenland Ice Sheet at Summit; environmental implications. *Geophys. Res. Lett.*, **21** (8), 693-696.

Souchez, R., M. Lemmens & J. Chappellaz (1995). Flow induced mixing in the GRIP basal ice deduced from the CO_2 and CH_4 records. *Geophys. Res. Lett.*, **22**, (1), 41-44.

Srolovitz, D.J., M.P. Anderson, P.S. Sahni & G.S. Grest (1984). Computer simulation of grain growth - II. Grain size distribution, topology and local dynamics. *Acta Metallurgica*, **32** (5), 793-802.

Staffelbach, T., B. Stauffer & H. Oeschger (1988). A detailed analysis of the rapid changes in ice-core parameters during the last ice age. *Ann. Glaciol.*, **10**, 167-170.

Stander, E. & B. Michel (1989). The development of aligned columnar sea ice: A field investigation. *J. Glaciol.*, **35** (120), 217-223.

Steinemann, S. (1958). Experimentelle Untersuchungen zur Plastizität von Eis. *Beitr. Geol. Schweiz, Geotech. Ser.*, **10**, 1-72.

Stephenson, P.J. (1967). Some considerations of snow metamorphism in the Antarctic Ice Sheet in the light of ice crystal studies. In: Oura, H. (ed), *Physics of Snow and Ice*, **I**, Institute of Low Temperature Science, Hokkaido University, Sapporo, Japan, 725-740.

Taylor, G.I. (1938). Plastic strain in metals. *Journal of the Institute of Metals*, **LXII**, 307-324.

Taylor, K., C.U. Hammer, R.B. Alley, H.B. Clausen, D. Dahl-Jensen, A.J. Gow, N.S. Gundestrup, J. Kipfstuhl, J.C. Moore & E.D. Waddington (1993). Electrical conductivity measurements from the GISP2 and GRIP Greenland ice cores. *Nature*, **366**, 549-552.

Thompson, L.G. & E. Mosley-Thompson (1981). Microparticle concentration variations linked with climate change. *Science*, **212**, 812-815.

Thorsteinsson, Th. (1990). Silty ice from the bottom of the Greenland ice sheet: An investigation of debris content and ice-crystal size and orientation in the bottom layers of the Dye 3 ice core. *MS-Thesis* (in Danish), Geophysical Institute, University of Copenhagen. 55 pp.

Thorsteinsson, Th., J. Kipfstuhl, H. Eicken, S.J. Johnsen, & K. Fuhrer (1995). Crystal size variations in Eemian-age ice from the GRIP ice core, Central Greenland. *Earth Planet. Sci. Lett.*, **131**, 381-394.

Thorsteinsson, Th., J. Kipfstuhl & H. Miller (1996). Textures and fabrics in the GRIP ice core. JGR Special Issue. Proceedings of the Wolfeboro Meeting, September 1995 (in press).

Tison, J.L., Th. Thorsteinsson, R.D. Lorrain & J. Kipfstuhl (1994). Origin and development of textures and fabrics in basal ice at Summit, Central Greenland. *Earth Planet. Sci. Lett.*, **125**, 421-437.

Ueda, H.T. & D.E. Garfield (1968). Drilling through the Greenland ice sheet. *CRREL Special Report*, **126**, 7 pp.

Urai, J.L., W.D. Means & G.S. Lister (1986). Dynamic recrystallization of minerals. In: *Mineral and Rock Deformation: Laboratory Studies*, B.E. Hobbs and H.C. Heard, eds., *Geophys. Monogr. Am. Geophys. Union,* **36**, 161-200.

van der Veen, C.J. & I.M. Whillans (1994). Development of fabric in ice. *Cold Reg. Sci. Technol.*, **22**, 171-195.

von Mises, R. (1928). Mechanik der plastischen Formänderung von Kristallen. *Zeitschrift für Angewandten und Matematische Mecanik,* **8**, 161-184.

Wallbrecher, E. (1978). Ein Cluster-Verfahren zur richtungsstatistichen Analyse tektonischer Daten. *Geologische Rundschau,* **67**, 840-857.

Wallbrecher, E. (1979). Methoden zum quantitativen Vergleich von Regelungsgraden und -formen strukturgeologischer Datenmengen mit Hilfe von Vektorstatistik und Eigenwertanalyse. *N. Jb. Geol. Paläont. Abh.,* **159**, 113-149.

Wallbrecher, E. (1986). *Tektonische und gefügeanalytische Arbeitsweisen: Graphische, rechnerische und statistische Verfahren.* Enke, Stuttgart. 244 pp.

Weertman, J. (1983). Creep deformation of ice. *Ann. Rev. Earth. Planet. Sci.,* **11**, 215-240.

Whillans, I.M. & K.C. Jezek (1987). Folding in the Greenland ice sheet. *J. Geophys. Res.*, **92** (B1), 485-493.

Wolff, E.W., J.C. Moore, H.B. Clausen, C.U Hammer, J. Kipfstuhl and K. Fuhrer (1995). Long-term changes in the acid and salt concentrations of the Greenland Ice Core Project ice core from electrical stratigraphy. *J. Geophys. Res.,* **100** (D8), 16249-16263.

Woodcock, N.H. (1977). Specification of fabric shapes using an eigenvalue method. *Geol. Soc. Am. Bull.,* **88**, 1231-1236.

Woods, G.A. (1994). Grain growth behavior of the GISP2 ice core from Central Greenland. *Technical Report Series,* **94-002**, Earth System Science Center, Penn State University. 85 pp.